Electrochemical Properties of Rare Earth-Doped Ceria and Its Application to Solid Oxide Fuel Cell

March 2008

SHIMONOSONO Taro

CONTENT

CHAPTER 1 General Introduction
1.1 Solid Oxide Fuel Cell 1
1.2 Purpose 4
References 6

CHAPTER 2 Electronic Conductivity of Rare Earth-Doped Ceria Ceramics
2.1 Introduction 10
2.2 Experimental Procedure
2.2.1 Sample Preparation 10
2.2.2 Measurement of Electronic Conductivity by the Hebb-Wagner Method 11
2.3 Theoretical Approach to Electronic Conduction
2.3.1 Electronic Conductivity and Applied Voltage 13
2.3.2 Possible Interactions between Rare Earth-Doped Ceria and Electron 15
2.4 Results and Discussion
2.4.1 Electronic Conductivity 17
2.4.2 Comparison of Oxide Ion Conductivity and Electronic Conductivity 22
2.5 Summary 37
References 38

CHAPTER 3 Electrochemical Properties of Cathode of Solid Oxide Fuel Cell with Gd-Doped Ceria Electrolyte
3.1 Introduction 39
3.2 Experimental Procedure
3.2.1 Powder Preparation of SOFC Component 42
3.2.2 Measurement of Cell Performance 42
3.2.3 Chemical Reaction between GDC Powder and $SrRuO_3$ or Co_2RuO_4 Powder 43
3.3 Results and Discussion
3.3.1 Microstructures of ITO, $SrRuO_3$ or Co_2RuO_4 (cathode) / $Ce_{0.8}Gd_{0.2}O_{1.9}$ (electrolyte) / Ni-$Ce_{0.8}Gd_{0.2}O_{1.9}$ (anode) Cell 46
3.3.2 Terminal Voltage and Power Density 46
3.3.3 Ohmic Resistance and Overpotential 51
3.3.4 Reaction between GDC Powder and $SrRuO_3$ or Co_2RuO_4 Powder 56
3.4 Summary 60

References 62

CHAPTER 4 Electrochemical Properties of Anode-Supported SOFC with GDC Thin Film

4.1 Introduction 64

4.2 Experimental Procedure

4.2.1 Powder Preparation of SOFC Component 66

4.2.2 Fabrication of Anode-Supported SOFC by the Doctor-Blade Method 69

4.2.3 Measurement of Cell Performance 69

4.3 Results and Discussion

4.3.1 Microstructure of NiO-GDC / GDC Composite 70

4.3.2 Terminal Voltage and Power Density 70

4.3.3 Ohmic Resistance and Overpotential 76

4.4 Summary 78

References 82

CHAPTER 5 AC Impedance Spectra of Cathodes Used in the Solid Oxide Fuel Cells

5.1 Introduction 83

5.2 Experimental Procedure

Measurement of the Electrochemical Properties of the Cathode 83

5.3 Results and Discussion

5.3.1 AC Impedance Spectra Measured for ITO and $SrRuO_3$ Cathodes 84

5.3.2 AC Impedance Spectra Measured for Co_2RuO_4 and $SrRuO_3$ on 30 μm GDC Electrolyte 95

5.4 Summary 113

References 114

CHAPTER 6 Conclusions 115

List of Publications 119

Acknowledgements 120

Chapter 1
General Introduction

1.1 Solid Oxide Fuel Cell (SOFC)

Fuel cells are the high efficiency power generation system to convert chemical energy directly into electricity. They can reduce the amount of CO_2 emission without the formation of nitrogen oxides[1)]. Fuel cells are classified by the kinds of electrolyte materials as shown in Table 1.1[2)]. Alkaline fuel cell has been adopted for space craft and has the performance of several kW. Phosphoric acid fuel cell of 200 kW class has been commercialized. The plant of 1000 kW class of the molten carbonates fuel cell is under the proof test. Polymer electrolyte fuel cell has been developed for mobile application. Solid oxide fuel cell (SOFC), which is under the poof test, has the highest efficiency among the fuel cells shown in Table 1.1 because of its high temperature operation. The high temperature operation of SOFC enables the use of hydrocarbon fuel such as methane. Figure 1.1 shows the principal of power generation for SOFC. The oxygen molecules adsorbed on the cathode react with electrons to form oxide ions. The formed oxide ions diffuse into the electrolyte. The oxide ions transferred to the anode through the electrolyte react with the hydrogen at the anode, resulting in the formation of water vapor and electrons. The Gibbs free energy change of the formation of water vapor from the oxygen and hydrogen is expressed by Eq. (1.1),

$$\Delta G = \Delta G^{\circ} + RT \ln \frac{p_{H_2O}^2}{p_{H_2}^2 p_{O_2}(c)} \qquad (1.1)$$

where p_{H_2O}, p_{H_2} and $p_{O_2}(c)$ is the partial pressure of water vapor at the anode, hydrogen at the anode and oxygen at the cathode, respectively. In the equilibrium, the ΔG is equal to zero. Then the ΔG° is expressed using the equilibrium constant (K) by Eq. (1.2),

$$\Delta G^{\circ} = -RT \ln K \qquad (1.2)$$

The K value is related to the partial pressures of water vapor, hydrogen and oxygen gas in equilibrium state. When the water vapor, the hydrogen and the oxygen at the anode are in equilibrium, the ΔG is expressed using the oxygen partial pressures at the anode

Table 1.1 Electrolytes, electrodes and energy conversion of fuel cells.

		AFC Alkaline Fuel Cell	PAFC Phosphoric Acid Fuel Cell	MCFC Molten Carbonates Fuel Cell	SOFC Solid Oxide Fuel Cell	PEFC Polymer Electrolyte Fuel Cell
electrolyte	electrolyte	KOH	H_3PO_4	Li_2CO_3 K_2CO_3	YSZ ($ZrO_2 + Y_2O_3$)	cation exchange membrane
	conductor	OH^-	H^+	CO_3^{2-}	O^{2-}	H^+
	operation temperature	50 ~ 150 ℃	190 ~ 220 ℃	600 ~ 700 ℃	~ 1000 ℃	~ 200 ℃
electrode	catalysis	Ni-Ag	Pt	–	–	Pt
	anode reaction	$H_2 + 2OH^- \rightarrow 2H_2O + 2e^-$	$H_2 \rightarrow 2H^+ + 2e^-$	$H_2 + CO_3^{2-} \rightarrow H_2O + CO_2 + 2e^-$	$H_2 + O^{2-} \rightarrow H_2O + 2e^-$	$H_2 \rightarrow 2H^+ + 2e^-$
	cathode reaction	$1/2O_2 + H_2O + 2e^- \rightarrow 2OH^-$	$1/2O_2 + 2H^+ + 2e^- \rightarrow H_2O$	$1/2O_2 + CO_2 + 2e^- \rightarrow CO_3^{2-}$	$1/2O_2 + 2e^- \rightarrow O^{2-}$	$1/2O_2 + 2H^+ + 2e^- \rightarrow H_2O$
	total reaction	$H_2 + 1/2O_2 \rightarrow H_2O$	$H_2 + 1/2O_2 \rightarrow H_2O$	$H_2 + 1/2O_2 \rightarrow H_2O$	$H_2 + 1/2O_2 \rightarrow H_2O$	$H_2 + 1/2O_2 \rightarrow H_2O$
fuel		H_2	H_2	H_2, CO	H_2, CO	H_2
electric power		~ 10 kW	~ 1000 kW	~ 1000 kW	~ 100 kW	~ 250 kW
development situation		research	commercial	proof	proof	commercial
energy conversion efficiency		60 %	40 ~ 45 %	45 ~ 60 %	50 ~ 60 %	40 ~ 50 %

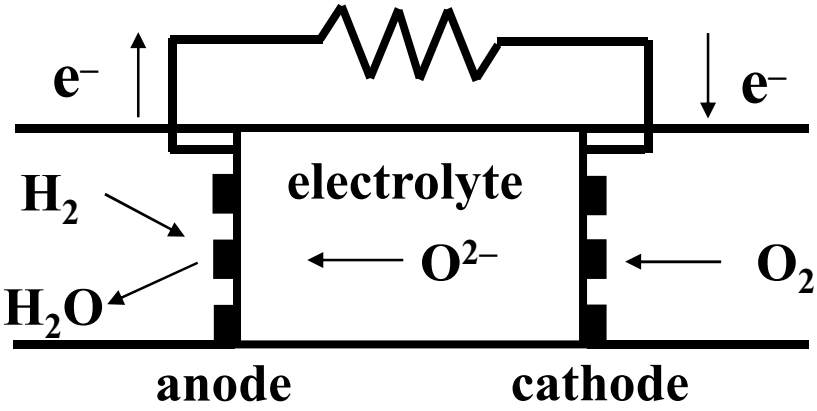

cathode	$O_2 + 4e^- \rightarrow 2O^{2-}$
anode	$2O^{2-} + 2H_2 \rightarrow 2H_2O + 4e^-$
total reaction	$2H_2 + O_2 \rightarrow 2H_2O$

$$R_2O_3 \xrightarrow{CeO_2} 2R'_{Ce} + 3O_O^{\times} + V_O^{\bullet\bullet}$$

(R : rare earth element)

$$E_0 = \frac{RT}{4F} \ln \frac{P_{O_2}(1)}{P_{O_2}(2)}$$

$Po_2(1)$: high oxygen partial pressure

$Po_2(2)$: low oxygen partial pressure

Fig. 1.1 Chemical reactions in SOFC.

($p_{O_2}(a)$) and the cathode ($p_{O_2}(c)$) by Eq. (1.3),

$$\Delta G = RT \ln \frac{p_{O_2}(a)}{p_{O_2}(c)} \tag{1.3}$$

On the other hand, the electromotive force (E) of the cell with 100 % oxide ion conductor is expressed by the Nernst equation and related with the ΔG by Eq. (1.4),

$$\Delta G = -nFE \tag{1.4}$$

where n and F is the mole number of electrons contributing to a reaction and Faraday constant, respectively. Then the E value is expressed using the $p_{O_2}(a)$ and the $p_{O_2}(c)$ by Eq. (1.5),

$$E = \frac{RT}{4F} \ln \frac{p_{O_2}(c)}{p_{O_2}(a)} \tag{1.5}$$

1.2 Purpose

Figure 1.2 shows the relationship between the terminal voltage (V) and the current (I). The terminal voltage decreases due to the ohmic resistances of the constituent materials of the cell and the overpotentials at the electrodes and is expressed by Eq. (1.6),

$$V = V_{OCV} - I(R_a + R_e + R_c) - (\eta_a + \eta_c) \tag{1.6}$$

where R_a, R_e and R_c are the resistance of the anode, electrolyte and cathode, respectively. η_a and η_c are the overpotential at the anode and the cathode, respectively. The overpotential is the voltage drops due to the charge transfer reactions and the diffusions of chemical species at the electrodes. The relationship between overpotential and current density is not linear. If the electrolyte is the pure ionic conductor, the V_{OCV} value corresponds to the E value expressed by Eq. (1.5). The cell performance is enhanced by the decrease of the ohmic resistances and the overpotentials. The proposed SOFC consists of yttria-stabilized zirconia (YSZ) electrolyte, Ni/YSZ cermet anode, $La_{1-X}Sr_XMnO_3$ (LSM) cathode, and $LaCrO_3$ interconnector[3]. This system is operated at 973 – 1273 K to enhance the diffusion of oxide ions. The oxide ion conductivity of YSZ is about 0.1 S/cm at 1273 K and is lower than the electrical conductivities of Ni/YSZ or LSM by a factor of about $1/10^4$. The increase of oxide ion conductivity and the

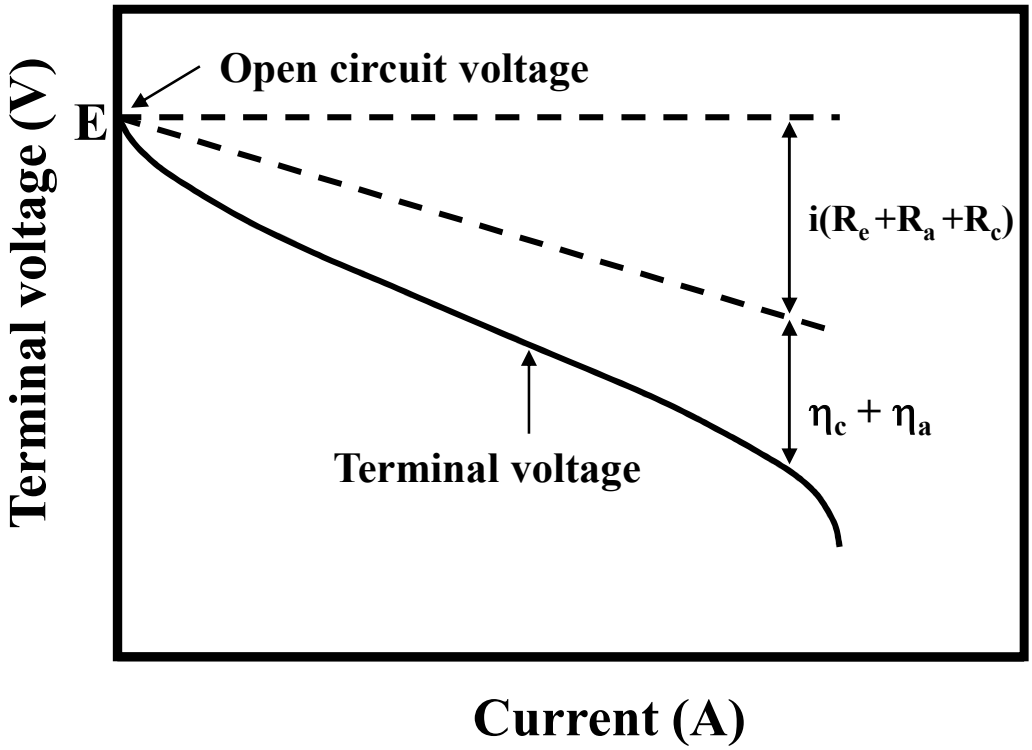

Fig. 1.2 Relationship between terminal voltage and current.

decrease of the thickness of solid electrolyte, lead to the decrease of operation temperature of SOFC as shown in Fig. 1.3. Figure 1.3 shows the oxide ion conductivities and the thickness required to obtain a specific area resistance of 0.1 $\Omega \cdot cm^2$ for YSZ[4] and Gd-doped ceria (GDC)[5]. The decrease of the operation temperature increases the lifetime of SOFC and expands the choice of constituent materials used for the electrodes and interconnector. It is reported that rare earth-doped ceria (RDC) has a higher oxide ion conductivity than YSZ and the transference number of oxide ion in RDC favorably approaches unity with decreasing temperature[3]. That is, RDC is a candidate of solid electrolyte for the low temperature operation of SOFC[6)-10)]. On the other hand, the ohimc resistance of the electrolyte as well as overpotentials at the electrodes increases at low temperatures of SOFC. Table 1.2 shows the cell performance reported by the literatures[11)-16)]. The cells with the higher power density have the thinner electrolyte supported by the anode. The comparison among the references[11)-13)] shows that the maximum power densities are greatly influenced by the kinds of cathodes. It is also reported that the polarization losses for the O_2 reduction on the cathode are particularly high due to the relatively high activation energy and relatively slow reaction rates as compared with those of H_2 oxidation on the anode[17),18)]. On the other hand, the open circuit voltages of the cells with the RDC electrolytes are lower than that of the cell with the YSZ electrolyte, which is attributed to the electronic conduction of the RDC electrolyte.

This thesis mainly comprises the electronic conductivity of rare earth-doped ceria, the electrochemical properties of the cells with the different cathodes, the fabrication of the thin electrolyte film by the doctor-blade method and the cell performance of the anode-supported SOFC.

References

1) B. C. H. Steele, Nature, 400, 619-621 (1999).

2) Y. Miyazaki, Bull. Ceram. Soc. Jpn., 30, 322-328 (1995).

3) K. Eguchi, J. Alloys and Compounds, 250 [3], 486-491 (1997).

4) J.H. Park and R.N. Blumenthal, J. Electrochem. Soc., 136, 2867-2876 (1989).

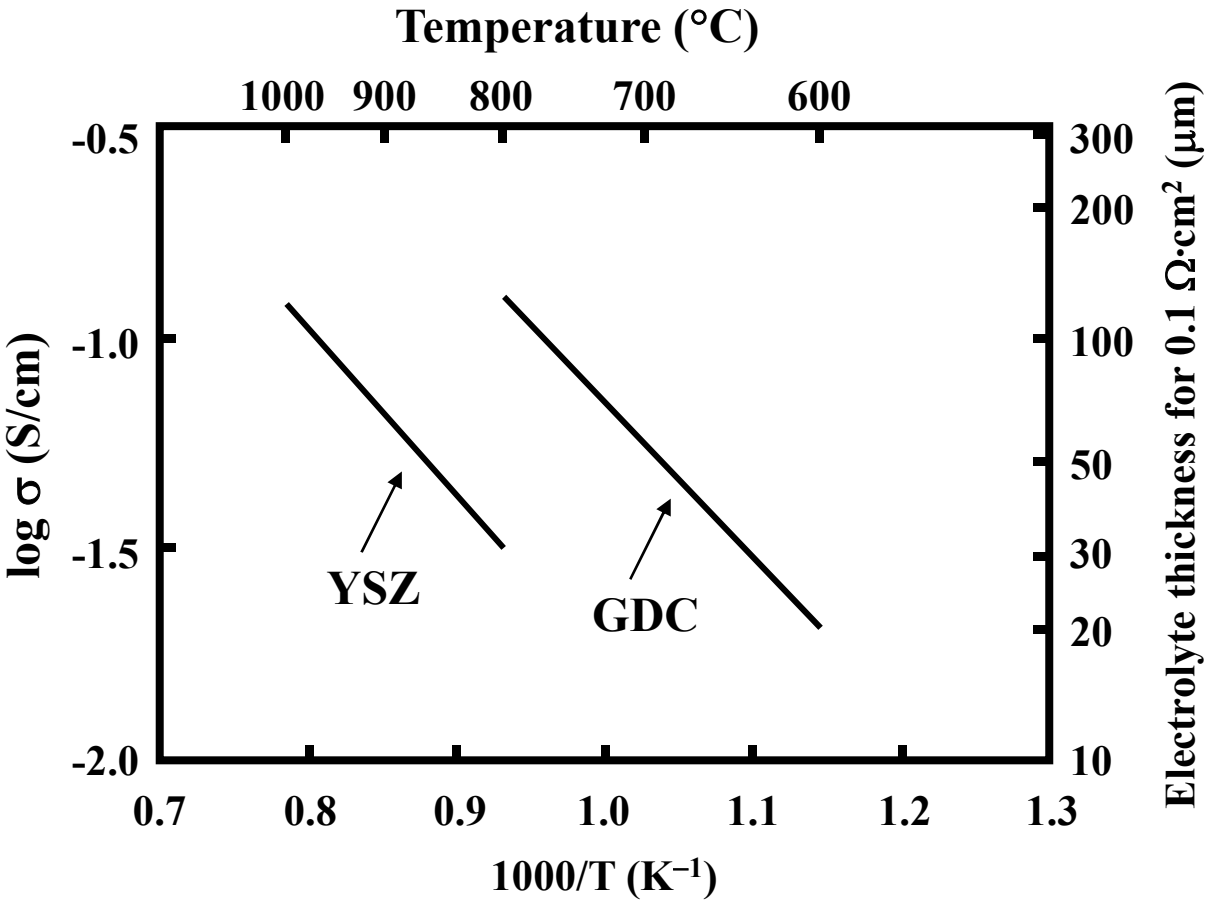

Fig. 1.3 Oxide ion conductivity (σ) and electrolyte thickness required to obtain a specific area resistance of 0.1 Ω·cm² for YSZ and GDC.

Table 1.2 Comparison of cell performance.

Electrolyte (thickness (μm))	SDC (20)	SDC (19)	GDC (10)	YSZ (13)	SDC (6.5) / ScSZ (1)	LSGM (5) / SDC (0.4)
Cathode (thickness (μm))	BSCF (10-20)	SSC-SDC (30)	LSCF-GDC (30)	LSM-SDC (20)	SSC-SDC (45)	SSC
anode (thickness (μm))	Ni-SDC (700) 60wt%NiO	Ni-SDC (12) Ni-YSZ (900) 57wt%NiO	Ni-GDC 65wt%NiO	Ni-YSZ 50wt%NiO	Ni-SDC(15) Ni-YSZ(800) 41 vol% Ni	Ni-Fe-SDC
Fuel (flux (ml/min))	3%H_2O-H_2 (80)	3%H_2O-H_2 (100)	3%H_2O-H_2 (86)	H_2	3vol%H_2O- H_2 (100)	H_2 (120)
Oxidant (flux (ml/min))	Air (400)	Air (100)	Air (stationary)	Air (stationary)	Air (100)	O_2 (120)
Temperature (K)	773, 873	773, 873	773, 873	873, 973, 1073	773, 873, 973	773, 873, 973
OCV (V)	0.92, 0.85	0.94, 0.88	0.95, 0.86	1.1	1.0-1.1	0.9, 1.0, 1.1
MPD (mW/cm^2)	402, 1010	253, 749	167, 578	334, 773, 1252	250, 900, 1600	612, 1951, 3270
Processing of electrolyte	Dry pressing	Screen printing	Spray coating	Slurry spin coating	PLD	PLD
Reference	11	12	13	14	15	16

OCV : Open circuit voltage, MPD : Maximum power density, SDC : Sm-doped Ceria, GDC : Gd-doped ceria, YSZ : Yttria-stabilized zirconia ScSZ : Sc_2O_3-stabilized zirconia, LSGM : $La_{0.9}Sr_{0.1}Ga_{0.8}Mg_{0.2}O_3$, BSCF : $Ba_{0.5}Sr_{0.5}Co_{0.8}Fe_{0.2}O_{3-delta}$, SSC : Sr-doped samarium cobaltite, PLD : Pulsed laser deposition

5) S. Sameshima, H. Ono, K. Higashi, K. Sonoda, Y. Hirata and Y. Ikuma, J. Ceram. Soc. Japan, 108 [12], 1060-1066 (2000).
6) T. H. Etsell and S. N. Flengas, Chem. Rev., 70 [3], 339-376 (1970).
7) T. Kubo and H. Obayashi, J. Electrochem. Soc., 122 [1], 142-147 (1975).
8) H. L. Tuller and A. S. Nowich, J. Electrochem. Soc., 122 [2], 255-259 (1975).
9) R. T. Dirstine, R. N. Blumenthal and T. F. Kuech, J. Electrochem. Soc., 126 [2], 264-269 (1979).
10) H. Inaba and H. Tagawa, Solid State Ionics, 83 [1], 1-16 (1996).
11) Z. Shao and S. M. Haile, Nature, 431, 170-173 (2004).
12) X. Zhang, M. Robertson, S. Yick, C. Deĉes-Petit, E. Styles, W. Qu, Y. Xie, R. Hui, J. Roller, O. Kesler, R. Maric and D. Ghosh, Journal of Power Sources, 160, 1211-1216 (2006).
13) Y.J. Leng, S.H. Chan, S.P. Jiang, K.A. Khor, Solid State Ionics, 170, 9-15 (2004).
14) K. Chen, Z. Lü, H. Ai, X. Chen, J. Hu, X. Huang and W. Su, Journal of Power Sources, 167, 84-89 (2007).
15) D. Yang, X. Zhang, S. Nikumb, C. Decès-Petit, R. Hui, R. Maric and D. Ghosh, Journal of Power Sources, 164, 182-188 (2007).
16) J. Yan, H. Matsumoto, M. Enoki and T. Ishihara, Electrochemical and Solid-State Letters, 8 [8], A389-A391 (2005).
17) S.P. Jiang and S.P.S. Badwal, Solid State Ionics 123, 209-224 (1999).
18) S.P. Jiang, J.G. Love and Y. Ramprakash, Journal of Power Sources 110, 201-208 (2002).

Chapter 2

Electronic Conductivity of Rare Earth-Doped Ceria Ceramics

2.1 Introduction

The problem pointed out on rare earth-doped ceria (RDC) is the increased electronic conduction at a low oxygen partial pressure, which is accompanied by the reduction of Ce^{4+} to Ce^{3+}. The oxygen partial pressure at which the ionic conductivity is equal to the electronic conductivity, has been reported as follows at 1073 K : 10^{-10} Pa for $Ce_{0.8}Sm_{0.2}O_{1.9}$[1)], 10^{-8} Pa for $Ce_{0.8}Gd_{0.2}O_{1.9}$[1)], and 10^{-12} Pa for $Ce_{0.8}Gd_{0.2}O_{1.9}$[2)] and 10^{-11} Pa for $Ce_{0.9}Gd_{0.1}O_{1.95}$[2)]. In our previous work[3)], the transference number of oxide ion for $Ce_{0.8}R_{0.2}O_{1.9}$ (R=Gd, Sm) was measured to be 0.83-0.85 at 973 K under an oxygen pressure of 10^{-15} Pa and was relatively high as compared with the values reported above. This paper reports on the measurement of electronic conductivity of $Ce_{0.8}La_{0.2}O_{1.9}$ (lanthanum-doped ceria, LDC) by direct current (DC) polarization method using a Hebb-Wagner ion blocking cell. The measured data were compared with the oxide ion conductivity[4)] to determine the transference number of oxide ions and also compared with the previously measured electronic conductivity of the Gd- and Sm-doped ceria[3)].

2.2 Experimental Procedure

2.2.1. Sample Preparation

The detailed powder preparation method of LDC with a composition $Ce_{0.8}La_{0.2}O_{1.9}$ is reported in our previous papers[5), 6)]. The oxalate solid solution $(Ce_{0.8}La_{0.2})_2(C_2O_4)_3$ was produced at room temperature by adding the mixed nitrate solution (0.2 M) of Ce and La into a 0.4 M oxalic acid solution. The formation of the solid solution was examined by X-ray diffraction and thermogravimetric differential thermal analysis (TG-DTA). The coprecipitated oxalate powder decomposed to polycrystalline oxide solid solution by heating to 873 K. The produced LDC powder gave 36.2 m^2/g of specific surface area, which corresponded to 24 nm diameter of spherical primary particles[6)]. As-prepared LDC powders were compacted isostatically under a pressure of

294 MPa to a pellet of 10 mm in diameter and 2 mm in thickness. The sintering at 1773 K for 4 h in air (SPM 6512 electric furnace, Marusho Electro-Heat Co., Ltd., Japan) gave dense compacts with 96-97 % of theoretical density. The open pores were 0.1-0.8 % and the closed pores were 1.8-3.5 %. As-sintered samples were polished with diamond paste of 1 μm.

2.2.2. Measurement of Electronic Conductivity by the Hebb-Wagner Method

The electronic conductivity was measured by DC polarization using a Hebb-Wagner ion blocking cell[7] in the temperature range from 773 to 1113 K under the oxygen partial pressure range of Po_2 = 10^4-10^{-22} Pa. The ion blocking cell is schematically shown in Fig. 2.1. Au paste (TR-1301, Tanaka Kikinzoku Kogyo Co., Japan) was painted on both surfaces of a disk sample with 8 mm diameter and 1.5 mm thickness and fired at 1223 K in air. The Au electrode surface area was 0.1-0.2 cm^2. The sample with Au electrodes was attached to a high purity alumina holder (Al_2O_3 > 99.99 mass%) using glass O-ring with a chemical composition (mass%) of 81SiO_2, 2Al_2O_3, 13B_2O_3 and 4Na_2O-K_2O (HV10R, softening temperature 1094 K, Iwaki Glass Co., Japan). The sample on the O-ring was heated to 1223 K under the application of the stress through a SiO_2-Al_2O_3 tube and cooled to 773-1113 K to measure the electronic conductivity. Platinum wire in the alumina holder was sealed with a glass powder of the SiO_2-B_2O_3-RO (R : alkaline-earth metal) system (ASF1761, softening temperature 1143 K, Asahi Glass Co., Ltd., Japan). The DC polarization measurement was performed with potentiometer (HA-501G, Hokuto Denko Co., Japan). The applied voltage (E) varied from 0.01 to 1.0 V. When the voltage was applied to the sample, the oxygen gas inside of the sealed holder is exhausted through LDC sample toward the outer side. In the steady state, the oxygen chemical potential at the inner Au electrode/sample interface is reduced against the outer Au electrode (reversible electrode). However, the oxide ion flow is blocked at the inner electrode because of the applied potential difference (See Section 2.3.1.). The measured current should be electronic current, governed by electrons or holes in the sample. The electromotive force after the electronic conductivity measurement of LDC sample was measured to check the leakage of oxygen molecules in air into the sealed holder. The electromotive force decreased from

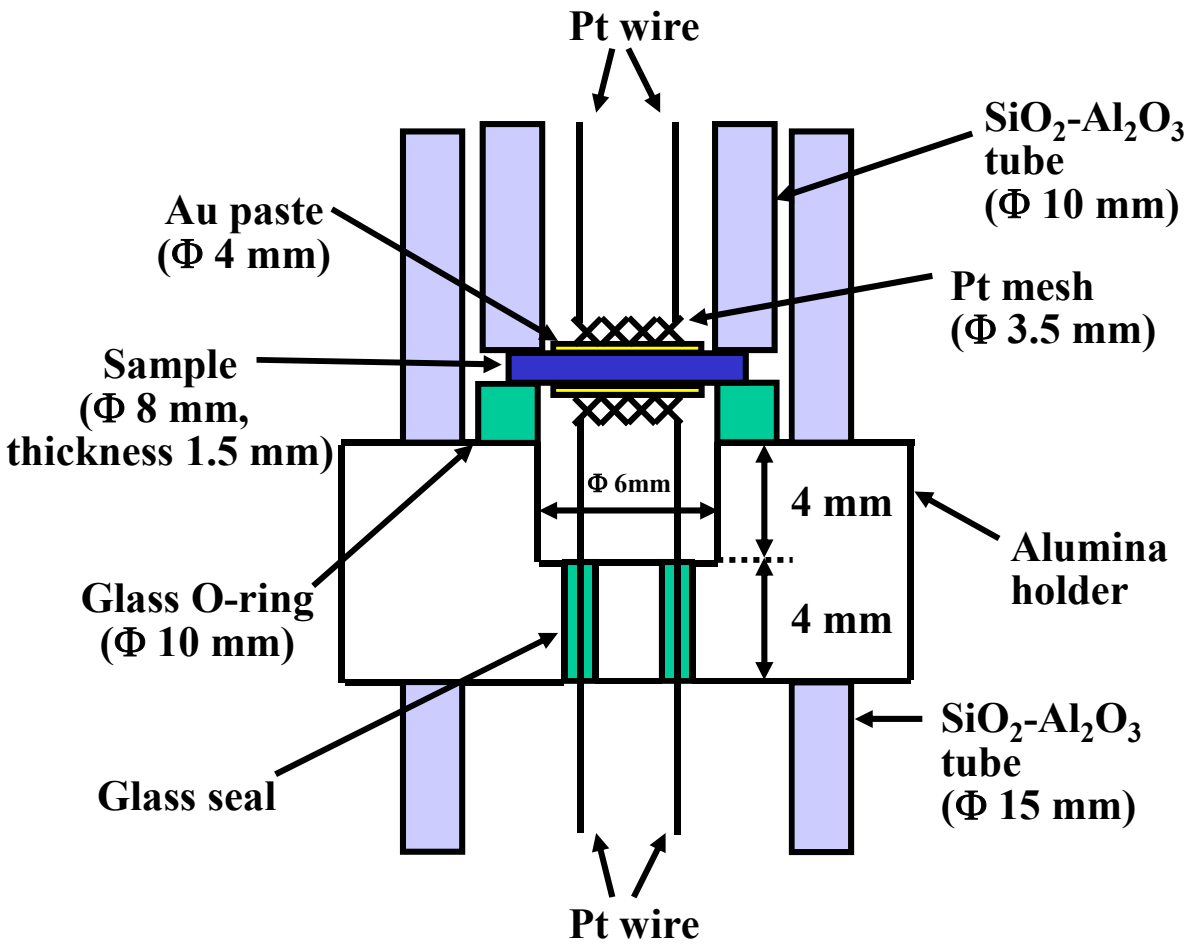

Fig. 2.1 Schematic diagram of Hebb-Wagner ion blocking cell.

0.954 V at the initial time to 0.23 V after 1 h at 773 K. This result is due to the leakage of oxygen molecules in air into the holder. The amount of the leaking oxygen molecules was calculated from the electromotive force, oxygen partial pressure at the inside of the holder and the inside volume of the sealed holder (5×10^{-8} m^3). The calculated amount of leaked oxygen molecules was converted to the oxide ion current. The leaked oxide ion current was 1.8×10^{-11} A at 773 K. The ratio of the leaked oxide ion current to the electronic current measured at 0.07-1.01 V of applied voltage was in the range from 2.0×10^{-4} to 2.6×10^{-7}. The above ratio indicates that the leakage of the oxygen molecules gave no significant influence of the electronic conductivity measurement in this experiment.

2.3 Theoretical Approach to Electronic Conduction

2.3.1. Electronic Conductivity and Applied Voltage

The electronic conductivity (σ_e) of a thin LDC layer under a homogeneous atmosphere of a low oxygen partial pressure is expressed by Eq. (2.1) as a function of oxygen partial pressure (Po_2),

$$\sigma_e = C_1 P_{O_2}^{-1/n} \tag{2.1}$$

where C_1 and n are the constants. The oxygen partial pressure at the inner and outer electrodes of sample in Fig. 2.1 is related to the applied voltage (E), Faraday constant (F), gas constant (R) and temperature (T) by Eq. (2.2) (Nernst equation),

$$E = \frac{RT}{4F} \ln \frac{P_{O_2}(\text{outer})}{P_{O_2}(\text{inner})} \tag{2.2}$$

The LDC sample in Fig. 2.1 is interpreted to be a multilayer structure consisting of different single layer defined by Eq. (2.1) at a different oxygen partial pressure. The electronic conductivity of LDC sample in Fig. 2.1 is defined by Eq. (2.3),

$$\sigma_e = \frac{L}{A}\left(\frac{dI}{dE}\right) \tag{2.3}$$

where A is the surface area of electrode, L the thickness of sample and I the electronic current. In a Hebb-Wagner ion blocking cell where oxide ion flow is blocked, the applied voltage is related to the chemical potential of oxygen atom ($\mu(O)$) in the LDC

sample as follows : $dE = -(1/2F)d\mu(O)$.

Substitution of the above relation into Eq. (2.3) provides Eq. (2.4),

$$dI = -\frac{A}{2FL}\sigma_e d\mu(O) \tag{2.4}$$

Furthermore, the chemical potential of oxygen atom in the LDC sample is related to the corresponding oxygen partial pressure (Po_2 (inside)) at the inside of the sample by Eq. (2.5),

$$d\mu(O) = \frac{1}{2}RT\, d\ln P_{O_2}(\text{inside}) \tag{2.5}$$

Combination of Eqs. (2.4) and (2.5) gives Eq. (2.6),

$$dI = -\frac{ART}{4FL}\sigma_e\ d\ln P_{O_2}(\text{inside}) \tag{2.6}$$

Integration of Eq. (2.6) between I = I (outer) at $Po_2 = Po_2$ (outer) and I = I (inner) at $Po_2 = Po_2$ (inner) results in Eq. (2.7),

$$I(\text{inner}) - I(\text{outer}) = -\frac{ART}{4FL}\int_{\ln P_{O_2}(\text{outer})}^{\ln P_{O_2}(\text{inner})}\sigma_e\ d\ln P_{O_2}(\text{inside}) \tag{2.7}$$

where σ_e is equal to Eq. (2.1). Equation (2.7) indicates that the electronic current of LDC sample depends on the oxygen partial pressure at the inner electrode, because Po_2 (outer) is equal to 0.21×10^5 Pa in air. On the other hand, the oxygen partial pressure at the inside of LDC sample (Po_2 (inside)) also satisfies Eq. (2.2) and $d\ln Po_2$ (inside) is expressed by Eq. (2.8),

$$d\ln P_{O_2}(\text{inside}) = -\frac{4F}{RT}dE \tag{2.8}$$

Finally, substitution of Eqs. (2.1), (2.2) and (2.8) into Eq. (2.6) gives Eq. (2.9),

$$I = \frac{A}{L}\int_0^E C_1 P_{O_2}(\text{inside})^{-1/n}dE = \frac{AC_1P_{O_2}(\text{outer})^{-1/n}}{L}\int_0^E \exp\left(\frac{4FE}{nRT}\right)dE$$

$$= \frac{nAC_1RTP_{O_2}(\text{outer})^{-1/n}}{4FL}\left[\exp\left(\frac{4FE}{nRT}\right)-1\right] \tag{2.9}$$

Equation (2.9) represents the I-E relation for the electronic conduction. Differential of Eq. (2.9) with respect to E results in Eq. (2.10),

$$\sigma_e = C_1 P_{O_2}(\text{outer})^{-1/n} \exp\left(\frac{4FE}{nRT}\right) \tag{2.10}$$

Equation (2.10) indicates a linear relation between ln σ_e and E.

2.3.2. Possible Interactions between Rare Earth-Doped Ceria and Electron

The substitution of R for Ce in CeO_2 fluorite structure produces oxygen vacancy by Eq. (2.11),

$$R_2O_3 \xrightarrow{CeO_2} 2R'_{Ce} + 3O_O^{\times} + V_O^{\bullet\bullet} \tag{2.11}$$

On the other hand, the possible interaction between electron and Ce site or O site in RDC at a low oxygen partial pressure was divided into the following four cases expressed by Eqs. (2.12), (2.14), (2.16) and (2.18). The equilibrium constant K for Eqs. (2.12), (2.14), (2.16) and (2.18) is expressed by Eqs. (2.13), (2.15), (2.17) and (2.19), respectively.

·Case I

$$O_O^{\times} \rightleftarrows V_O^{\bullet\bullet} + 2e' + \frac{1}{2}O_2 \tag{2.12}$$

$$K_I = \frac{[V_O^{\bullet\bullet}][e']^2 P_{O_2}^{1/2}}{[O_O^{\times}]} \tag{2.13}$$

·Case II

$$Ce_{Ce}^{\times} + O_O^{\times} \rightleftarrows Ce'_{Ce} + V_O^{\bullet\bullet} + e' + \frac{1}{2}O_2 \tag{2.14}$$

$$K_{II} = \frac{[Ce'_{Ce}][V_O^{\bullet\bullet}][e']P_{O_2}^{1/2}}{[Ce_{Ce}^{\times}][O_O^{\times}]} \tag{2.15}$$

·Case III

$$2Ce_{Ce}^{\times} + O_O^{\times} \rightleftarrows 2Ce'_{Ce} + V_O^{\bullet\bullet} + \frac{1}{2}O_2 \tag{2.16}$$

$$K_{III} = \frac{[Ce'_{Ce}]^2[V_O^{\bullet\bullet}]P_{O_2}^{1/2}}{[Ce_{Ce}^{\times}]^2[O_O^{\times}]} \tag{2.17}$$

·Case IV

$$Ce_{Ce}^{\times} + 2O_O^{\times} \rightleftarrows Ce'_{Ce} + 2V_O^{\bullet\bullet} + 3e' + O_2 \quad (2.18)$$

$$K_{IV} = \frac{[Ce'_{Ce}][V_O^{\bullet\bullet}]^2[e']^3 P_{O_2}}{[Ce_{Ce}^{\times}][O_O^{\times}]^2} \quad (2.19)$$

The charge neutrality condition for each case in consideration of Eq. (2.11) is expressed by Eqs. (2.20)-(2.23).

·Case I $2[V_O^{\bullet\bullet}] = [R'_{Ce}] + [e']$ (2.20)

·Case II $2[V_O^{\bullet\bullet}] = [R'_{Ce}] + [Ce'_{Ce}] + [e']$ (2.21)

·Case III $2[V_O^{\bullet\bullet}] = [R'_{Ce}] + [Ce'_{Ce}]$ (2.22)

·Case IV $2[V_O^{\bullet\bullet}] = [R'_{Ce}] + [Ce'_{Ce}] + [e']$ (2.23)

In case I (Eq. (2.12)), the release of lattice oxide ion produces free electron and positively charged oxide ion vacancy. In case II (Eq. (2.14)) and IV (Eq. (2.18)), the reaction between lattice Ce^{4+} ion and lattice O^{2-} ion produces Ce^{3+} ion, positively charged oxide ion vacancy and free electron. In case III, no free electron is formed by the reaction between lattice Ce^{4+} ion and lattice O^{2-} ion. The charge neutrality condition of each case (Eqs. (2.20)-(2.23)) was approximated to (a) $2[V_O^{\bullet\bullet}] \approx [R'_{Ce}]$, (b) $2[V_O^{\bullet\bullet}] \approx [e']$ and (c) $2[V_O^{\bullet\bullet}] \approx [Ce'_{Ce}]$ to understand the oxygen partial pressure dependence of $[e']$ or $[Ce'_{Ce}]$. In case I, the substitution of $2[V_O^{\bullet\bullet}] = [R'_{Ce}]$ into Eq. (2.13) gives Eq. (2.24),

$$[e'] = (2K_1)^{1/2}\left(\frac{[O_O^{\times}]}{[R'_{Ce}]}\right)^{1/2} P_{O_2}^{-1/4} \quad (2.24)$$

Similarly, the approximation of $2[V_O^{\bullet\bullet}] = [e']$ (condition (b)) in Eq. (2.13) provides Eq. (2.25),

$$[e'] = (2K_1)^{1/3}[O_O^{\times}]^{1/3} P_{O_2}^{-1/6} \quad (2.25)$$

Equations (2.24) and (2.25) indicate a linear relationship with −1/4 and −1/6 of slope in the log $[e']$-log Po_2 plot, respectively. The detailed oxygen partial pressure dependence of $[e']$ for cases I, II and IV is summarized in Table 2.1. “No hopping” in cases II and IV corresponds to no possibility of movement of the electron trapped on a lattice Ce^{4+} ion (Ce'_{Ce}) to a neighboring Ce^{4+} ion. On the other hand, “Hopping” indicates that the movement of the electron trapped on a Ce^{4+} ion to a neighboring Ce^{4+} ion is allowed. In

Table 2.1, the hopping electron was treated as an identical electron to free electron ($Ce'_{Ce} = e'$). As seen in Table 2.1, the different dependence of $[e']$ on oxygen partial pressure is expected for "No hopping" and "Hopping" in the conditions (a), (b) and (c). Furthermore, the same equation of $[e']$ in (b) and (c) conditions is derived for "Hopping" of Ce^{3+} ion. In case III, the electronic conductivity by hopping of the electron on Ce^{4+} ion is proportional to $Po_2^{-1/4}$ in the condition (a) and $Po_2^{-1/6}$ in the condition (c). The experimentally measured electronic conductivity with oxygen partial pressure can be compared with the proposed possibility of electronic conductivity in Table 2.1. In condition (a), the concentrations of free electron and hopping electron are proportional to $Po_2^{-1/4}$ in cases I-IV. In conditions (b) and (c), $[e']$ is proportional to $Po_2^{-1/6}$ in cases I-IV for hopping electron.

2.4 Results and Discussion

2.4.1. Electronic Conductivity

Figure 2.2 shows the relationship between applied voltage (E) and electronic current density (I) for LDC at (a) 773, (b) 873, (c) 973 and (d) 1113 K. The I value increased nonlinearly with an increase in E value. This result is explained by the influence of E (2nd term) in the right side of Eq. (2.9). The increase of E enhances the electronic conductivity.

Figure 2.3 shows the relationship between ln σ_e (electronic conductivity) and E (applied voltage) for LDC at (a) 773, (b) 873, (c) 973 and (d) 1113 K. The electronic conductivity was determined from the data in Fig. 2.2 and Eq. (2.3), $\sigma_e = L\Delta I / A\Delta E$, where ΔE was divided into 20 mV. The sample showed two straight lines with 0.982-1.000 of the correlation coefficient in a wide applied voltage range of 0.2-1.0 V. This result supports the relationship predicted by Eq. (2.10) for the measured electronic conductivity. From the slopes of the straight lines in Fig. 2.3, the n value in Eq. (2.10) was determined and shown in Fig. 2.3. Table 2.2 summarizes the experimental constants C_1 and n values in Eq. (2.10). The n values measured for LDC was 4.3-4.6 in the applied voltage range from 0.2 to 0.6 V and 6.7-7.1 in the applied voltage range from 0.7 to 1.0 V. The solid lines in Fig. 2.2 represent Eq. (2.9), where n and C_1 values were

Table 2.1 Possible interactions between electron and Ce and O sites in La-doped ceria and oxygen partial pressure dependence of concentration of electron.

Case	Charge neutrality condition		
	(a) $2[V_O^{\cdot\cdot}] \approx [R_{Ce}']$	(b) $2[V_O^{\cdot\cdot}] \approx [e']$	(c) $2[V_O^{\cdot\cdot}] \approx [Ce_{Ce}']$
[I] $O_O^{\times} \rightleftarrows V_O^{\cdot\cdot} + 2e' + \frac{1}{2}O_2$ $K_I = \frac{[V_O^{\cdot\cdot}][e']^2 Po_2^{1/2}}{[O_O^{\times}]}$	$[e'] = (2K_I)^{1/2}\left[\frac{[O_O^{\times}]}{[R_{Ce}']}\right]^{1/2} Po_2^{-1/4}$	$[e'] = (2K_I)^{1/3}[O_O^{\times}]^{1/3} Po_2^{-1/6}$	
[II] $Ce_{Ce}^{\times} + O_O^{\times} \rightleftarrows Ce_{Ce}' + V_O^{\cdot\cdot} + e' + \frac{1}{2}O_2$ $K_{II} = \frac{[Ce_{Ce}'][V_O^{\cdot\cdot}][e']Po_2^{1/2}}{[Ce_{Ce}^{\times}][O_O^{\times}]}$	No hopping $[e'] = 2K_{II}\frac{[Ce_{Ce}^{\times}][O_O^{\times}]}{[Ce_{Ce}'][R_{Ce}']} Po_2^{-1/2}$	No hopping $[e'] = (2K_{II})^{1/2}\left[\frac{[Ce_{Ce}^{\times}][O_O^{\times}]}{[Ce_{Ce}']}\right]^{1/2} Po_2^{-1/4}$	No hopping $[e'] = 2K_{II}\frac{[Ce_{Ce}^{\times}][O_O^{\times}]}{[Ce_{Ce}']^2} Po_2^{-1/2}$
	Hopping $[e'] = (2K_{II})^{1/2}\left[\frac{[Ce_{Ce}^{\times}][O_O^{\times}]}{[R_{Ce}']}\right]^{1/2} Po_2^{-1/4}$	Hopping $[e'] = (2K_{II})^{1/3}([Ce_{Ce}^{\times}][O_O^{\times}])^{1/3} Po_2^{-1/6}$	Hopping $[e'] = (2K_{II})^{1/3}([Ce_{Ce}^{\times}][O_O^{\times}])^{1/3} Po_2^{-1/6}$
[III] $2Ce_{Ce}^{\times} + O_O^{\times} \rightleftarrows 2Ce_{Ce}' + V_O^{\cdot\cdot} + \frac{1}{2}O_2$ $K_{III} = \frac{[Ce_{Ce}']^2[V_O^{\cdot\cdot}]Po_2^{1/2}}{[Ce_{Ce}^{\times}]^2[O_O^{\times}]}$	$[Ce_{Ce}'] = (2K_{III})^{1/2}\left[\frac{[Ce_{Ce}^{\times}]^2[O_O^{\times}]}{[R_{Ce}']}\right]^{1/2} Po_2^{-1/4}$		$[Ce_{Ce}'] = (2K_{III})^{1/3}([Ce_{Ce}^{\times}]^2[O_O^{\times}])^{1/3} Po_2^{-1/6}$
[IV] $Ce_{Ce}^{\times} + 2O_O^{\times} \rightleftarrows Ce_{Ce}' + 2V_O^{\cdot\cdot} + 3e' + O_2$ $K_{IV} = \frac{[Ce_{Ce}'][V_O^{\cdot\cdot}]^2[e']^3 Po_2}{[Ce_{Ce}^{\times}][O_O^{\times}]^2}$	No hopping $[e'] = (4K_{IV})^{1/3}\left[\frac{[Ce_{Ce}^{\times}][O_O^{\times}]^2}{[Ce_{Ce}'][R_{Ce}']^2}\right]^{1/3} Po_2^{-1/3}$	No hopping $[e'] = (4K_{IV})^{1/5}\left[\frac{[Ce_{Ce}^{\times}][O_O^{\times}]^2}{[Ce_{Ce}']}\right]^{1/5} Po_2^{-1/5}$	No hopping $[e'] = (4K_{IV})^{1/3}\left[\frac{[Ce_{Ce}^{\times}][O_O^{\times}]^2}{[Ce_{Ce}']^3}\right]^{1/3} Po_2^{-1/3}$
	Hopping $[e'] = (4K_{IV})^{1/4}\left[\frac{[Ce_{Ce}^{\times}][O_O^{\times}]^2}{[R_{Ce}']^2}\right]^{1/4} Po_2^{-1/4}$	Hopping $[e'] = (4K_{IV})^{1/6}([Ce_{Ce}^{\times}][O_O^{\times}]^2)^{1/6} Po_2^{-1/6}$	Hopping $[e'] = (4K_{IV})^{1/6}([Ce_{Ce}^{\times}][O_O^{\times}]^2)^{1/6} Po_2^{-1/6}$

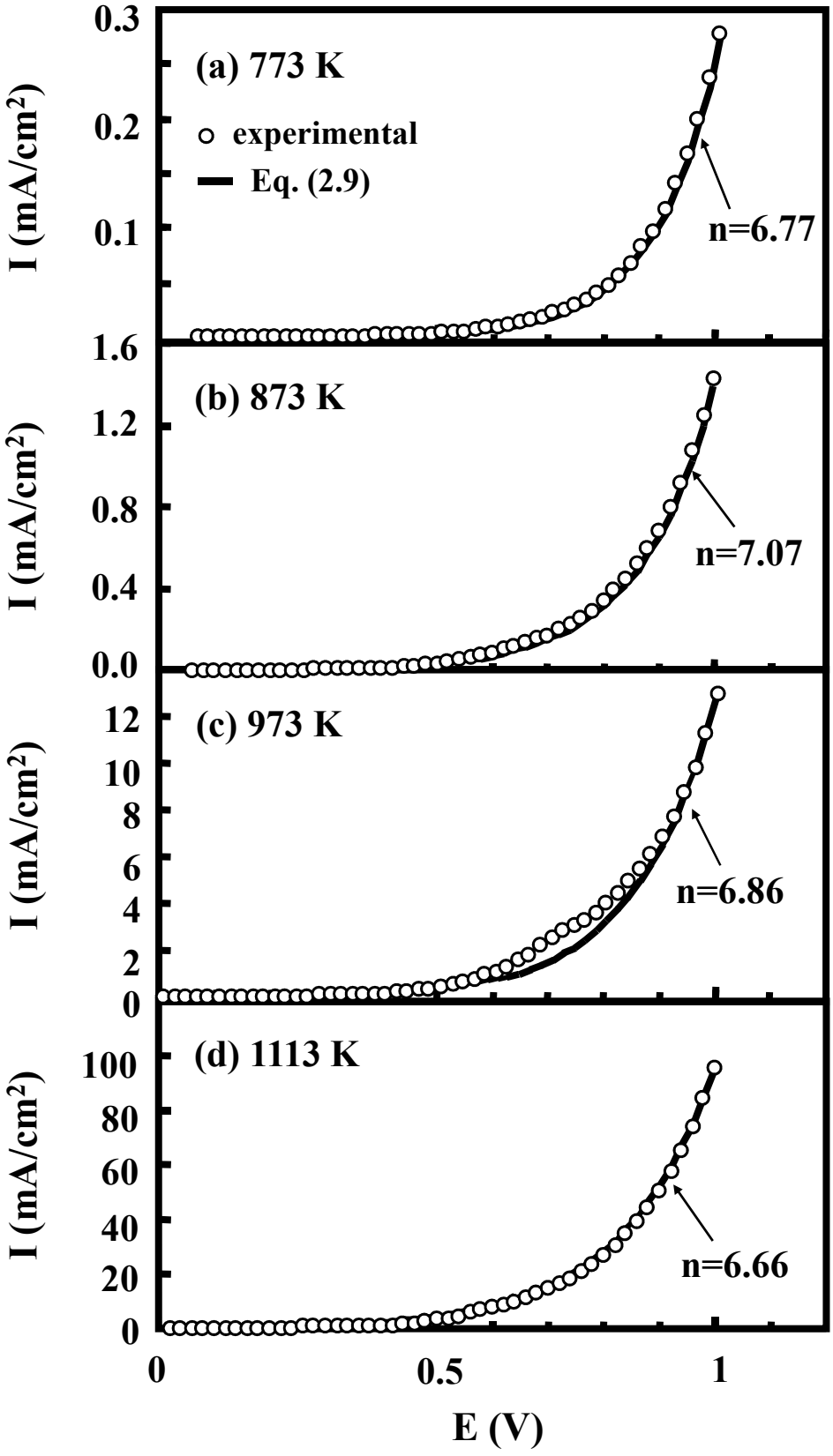

Fig. 2.2 Relationship between applied voltage (E) and electronic current density (I) for LDC at (a) 773 K, (b) 873 K, (c) 973 K and (d) 1113 K. The solid lines in Fig. 2.2 correspond to Eq. (2.9) in text.

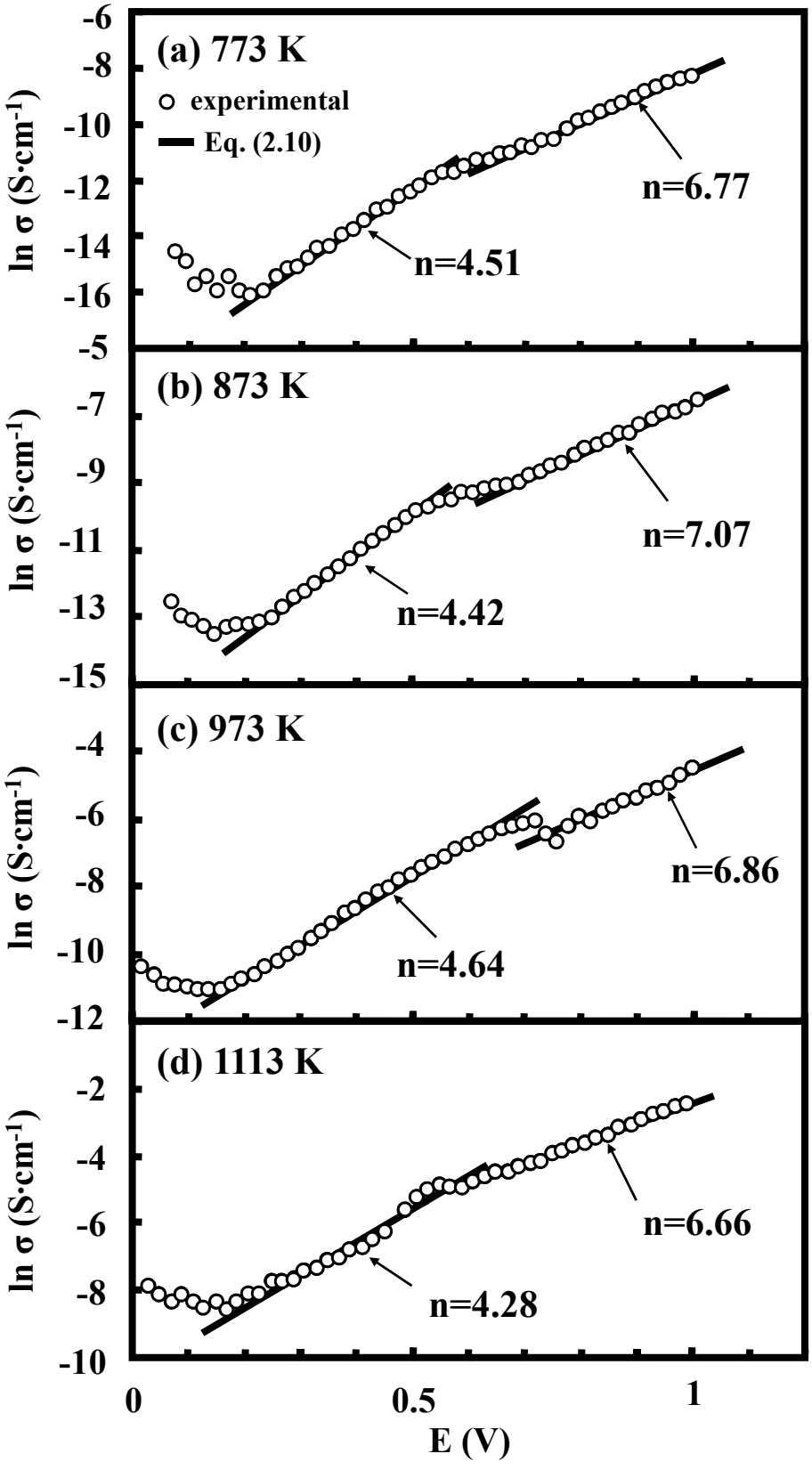

Fig. 2.3 Logarithmic electronic conductivity and applied voltage for LDC at (a) 773 K, (b) 873 K, (c) 973 K and (d) 1113 K. The straight lines express Eq. (2.10) in text.

Table 2.2 Experimental constants C_1 and n values in electronic conductivity, $\sigma_e = C_1 Po_2^{-1/n}$ for LDC.

Temperature (K)	C_1 ($S \cdot cm^{-1}$)	n (–)	Oxygen partial pressure range (Pa)
773	3.74×10^{-9}	4.51	$10^{-1.4}$ - $10^{-8.1}$
773	2.89×10^{-8}	6.77	$10^{-12.4}$ - 10^{-22}
873	8.20×10^{-8}	4.42	10^{-1} - $10^{-7.5}$
873	5.69×10^{-7}	7.07	10^{-11} - 10^{-19}
973	1.89×10^{-6}	4.64	$10^{0.2}$ - 10^{-8}
973	7.37×10^{-6}	6.86	10^{-12} - $10^{-16.5}$
1113	1.96×10^{-5}	4.28	10^{2} - 10^{-5}
1113	1.35×10^{-4}	6.66	$10^{-7.5}$ - 10^{-14}

determined in Fig. 2.3 (Eq. (2.10)). The experimental data were well expressed by Eq. (2.9). The n values in Fig. 2.3 were compared with those predicted for the possible reactions in Table 2.1.

The measured n values were more close to 4 and 6 predicted for free and hopping electron in cases I-IV rather than 2, 3 and 5 predicted for no hopping electron in cases II-IV. The above comparison of n values for LDC at 773-1113 K leads to the following conclusions : (1) The charge neutrality condition is approximated by $2[V_O^{\bullet\bullet}] \approx [R'_{Ce}]$ at a lower applied voltage. (2) The electronic conduction at a lower applied voltage is related to the migration of free and hopping electrons in cases I-IV in Table 2.1. (3) The charge neutrality condition changes to $2[V_O^{\bullet\bullet}] \approx [e']$ or $2[V_O^{\bullet\bullet}] \approx [Ce'_{Ce}]$ at a higher applied voltage. (4) The electronic conductivity at a higher voltage has a high possibility to be associated with the migration of free and hopping electrons in cases I-IV in Table 2.1.

2.4.2. Comparison of Oxide Ion Conductivity and Electronic Conductivity

Figure 2.4 shows the comparison of oxide ion conductivity and electronic conductivity for LDC in a temperature range from 773 to 1113 K, as a function of oxygen partial pressure. The electronic conductivity-oxygen partial pressure relation was plotted by substituting the experimentally measured n and C_1 values in Eq. (2.10) into Eq. (2.1). The experimental constants C_1 and n values are shown in Table 2.2. On the other hand, we reported the electrical conductivity of LDC in air in a previous paper[4]. This value represents the oxide ion conductivity. The comparison of the data in Fig. 2.4 apparently indicates that the oxide ion conductivity of the samples is much higher than the electronic conductivity at a higher oxygen partial pressure. In Fig. 2.4, the electronic conduction of LDC ($Ce_{0.8}La_{0.2}O_{1.9}$), measured by Xiong et al.[8] in the oxygen partial pressure range from 10^{-3} to 10^5 Pa at 973 K, was also plotted. As seen in Fig. 2.4, the present data at a high oxygen partial pressure were very close to their values. The measured data were also compared with the previously measured electronic conductivity of the Gd- and Sm-doped ceria[3), 9)]. The relationship between applied voltage (E) and electronic current density (I), the relationship between ln σ_e (electronic conductivity) and E (applied voltage) and the comparison of oxide ion conductivity and

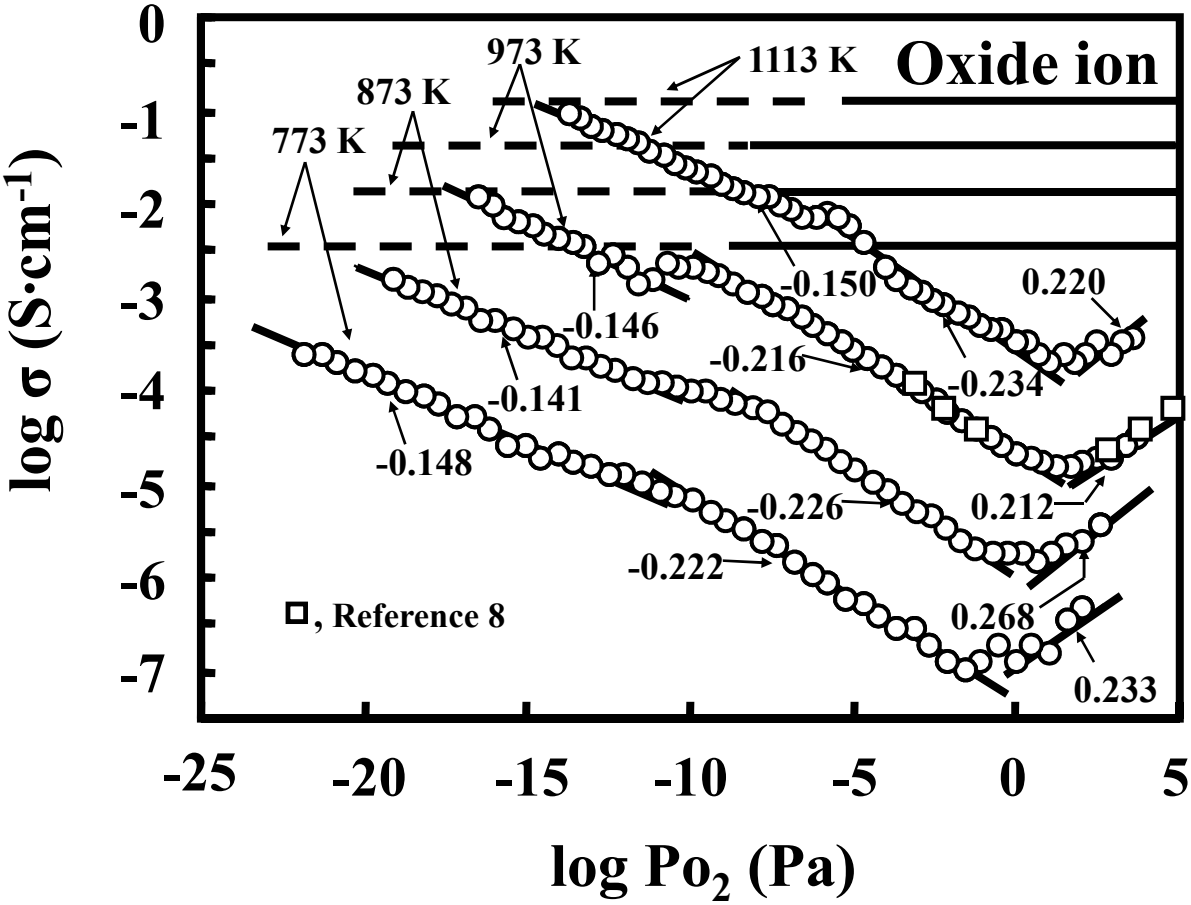

Fig. 2.4 Comparison of conductivities between oxide ion and electron for LDC under an oxygen partial pressure range from 10^{5} to 10^{-22} Pa at 773-1113 K.

electronic conductivity for SDC at 1073 K[9] are shown in Figs. 2.5, 2.6 and 2.7, respectively. The data measured for SDC at 1073 K have the trend similar to LDC studied in this chapter. The n value measured for SDC at 1073 K was 4.1 in the applied voltage range from 0.2 to 0.5 V and 7.1 in the applied voltage range from 0.6 to 1.0 V. Figures 2.8 and 2.9 show the relationships between ln I (electronic current) and E (applied voltage) for GDC[3] and SDC[3] at the steady state, respectively. Equation (2.9) is transformed into Eq. (2.26),

$$\ln I = \ln C_2 + \ln\left[\exp\left(\frac{4FE}{nRT}\right) - 1\right] \tag{2.26}$$

where C_2 is equal to $nAC_1RTPo_2(outer)^{-1/n}/4FL$ in Eq. (2.9). For the condition of exp (4FE / nRT) >> 1, Eq. (2.26) is approximated to Eq. (2.27),

$$\ln I = \ln C_2 + \frac{4FE}{nRT} \tag{2.27}$$

Equation (2.27) is useful to determine both the values of C_2 and n from the linear relationship between ln I and E. Both the samples showed a high linearity with 0.993-0.999 of the correlation coefficient in a wide applied voltage range of 0.2-1.4 V. This result supports the good approximation by Eq. (2.27) for the measured electronic conductivity. Tables 2.3 and 2.4 summarize the experimental constants C_1 and n values for GDC and SDC, respectively. The n value measured in GDC was close to 6 in the temperature range from 873 to 1113 K, except for the measurement at 773 K. On the other hand, the n value in SDC was higher than 6 and approached 6 as the heating temperature was increased to 1073 K. The reason for this tendency of n value is not explained by the interaction between SDC and electron discussed in Section 2.3.2. The experiment for GDC and SDC covers the electronic conduction in the Po_2 range from 10 to 10^{-32} Pa at 773-1113 K for GDC (Fig. 2.10) and from 10^2 to 10^{-22} Pa at 773-1073 K for SDC (Fig. 2.11). The reported electronic conductivities of LDC and GDC were comparable to the conductivity of the present LDC. However, the reported SDC showed a higher electronic conductivity than the present LDC.

On the other hand, the electronic conductivity of LDC increased in the oxygen partial pressure range higher than 10^2 Pa. This result is explained by hole conduction.

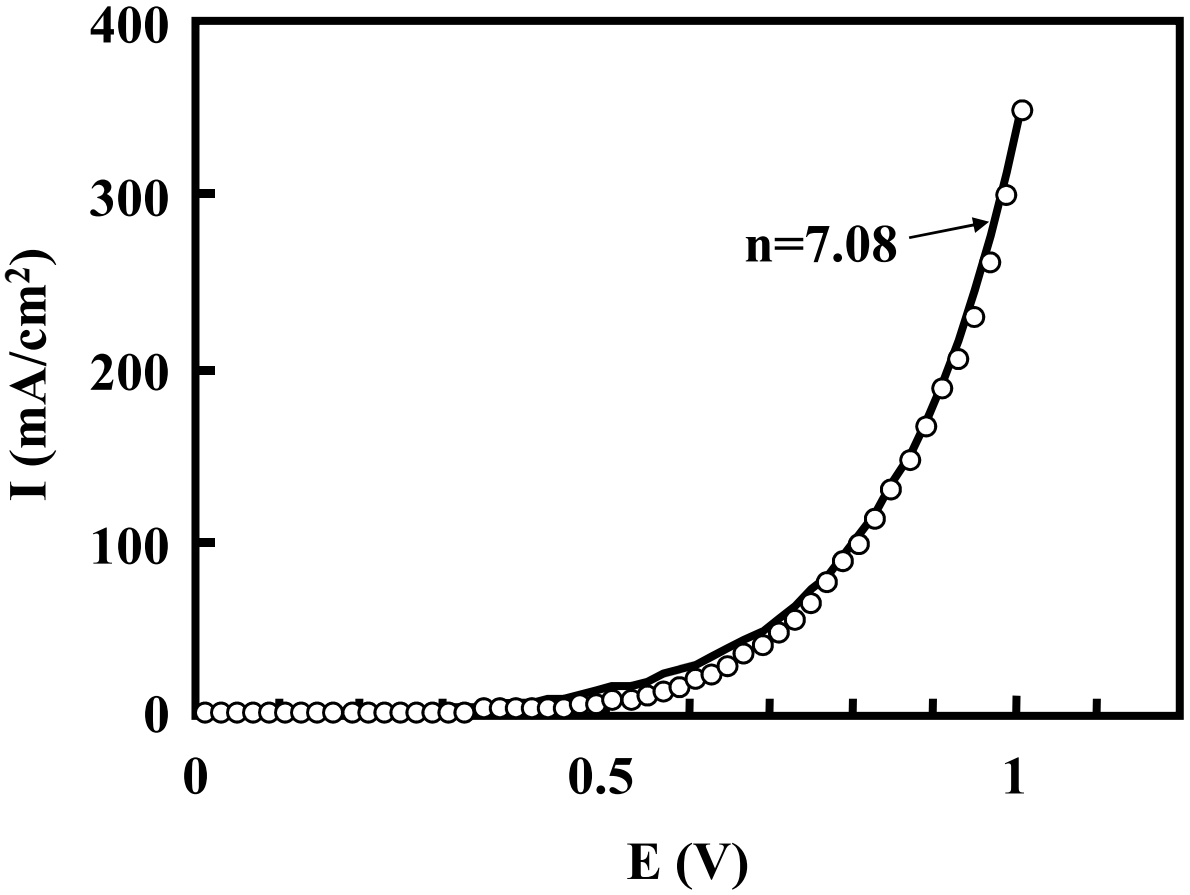

Fig. 2.5 Relationship between applied voltage (E) and electronic current density (I) for SDC at 1073 K.

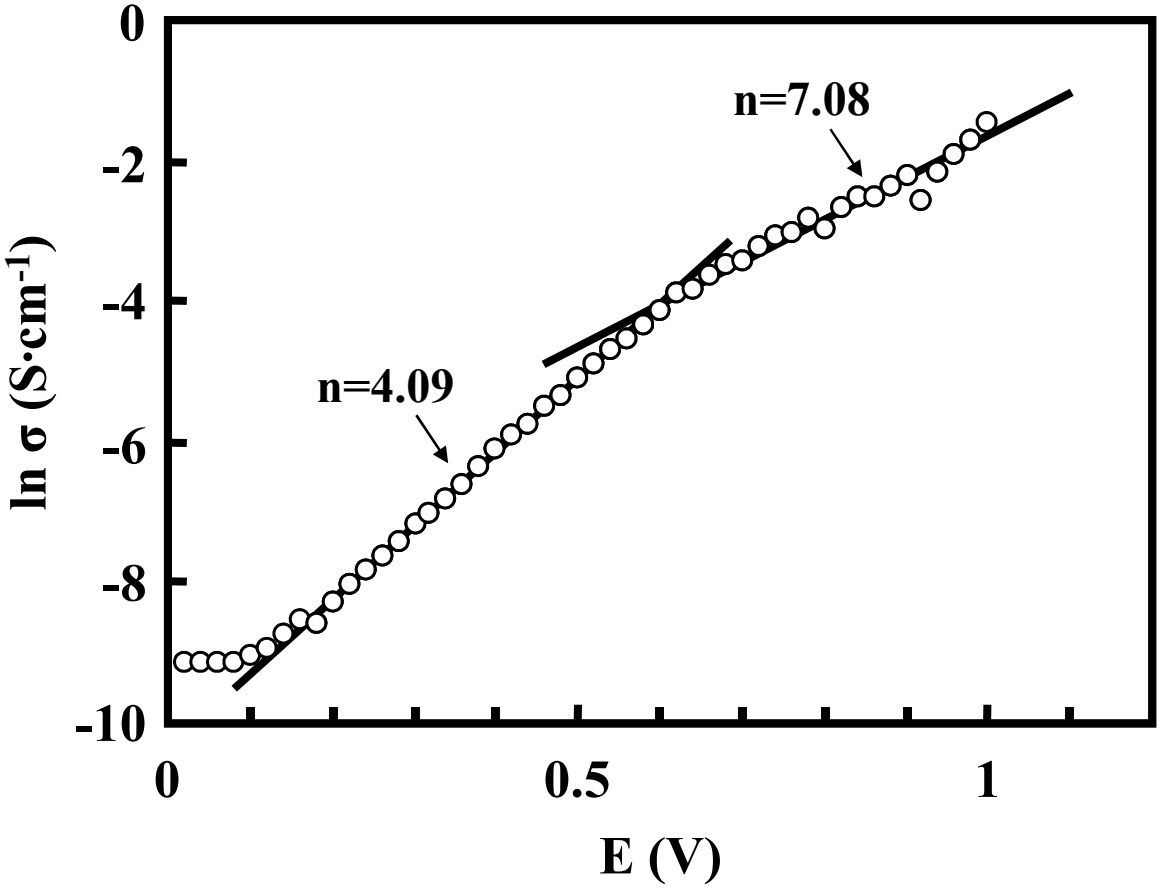

Fig. 2.6 Logarithmic electronic conductivity and applied voltage for SDC at 1073 K.

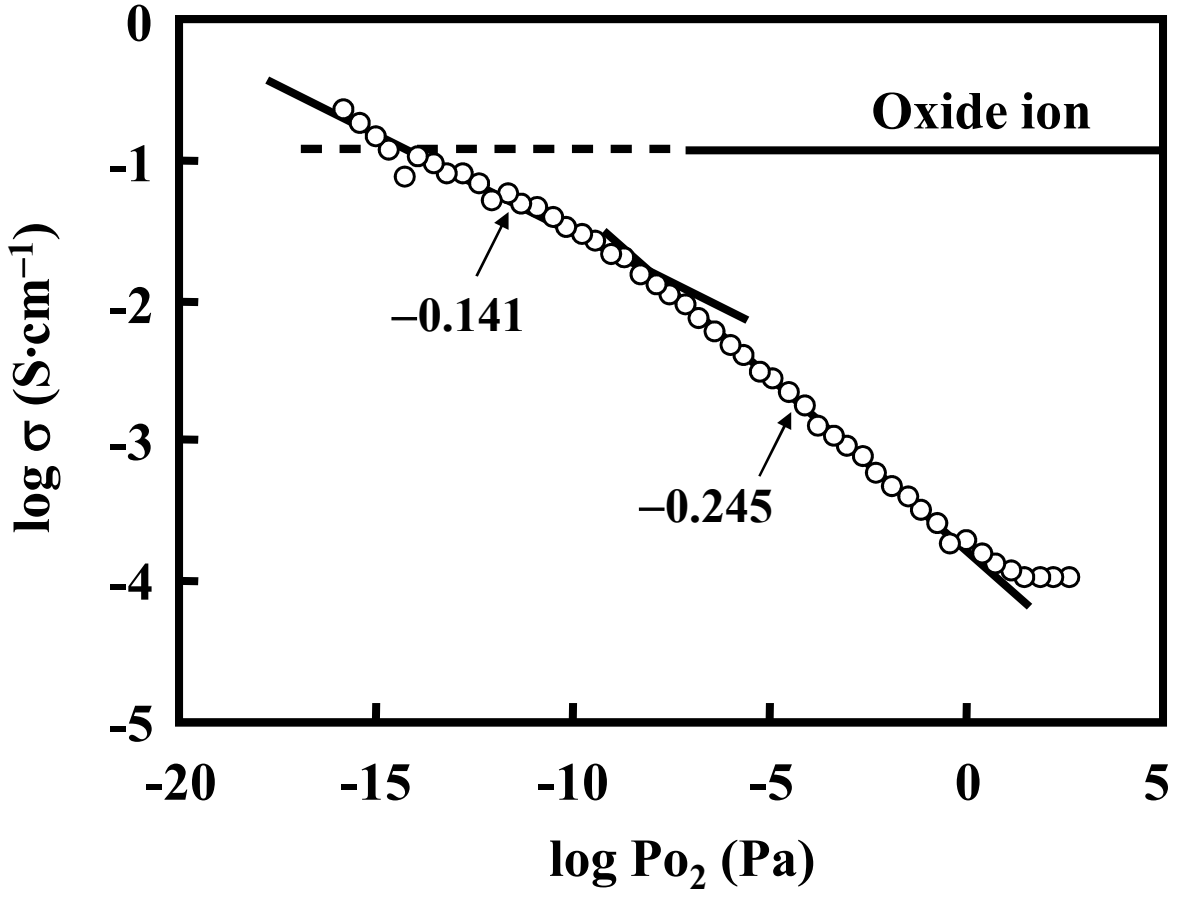

Fig. 2.7 Comparison of conductivity between oxide ion and electron for SDC at 1073 K under an oxygen partial pressure range from 10^{3} to 10^{-16} Pa.

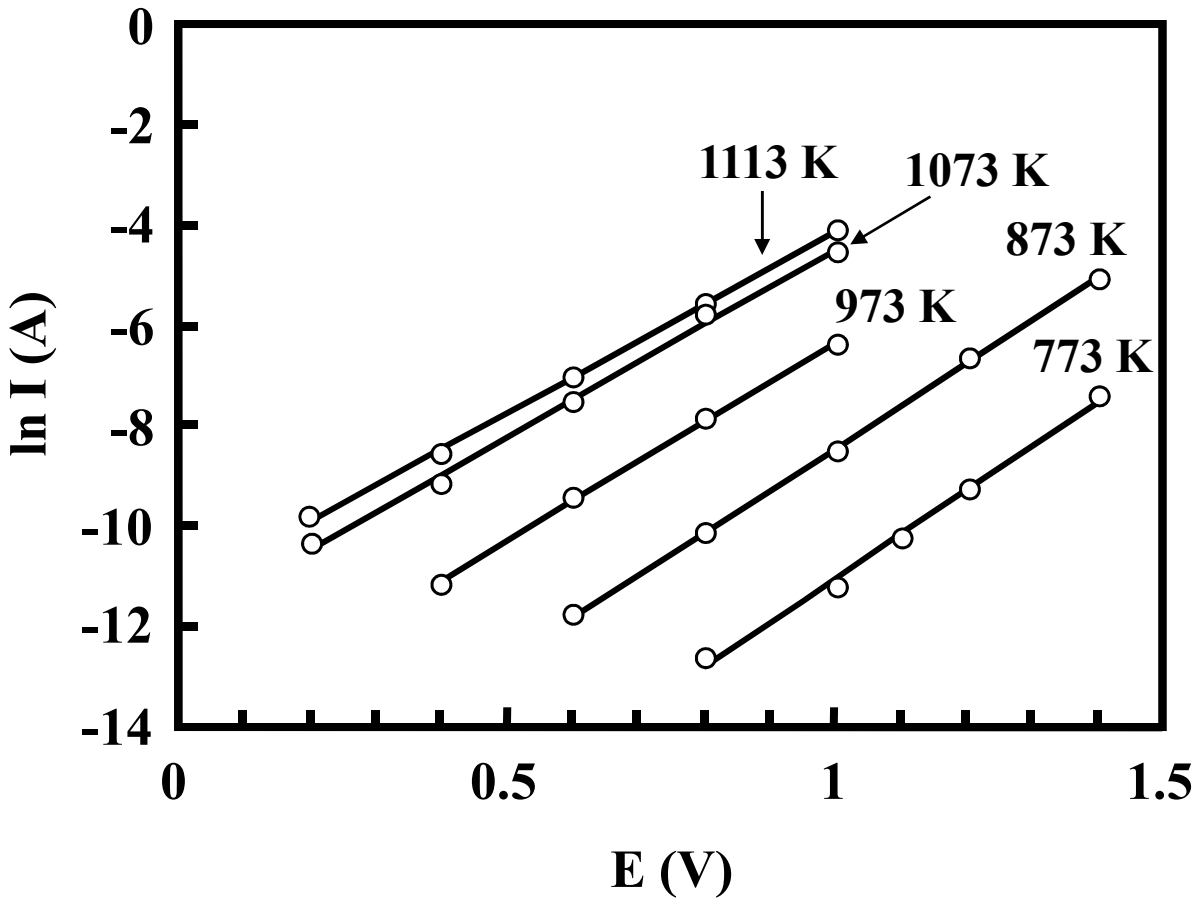

Fig. 2.8 Logarithmic electronic current and applied voltage for GDC at 773 – 1113 K.

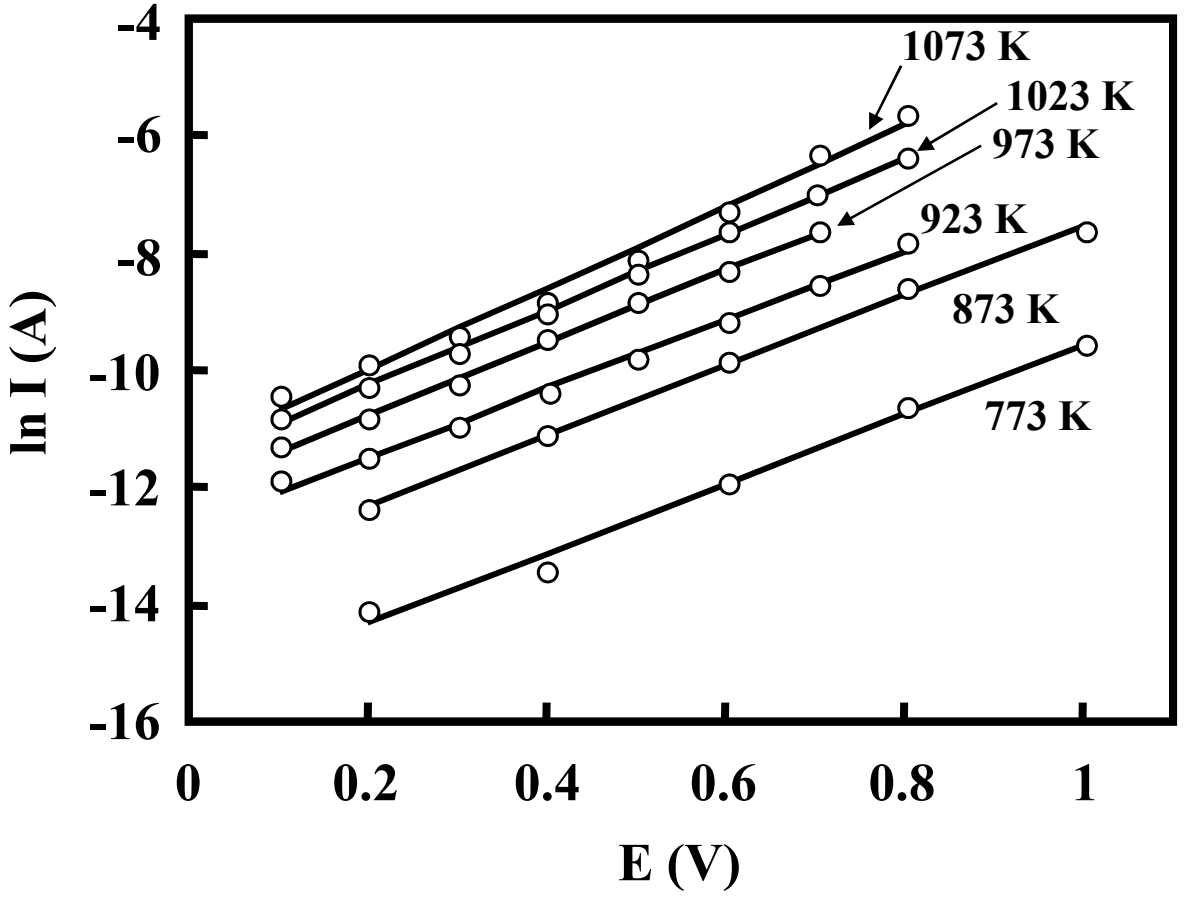

Fig. 2.9 Logarithmic electronic current and applied voltage for SDC at 773 – 1073 K.

Table 2.3 Experimental constants C_1 and n values in electronic conductivity, $\sigma_e = C_1 Po_2^{-1/n}$ for GDC.

Analysis	Temperature (K)	C_1 ($S \cdot cm^{-1}$)	n (–)	Oxygen partial pressure range (Pa)
Eq. (2.27)	773[3)]	1.27×10^{-8}	6.88	$10^{-16.6}$ - $10^{-32.3}$
	873[3)]	2.18×10^{-7}	6.30	$10^{-9.6}$ - $10^{-28.1}$
	973[3)]	2.75×10^{-6}	6.00	10^{-4} - $10^{-16.4}$
	1073[3)]	2.58×10^{-5}	5.79	$10^{0.6}$ - $10^{-14.5}$
	1113[3)]	4.63×10^{-5}	5.79	$10^{0.7}$ - $10^{-13.8}$

Table 2.4 Experimental constants C_1 and n values in electronic conductivity, $\sigma_e = C_1 Po_2^{-1/n}$ for SDC.

Analysis	Temperature (K)	C_1 ($S \cdot cm^{-1}$)	n (–)	Oxygen partial pressure range (Pa)
Eq. (2.27)	773[3)]	5.27×10^{-7}	10.11	$10^{-0.9}$ - $10^{-21.8}$
	873[3)]	3.82×10^{-6}	8.88	$10^{-0.3}$ - $10^{-18.8}$
	923[3)]	8.72×10^{-6}	8.57	$10^{2.1}$ - $10^{-13.2}$
	973[3)]	1.74×10^{-5}	7.70	$10^{2.2}$ - $10^{-10.2}$
	1023[3)]	2.81×10^{-5}	7.06	$10^{2.4}$ - $10^{-11.5}$
	1073[3)]	3.45×10^{-5}	6.21	$10^{2.4}$ - $10^{-10.8}$
Eq. (2.3)	1073[9)]	9.92×10^{-6}	4.09	$10^{-0.4}$ - $10^{-7.1}$
	1073[9)]	2.24×10^{-4}	7.08	$10^{-7.5}$ - $10^{-15.8}$

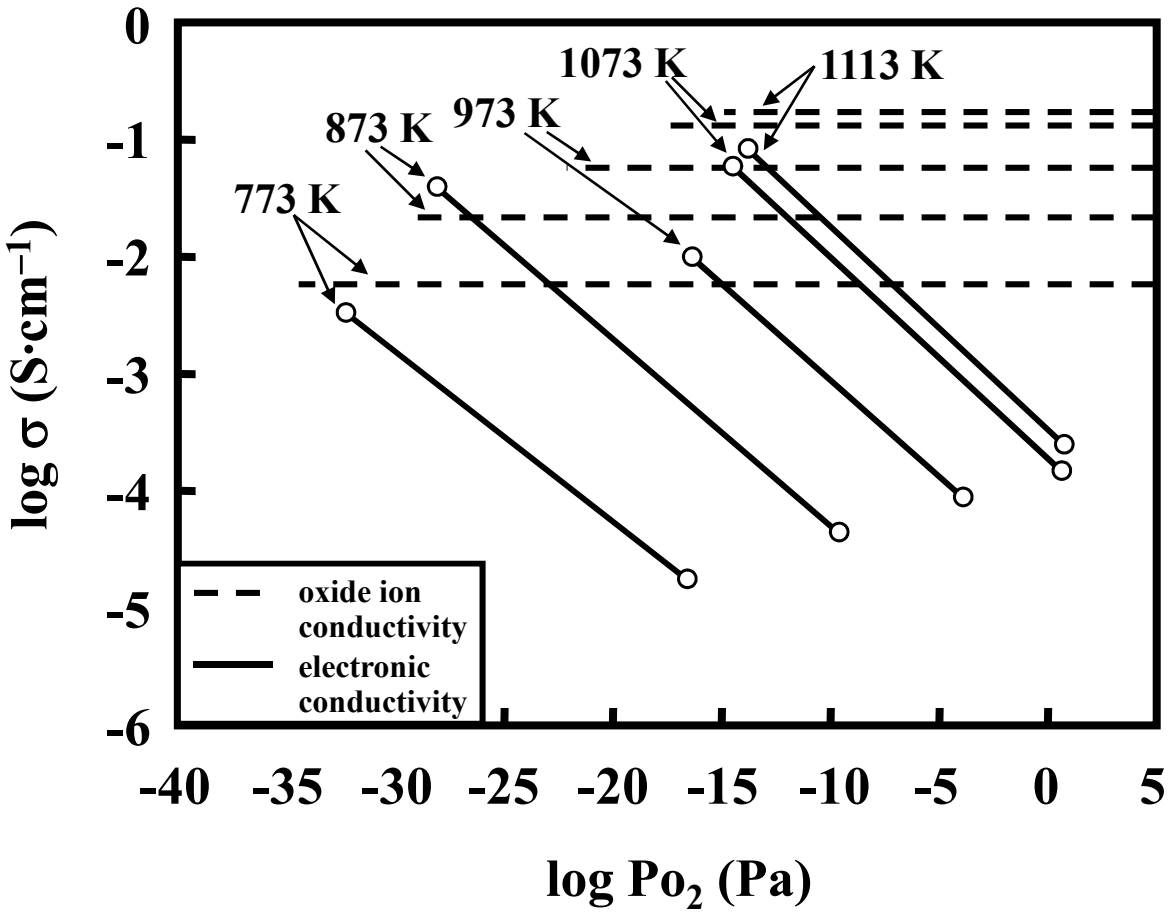

Fig. 2.10 Comparison of conductivity between oxide ion and electron for GDC under an oxygen partial pressure range from 10 to 10^{-32} Pa. The open circles for electronic conduction represents the Po_2 (inner) range in Eq. (2.2) at a given applied voltage range.

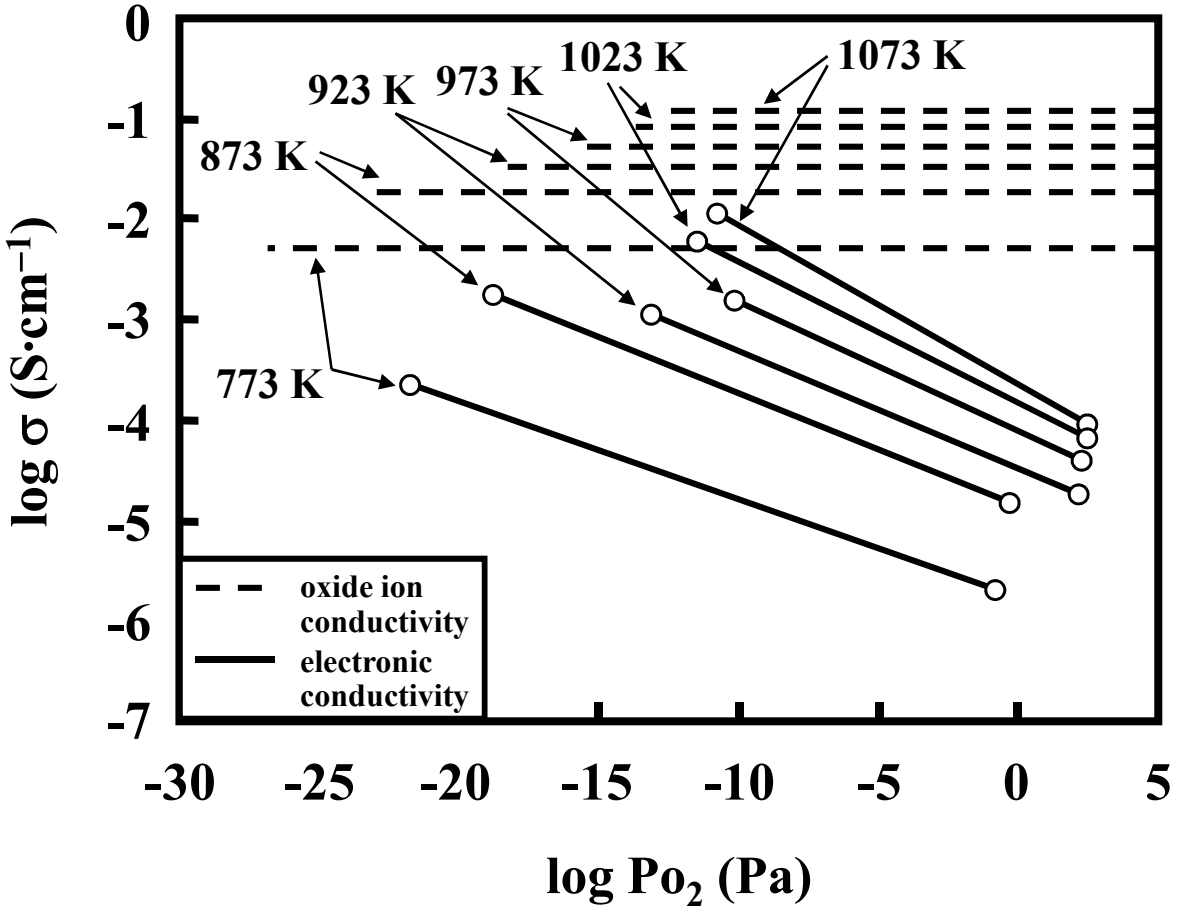

Fig. 2.11 Comparison of conductivity between oxide ion and electron for SDC under an oxygen partial pressure range from 10^2 to 10^{-22} Pa. The open circles for electronic conduction represents the Po_2 (inner) range in Eq. (2.2) at a given applied voltage range.

Equation (2.28) expresses the interaction between oxygen vacancy and oxygen gas to form positively charged holes.

$$V_O^{\bullet\bullet} + \frac{1}{2}O_2 \rightleftarrows O_O^{\times} + 2h^{\bullet} \tag{2.28}$$

The equilibrium constant K for Eq. (2.28) is expressed by Eq. (2.29).

$$K = \frac{[O_O^{\times}][h^{\bullet}]^2}{[V_O^{\bullet\bullet}]P_{O_2}^{1/2}} \tag{2.29}$$

The charge neutrality condition in consideration of Eq. (2.11) is expressed by Eq. (2.30),

$$2[V_O^{\bullet\bullet}] + [h^{\bullet}] = [R'_{Ce}] \tag{2.30}$$

Since the hole conductivity is significantly low, the charge neutrality condition is approximated to be $2[V_O^{\bullet\bullet}] \approx [R'_{Ce}]$. That is, $[h^{\bullet}]$ is represented by Eq. (2.31), giving a linear relation with 1/4 of slope in the log $[h^{\bullet}]$ - log Po_2 plot.

$$[h^{\bullet}] = \left(\frac{K}{2}\right)^{1/2}\left(\frac{[R'_{Ce}]}{[O_O^{\times}]}\right)^{1/2} P_{O_2}^{1/4} \tag{2.31}$$

The measured slopes for LDC in the Po_2 range higher than 10^2 Pa were 0.212-0.268. This result was close to the theoretical value (0.25) predicted by Eq. (2.31). That is, LDC shows hole conduction in the Po_2 range from 10^2 to 10^5 Pa but the hole conductivity is significantly lower than the oxide ion conductivity. The oxygen partial pressure in which the hole conductivity became equal to the electronic conductivity was 0.2, 0.5, 1.7 and 1.5 Pa at 773, 873, 973 and 1113 K, respectively.

Figure 2.12 shows the Arrhenius plot of the electronic conductivity. The apparent activation energy of the electronic conduction was 1.93, 1.94 and 1.87 eV at $Po_2 = 10^{-2}$, 10^{-4} and 10^{-14} Pa, respectively. Although the oxygen partial pressure dependence of electronic conduction was different at the low and high oxygen pressure ranges (Fig. 2.4), the activation energy was similar to each other. The reported activation energy for electronic conduction was 2.07 eV for $Ce_{0.8}Y_{0.2}O_{1.9}$[10] and 2.00 eV for $Ce_{0.8}Gd_{0.2}O_{1.9}$[11], and was very close to the present data.

The measured conductivities of oxide ion, electron and hole were coupled to clarify the transference number of oxide ion. Figure 2.13 shows the transference number

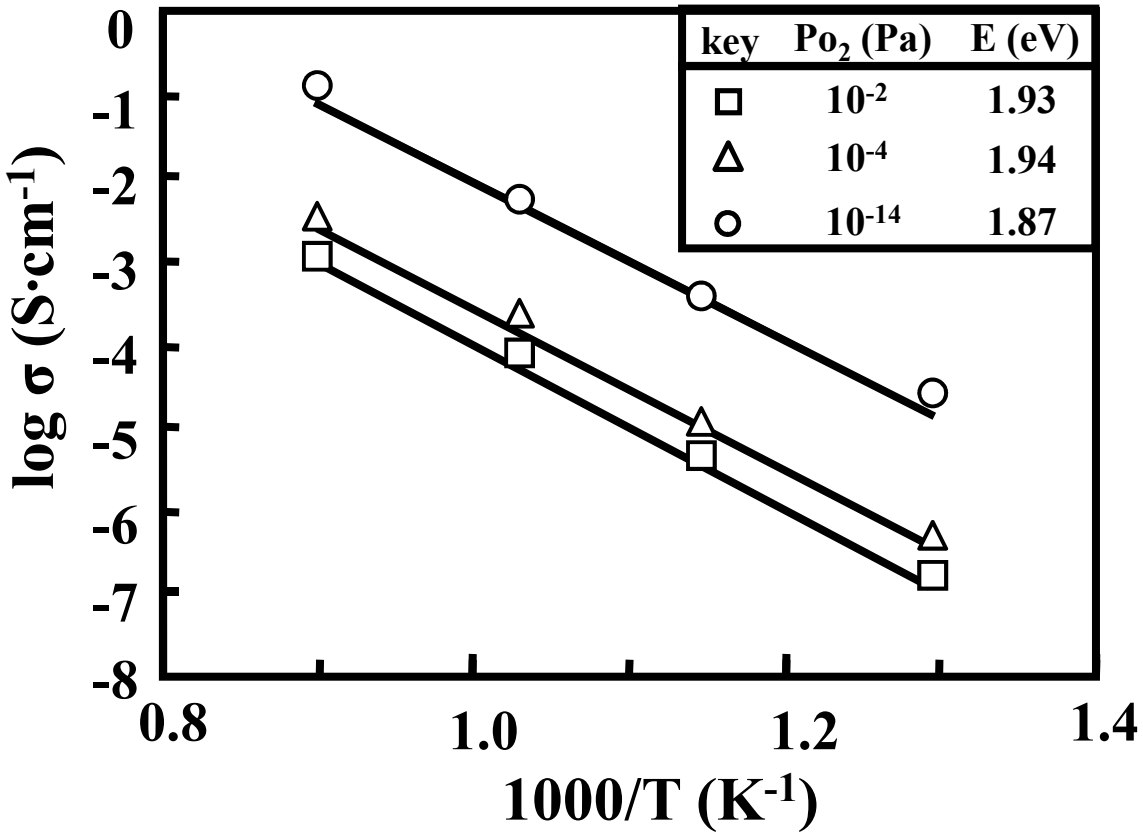

Fig. 2.12 Temperature dependence of the electronic conductivity of LDC at the different oxygen partial pressures.

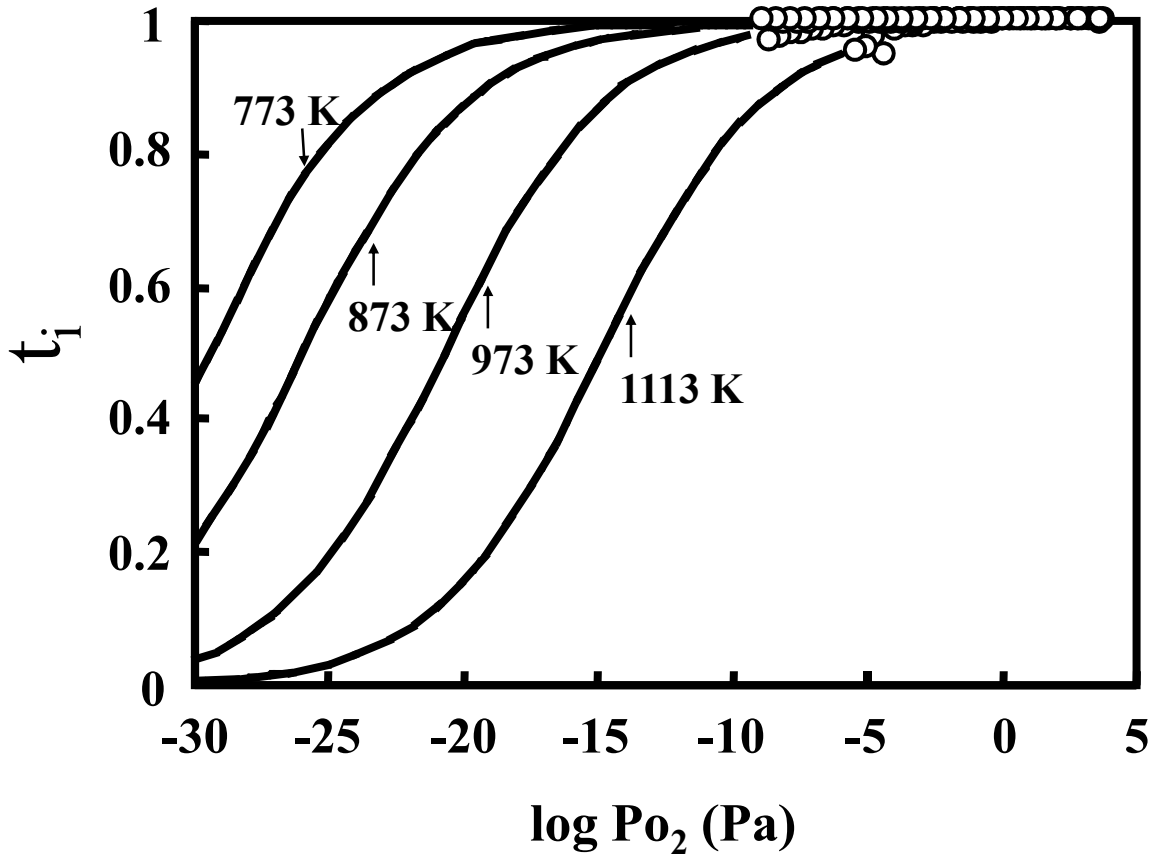

Fig. 2.13 Transport number (t_i) of oxide ion for LDC as a function of oxygen partial pressure at 773-1113 K. The solid lines were extrapolated by Eq. (2.1) from the measured electronic conductivity and oxide ion conductivity measured in air under the assumption that the oxide ion conductivity was independent of oxygen partial pressure.

(t_i) of oxide ion for LDC in a temperature range from 773 to 1113 K, as a function of oxygen partial pressure. The solid lines were extrapolated from the measured oxide ion conductivity and electronic conductivity (Eq. (2.1)) under the assumption that the oxide ion conductivity is independent of oxygen partial pressure. The results for LDC indicate that the t_i value increases with decreasing temperature and increasing oxygen partial pressure. Compared with the previously measured transference number of oxide ion, which were presented in the introduction section, the significantly high t_i values were measured in the present sample. This result is favorable to the use of RDC in the solid electrolyte of SOFC.

2.5 Summary

The electronic conductivity of LDC was measured in a temperature range from 773 to 1113 K by direct current polarization method using the Hebb-Wagner ion blocking cell. A high linearity between ln σ_e (electronic conductivity)-E (applied voltage), which was theoretically predicted, was measured for LDC in the applied voltage of 0.2-1.0 V. The electronic conduction of LDC was proportional to $Po_2^{-1/4.3} \sim Po_2^{-1/4.6}$ in the higher Po_2 range (10^{-2}-10^{-8} Pa) and $Po_2^{-1/6.7} \sim Po_2^{-1/7.1}$ in the lower Po_2 range ($10^{-7.5}$-10^{-22} Pa). The activation energy for electronic conduction at $Po_2 = 10^{-2}$-10^{-14} Pa was 1.87-1.94 eV. In the Po_2 range from 10^2 to 10^5 Pa, hole conduction with the slopes of 0.21-0.27 in the log σ_e-log Po_2 plot was measured. The transference number (t_i) of oxide ion for the present LDC was significantly higher than the previously reported values. The t_i value for LDC at 773-1113 K was 0.96-1.00 under an oxygen partial pressure of 10^{-5} Pa. These results were compared with the previously reported data of Sm-doped ceria and Gd-doped ceria. The data measured for SDC at 1073 K have the trend similar to LDC studied in this chapter. The slope of log σ_e–log Po_2 plot for SDC at 1073 K was −1/4.1 in the Po_2 range from 10 to 10^{-7} Pa and decreased to −1/7.1 in the Po_2 range from 10^{-8} to 10^{-16} Pa. The slope of log σ_e–log Po_2 plot was also determined from the linear relationship between ln I (electronic current)–E (applied voltage). The slope for GDC was −1/6 in the temperature range from 873 to 1113 K, while the slope for SDC was in the range from −1/10.1 to −1/6.2 and increased with increasing temperature in the

temperature range from 773 to 1073 K. The reported electronic conductivity of GDC was comparable to the conductivity of the present LDC. However, the reported SDC showed a higher electronic conductivity than the present LDC.

References

1) H. Yahiro, K. Eguchi and H. Arai, Solid State Ionics, 36 [10], 71-75 (1989).

2) B. C. H. Steele, K. Zheg, R. A. Rudkin, N. Kiratzis and M. Chrisitie, Proceedings of the Fourth International Symposium on Solid Oxide Fuel Cells (SOFC-IV), June 1995, Edited by M. Dokiya, O. Yamanoto, H. Tagawa and S. C. Singhal, The Electrochem. Soc., Inc., New Jersey (1995) pp.1028-1038.

3) T. Shimonosono, Y. Hirata, Y. Ehira, S. Sameshima and T. Horita, J. Ceram. Soc. Japan, Suppl., 112 [5], S616-S621 (2004).

4) S. Sameshima, H. Ono, K. Higashi, K. Sonoda, Y. Hirata and Y. Ikuma, J. Ceram. Soc. Japan, 108 [12], 1060-1066 (2000).

5) K. Higashi, K. Sonoda, H. Ono, S. Sameshima and Y. Hirata, Key Eng. Mater., 159-160, 25-30 (1999).

6) K. Higashi, K. Sonoda, H. Ono, S. Sameshima and Y. Hirata, J. Mater. Res., 14 [3], 957-967 (1999).

7) Y. Xiong, K. Yamaji, N. Sakai, H. Negishi, T. Horita and H. Yokokawa, J. Electrochem. Soc., 148 [12], E489-E492 (2001).

8) Y. Xiong, K. Yamaji, T. Horita, N. Sakai and H. Yokokawa, J. Electrochem. Soc., 151 [3], A407-A412 (2004).

9) T. Shimonosono, Y. Hirata, Y. Ehira, S. Sameshima, T. Horita and H. Yokokawa, Solid State Ionics, 174 [10], 27-33 (2004).

10) T.Otake, H. Yugami, K. Yashiro, Y. Nigara, T. Kawada and J. Mizusaki, Solid State Ionics, 161 [7], 181-186 (2003).

11) S. Wang, H. Inaba, H. Tagawa, M. Dokiya and T. Hashimoto, Solid State Ionics, 107 [3], 73-79 (1998).

Chapter 3

Electrochemical Properties of Cathode of Solid Oxide Fuel Cell with Gd-Doped Ceria Electrolyte

3.1 Introduction

Rare earth-doped ceria (RDC) is the candidate of the electrolyte for the low temperature SOFC. As shown in chapter 2, the transference number of oxide ion in RDC reaches unity with decreasing temperature. On the other hand, the electric power density is also affected by the properties of electrodes. As described in chapter 1, it is reported that the polarization loss of electric power for the O_2 reduction ($O_2 + 4e^- \rightarrow 2O^{2-}$) on the cathode is particularly large because of the relatively high activation energy and relatively slow reaction rate as compared with the case of H_2 oxidation on the anode. The reduction of oxygen molecules at the cathode includes the diffusion of O_2 gas, the dissociative adsorption of O_2 on the cathode surface, the surface diffusion of O atom to the triple phase boundary of the electrolyte - cathode - O_2 gas and the diffusion of oxide ion into the electrolyte as shown in Fig. 3.1. Figure 3.1 also shows the enthalpy change of some process in the reduction of oxygen molecules. The dissociation of oxygen molecule and the reaction of an oxygen atom with two electrons are the endothermic reactions with the enthalpy changes of 494 kJ/mol-O_2 and 702 kJ/mol-O, respectively. The novel materials and microstructures for cathode have been developed to enhance the cathode performance. It was reported that $La_{2-x}Sr_xNiO_{4+\delta}$ of K_2NiF_4-type structure is a candidate cathode for SOFC in terms of the higher oxygen diffusion coefficient than $La_{0.6}Sr_{0.4}Co_{0.2}Fe_{0.8}O_3$ which is one of the candidate cathode, and the thermal expansion coefficient of $La_{2-x}Sr_xNiO_{4+\delta}$ is close to that of YSZ or GDC[1)]. Shao et al. studied perovskite-type oxide $Ba_{0.5}Sr_{0.5}Co_{0.8}Fe_{0.2}O_{3-\delta}$ (BSCF) of ionic-electronic mixed conductor as a cathode material for low temperature SOFC, and reported that the maximum power densities of the cell with BSCF cathode on the Sm-doped ceria electrolyte thin film were 402 and 1010 mW/cm^2 at 773 and 873 K, respectively[2)]. Liu et al. fabricated the composite cathode of Sr-doped lanthanum manganite (LSM) – Sr-doped lanthanum cobaltite (LSC) – Gd-doped ceria (GDC) on YSZ electrolyte. The

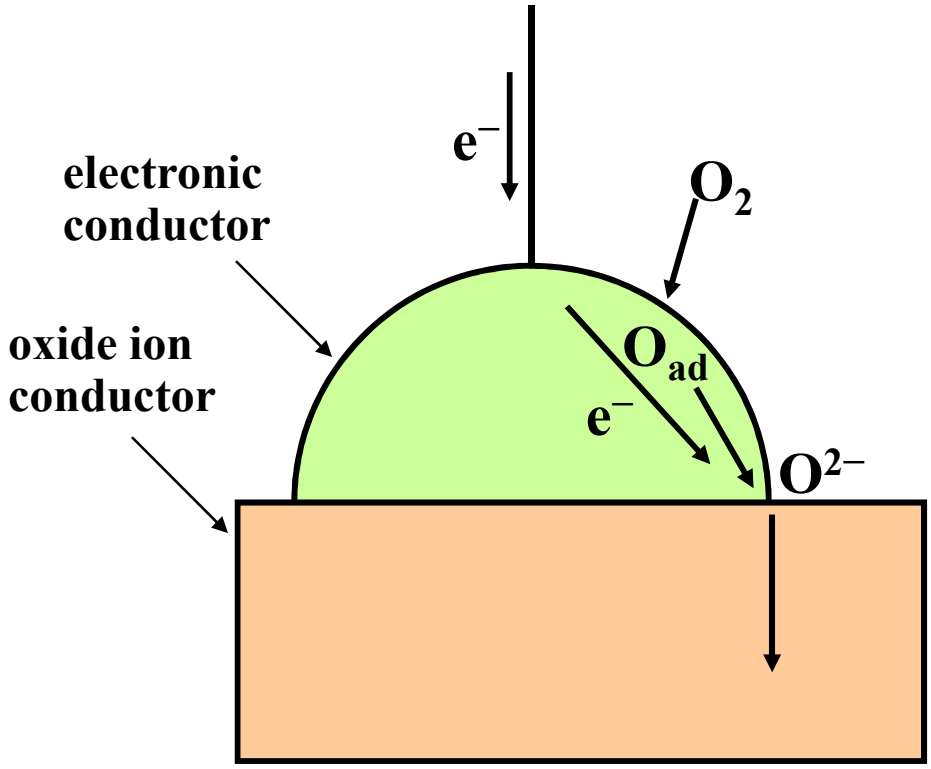

$$O_2 \rightarrow 2O \quad \Delta H = 494\ \text{kJ/mol-}O_2$$

$$O + 2e^- \rightarrow O^{2-} \quad \Delta H = 702\ \text{kJ/mol-}O$$

Fig. 3.1 Reduction of oxygen molecules at the cathode.

composite was graded in both composition and structure. A higher LSM content and finer primary grain size were designed at electrolyte side while higher LSC content and coarser primary grain size at air/oxygen side were set in order to optimize the chemical compatibility with YSZ electrolyte, triple phase boundary for oxygen reduction, pass of current and transport of oxygen molecules to the active reaction sites[3].

However, high performance cathode materials for RDC electrolyte have not been established. Addition of RuO_2 with the high electrical conductivity to Sr-doped samarium cobaltite ($Sm_{0.5}Sr_{0.5}CoO_3$, SSC) cathode reduced the ohmic resistance and overpotential at the cathode, and increased the power density of the SOFC with Sm-doped ceria electrolyte[4]. Oxygen molecules adsorbed on the triple phase boundaries of SSC-RuO_2-O_2 gas, easily react with the electrons supplied from RuO_2 and the formed oxide ions diffuse along the grain boundaries between SSC and RuO_2[4]. Reference 4 also showed the formations of $SrRuO_3$ and Co_2RuO_4 due to the reaction between SSC and RuO_2[4]. On the other hand, the maximum coverage of oxygen on palladium, platinum, rhodium, iridium, ruthenium and gold electrodes in the sulfuric acid solution saturated with oxygen at room temperature were repored[5]. The maximum coverage of oxygen was proportional to the number of unpaired d-electrons per atom, and was the largest for the ruthenium electrode[5]. The ruthenium elements in the compound may be also active sites for the dissociative adsorption of oxygen molecules, which may lead to the decrease of the activation energy for oxygen reduction on the cathode. The electrical conductivities of $SrRuO_3$[6] and Co_2RuO_4[7] have been reported to be 1×10^4 and 1.4×10^{-1} S/cm at room temperature, respectively. However, these materials have not been investigated as a cathode for RDC electrolyte. The cathode materials reported in the literatures are the electronic conductor, ionic-electronic mixed conductor and composite of ionic and electronic conductors as described above. The cathode performance of electronic conductor is easily enhanced by the combination with an ionic conductor. Furthermore, the degradation of the cathode performance due to the grain growth worried about the single phase cathode like an ionic-electronic mixed conductor is suppressed for a composite cathode of ionic and electronic conductors. Then, it is favorable that an electronic conductor is explored to activate the oxygen reduction

reaction. In this chapter, $SrRuO_3$ and Co_2RuO_4 were investigated as the novel cathode for RDC electrolyte. In addition, indium tin oxide (ITO, 90 mass% In_2O_3-10 mass% SnO_2) with the high electrical conductivity[8] (5.0×10^2 S/cm at room temperature) was also studied. The electrochemical properties of these cathodes were measured for SOFC with Gd-doped ceria ($Ce_{0.8}Gd_{0.2}O_{1.9}$, GDC) electrolyte and Ni-GDC anode and were compared with those of $La_{0.6}Sr_{0.4}Co_{0.2}Fe_{0.8}O_3$ (LSCF) cathode.

3.2 Experimental Procedure

3.2.1 Powder Preparation of SOFC Component

The GDC powder was prepared by heating the oxalate solid solution at 873 K. The GDC powder was milled with alumina ball for 24 h and then pressed isostatically at 294 MPa to a pellet of 22 mm diameter and 2 mm thickness. The green compact was sintered at 1773 K for 4 h in air (SPM 6512 electric furnace, Marusho Electro-Heat Co., Ltd., Japan). The milled GDC powder was immersed into a 1.4 M $Ni(NO_3)_2$ solution to make a cermet anode with the volume ratio of Ni / GDC = 30 / 70. The suspension was freeze-dried and calcined at 873 K for 1 h in air. A high purity ITO powder (90 mass% In_2O_3-10 mass% SnO_2) with specific surface area 3.54 m^2/g, was supplied by Sumitomo Chemical Co., Japan. $La_{0.6}Sr_{0.4}Co_{0.2}Fe_{0.8}O_3$ (LSCF) was prepared by heating the freeze-dried mixture of coprecipitate of $La(NO_3)_3$, $Sr(NO_3)_2$, $Co(NO_3)_2$ and $Fe(NO_3)_3$ with $(NH_4)_2CO_3$. The freeze-dried powder was calcined at 1273 K for 1 h in air and the produced solid solution was identified by X-ray diffraction (RINT2200, Rigaku Denki Co. Ltd., Japan). The 0.2 M mixed solution of $RuCl_3$ and $Sr(NO_3)_2$ with the molar ratio of Ru / Sr = 1 / 1 was added into 1 M NH_4OH solution and then freeze-dried. The freeze-dried powder was heated at 1273 K for 2 h in air and formation of $SrRuO_3$ was confirmed by X-ray diffraction. Similarly, 0.2 M aqueous solutions of $RuCl_3$ and $Co(NO_3)_2$ were mixed in the stoichiometric ratio to prepare Co_2RuO_4 powder. The mixed solution was added into 1 M NH_4OH solution and then freeze-dried, which was followed by heating at 1373 K for 1 h in air. The crystal structure of the prepared powder was observed by X-ray diffraction.

3.2.2 Measurement of Cell Performance

The ITO, LSCF, $SrRuO_3$, Co_2RuO_4 and NiO-GDC powders were dispersed at 15 vol% solid in the mixed solution of 90 vol% ethanol – 10 vol% ethyleneglycol. The prepared suspension was formed with screen (mesh: 250 μm) of thread diameter of 4 mm on the surfaces of GDC electrolyte (> 95 % theoretical density) of 15 mm diameter and 550-700 μm thickness. The printed ITO, LSCF, $SrRuO_3$, Co_2RuO_4 and NiO-GDC powders were heated at 1423, 1273, 1273, 1273 and 1473 K for 1 h in air, respectively. The Pt wire reference electrodes were fixed on both the GDC surfaces with Pt paste at 1273 K. A Pt mesh was attached to the each electrode with Pt paste. The GDC electrolyte with the cathode and anode was set to an alumina holder and sealed at 1173 K by using a glass O-ring. After cooling to 1073 and 873 K, the cell performance was measured by feeding air and 3 vol% H_2O-containing H_2 fuel into cathode and anode at 100 ml/min, respectively. The NiO at the anode is reduced to Ni by the reaction with H_2 fuel ($NiO + H_2 \rightarrow Ni + H_2O$). Figure 3.2 shows the schematic diagram of the cell. A direct current-voltage relation and AC impedance in the frequency range from 0.01 Hz to 100 kHz at the current of 10 mA were measured at 873 and 1073 K (As-510, NF Kairosekkei Block Co., Japan). The current was flowed between the cathode and anode for all the measurement. On the other hand, the terminal voltages between the cathode and anode, the cathode and reference electrode of cathode side, the anode and reference electrode of anode side, and the reference electrodes of cathode side and anode side were measured to separate the voltage drop. The oxygen partial pressure of the fuel was monitored with yttria-stabilized zirconia oxygen gas sensor as shown in Fig. 3.3. Figure 3.3 shows the system for the measurement of electrochemical properties. The microstructure of the cell after the measurement of cell performance was observed using a scanning electron microscope (SM-300, Topcon, Co., Japan).

3.2.3 Chemical Reaction between GDC Powder and $SrRuO_3$ or Co_2RuO_4 Powder

The GDC powder and $SrRuO_3$ or Co_2RuO_4 powder were mixed at the volume ratio of GDC / $SrRuO_3$ or Co_2RuO_4 = 1 / 1. The mixed powders were heated at 1073 K for 10 h in air. The crystal structures of the mixed powders before and after the heating were observed by X-ray diffraction.

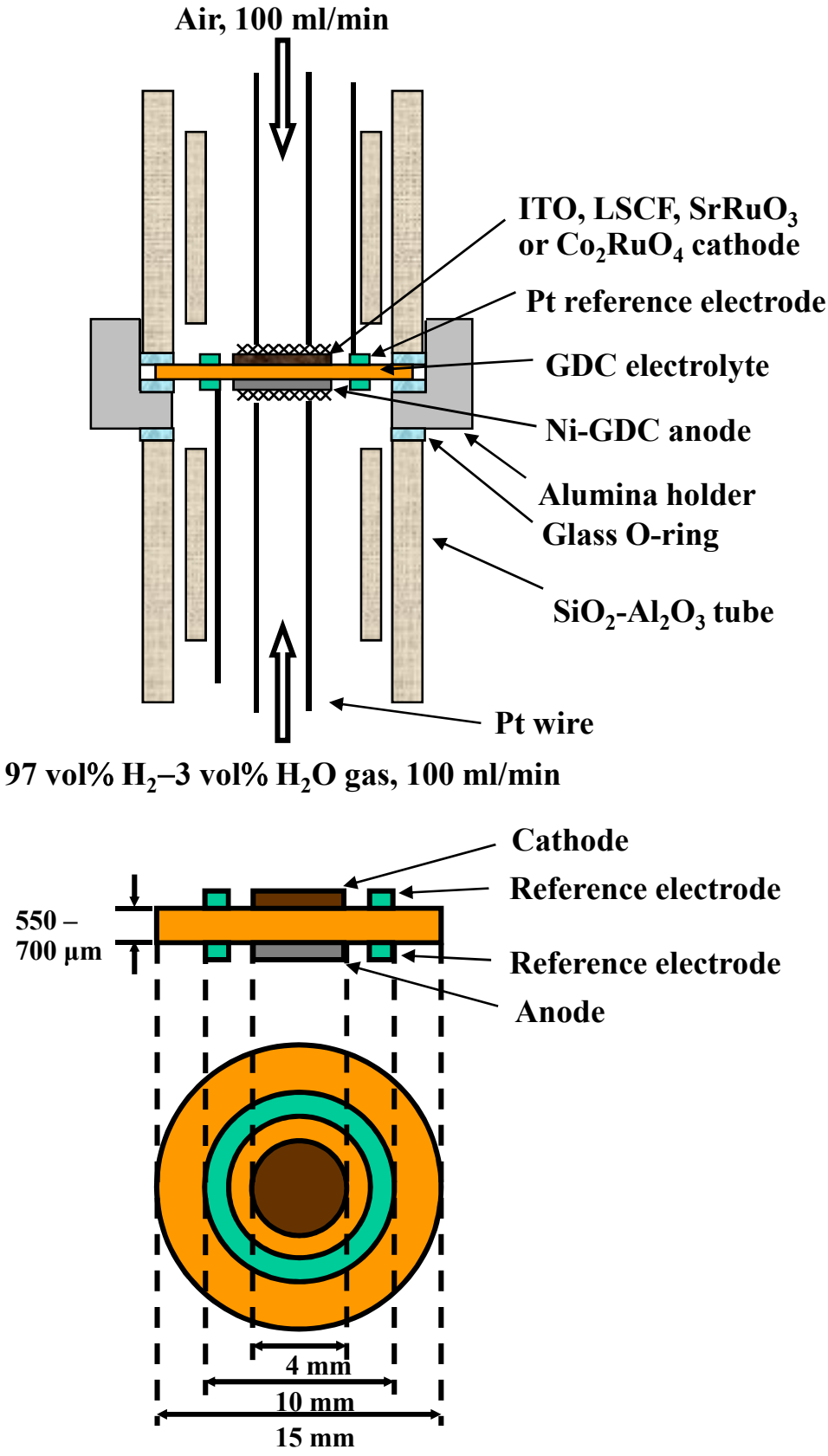

Fig. 3.2 Schematic diagram of the cell.

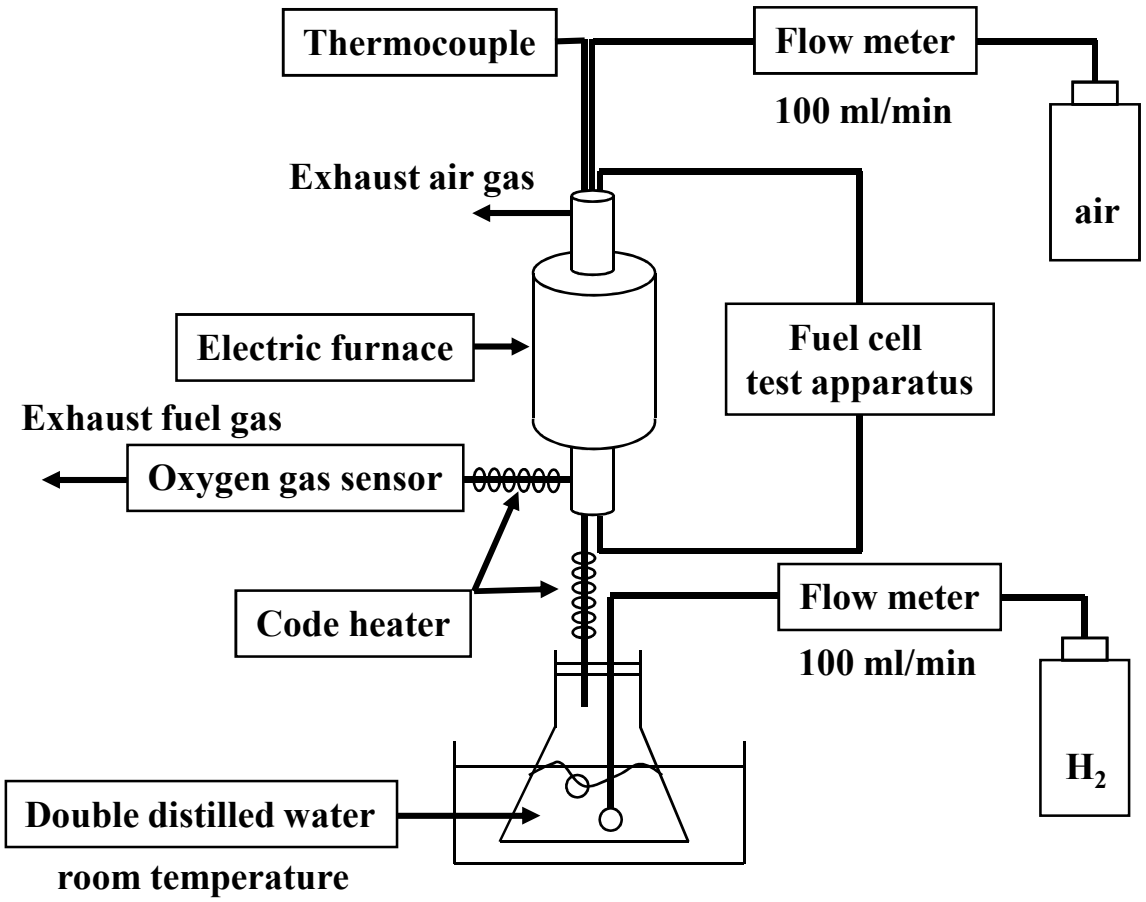

Fig. 3.3 System for the measurement of electrochemical properties.

3.3 Results and Discussion

3.3.1 Microstructures of ITO, $SrRuO_3$, Co_2RuO_4 / $Ce_{0.8}Gd_{0.2}O_{1.9}$ / Ni-$Ce_{0.8}Gd_{0.2}O_{1.9}$ Cell

Figures 3.4 (a), (b), (c) and (d) show the cross section of ITO, $SrRuO_3$, Co_2RuO_4 cathode and Ni-GDC anode after the measurement of cell performance, respectively. The porous ITO (90 μm thick) and Ni-GDC (40 μm thick) electrodes were formed on the dense GDC (650 μm thick). The similar microstructures were observed for the $SrRuO_3$ (100 μm) / GDC (620 μm) / Ni-GDC (85 μm) cell, Co_2RuO_4 (90 μm) / GDC (560 μm) / Ni-GDC (50 μm) and the LSCF (100 μm) / GDC (700 μm) / Ni-GDC (150 μm) cell. The particle sizes of ITO, $SrRuO_3$ and Co_2RuO_4 cathode were about 0.5, 20 and 1 μm, respectively. The $SrRuO_3$ cathode had the smallest surface area and triple phase boundary among the investigated cathode. The triple phase boundary of the electrolyte - cathode - O_2 gas is the site for the reaction between the oxygen molecules and electrons.

3.3.2 Terminal Voltage and Power Density

Figure 3.5 shows the terminal voltage and electric power density for the cells of ITO / GDC / Ni-GDC (cell 1), $SrRuO_3$ / GDC / Ni-GDC (cell 2) and Co_2RuO_4 / GDC / Ni-GDC (cell 3). Figure 3.5 shows also the terminal voltage and electric power density for the cell of LSCF / GDC / Ni-GDC (cell 4), which were studied by Hiramatsu et al.[9]. The open circuit voltages (V_{OCV}) at 873 K for cell 1, 2, 3 and 4 were 0.93, 0.85, 0.84 and 0.81 V, respectively. The V_{OCV} values at 1073 K for cell 1, 2, 3 and 4 were 0.82, 0.82, 0.57 and 0.79 V, respectively. The maximum power density and the corresponding current density for cell 1 were 21 mW/cm^2 and 43 mA/cm^2 at 873 K, and 71 mW/cm^2 and 205 mA/cm^2 at 1073 K. For cell 2 with $SrRuO_3$ cathode, the maximum power density and the corresponding current density were 36 mW/cm^2 and 90 mA/cm^2 at 873 K, and 328 mW/cm^2 and 718 mA/cm^2 at 1073 K. For cell 3 with Co_2RuO_4 cathode, the maximum power density and the corresponding current density were 38 mW/cm^2 and 91 mA/cm^2 at 873 K, and 183 mW/cm^2 and 599 mA/cm^2 at 1073 K. When LSCF cathode was used in cell 4, the maximum power density and the corresponding current density were 12 mW/cm^2 and 32 mA/cm^2 at 873 K, and 113 mW/cm^2 and 279 mA/cm^2

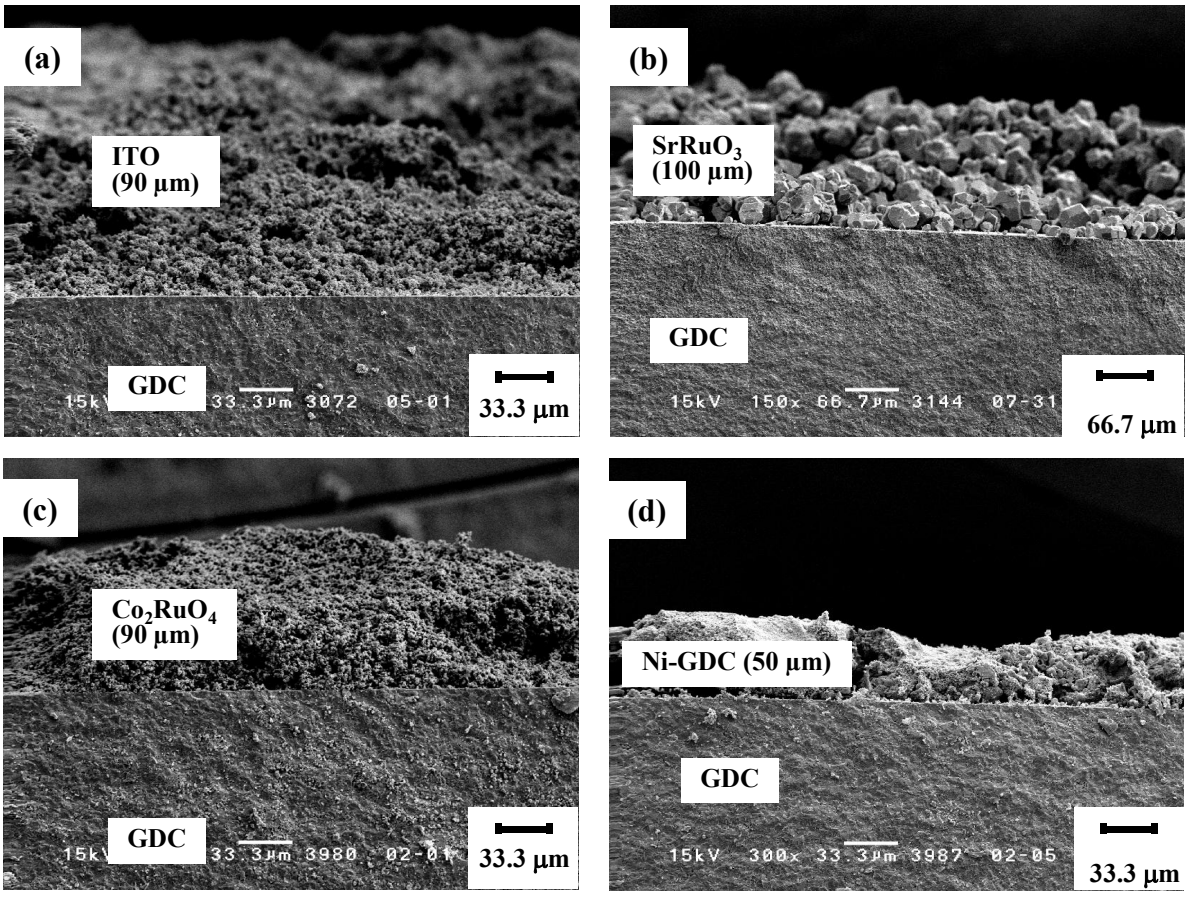

Fig. 3.4 Microstructures of (a) ITO, (b) $SrRuO_3$, (c) Co_2RuO_4 cathode and (d) Ni-GDC anode on GDC electrolyte.

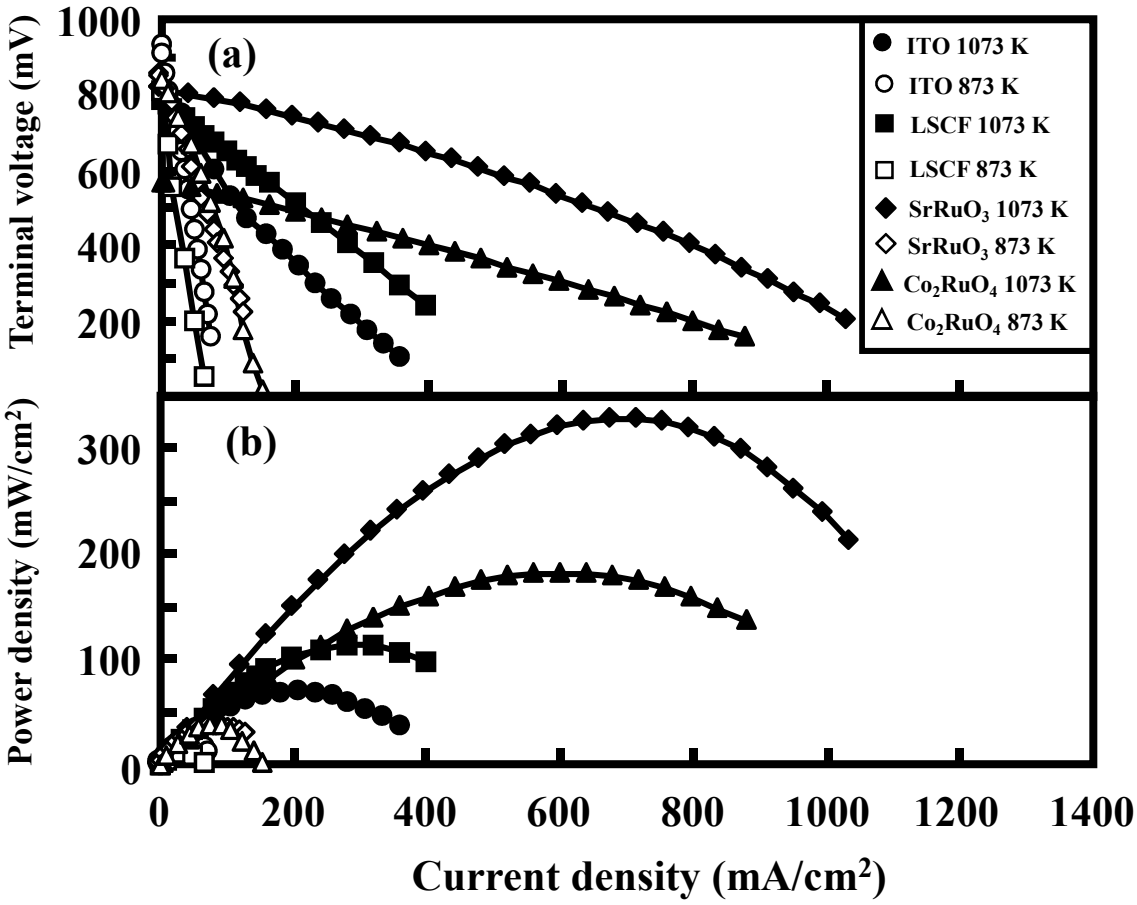

Fig. 3.5 Terminal voltage (a) and electric power density (b) as a function of current density for the ITO, LSCF, $SrRuO_3$ or Co_2RuO_4 cathode / GDC electrolyte / Ni-GDC anode cell using a 3 vol% H_2O-containing H_2 fuel at 873 and 1073 K.

at 1073 K. The results measured in Fig. 3.5 indicate that $SrRuO_3$ cathode enhances the power density at 1073 K as compared with ITO, Co_2RuO_4 and LSCF cathode.

The V_{OCV} of the cell is given by Eq. (3.1),

$$V_{OCV} = \frac{RT}{4F}\int_{Po_2\,(a)}^{Po_2\,(c)} \frac{\sigma_i}{\sigma_i + \sigma_e}\, d \ln Po_2 \tag{3.1}$$

where R is the gas constant, T the temperature, F the Faraday constant, Po_2 (c) the oxygen partial pressure at cathode and Po_2 (a) the oxygen partial pressure at anode, σ_i the oxide ion conductivity and σ_e the electronic conductivity. The oxide ion conductivity σ_i of GDC was reported in the previous paper[10] and expressed by Eq. (3.2),

$$\sigma_i = \frac{\sigma_0}{T}\exp\left(-\frac{E_a}{RT}\right) \tag{3.2}$$

where σ_0 is the constant and E_a the activation energy for the migration of oxide ions. Equation (3.2) is independent of the oxygen partial pressure. The electronic conductivity at a low oxygen partial pressure is expressed by Eq. (3.3) as a function of oxygen partial pressure,

$$\sigma_e = CP_{O_2}^{-\frac{1}{n}} \tag{3.3}$$

where C and n are the constants. In the previous paper[11], σ_e of GDC was measured in a temperature range from 773 to 1073 K by Hebb-Wagner method. Combination of Eqs. (3.1), (3.2) and (3.3) gives Eq. (3.4),

$$V_{OCV} = \frac{nRT}{4F}\ln\left[\frac{P_{O_2}(c)^{1/n} + \left(\frac{C}{\sigma_i}\right)}{P_{O_2}(a)^{1/n} + \left(\frac{C}{\sigma_i}\right)}\right] \tag{3.4}$$

The Po_2 (a) values measured for cells 1, 2, 3 and 4 at 873-1073 K were 1.3×10^{-22} – 1.6×10^{-17} Pa, 1.5×10^{-22} – 1.7×10^{-17} Pa, 9.6×10^{-23} – 4.9×10^{-18} Pa and 9.1×10^{-23} – 1.0×10^{-17} Pa respectively. The V_{OCV} values were calculated to be 1.113 − 1.121 V and 1.020 − 1.031 V at 873 and 1073 K, respectively. The measured V_{OCV} values were lower than the calculated values. When the parallel circuit shown in Fig. 3.6 is assumed for the cell in the open circuit condition, V_{OCV} is expressed by Eq. (3.5),

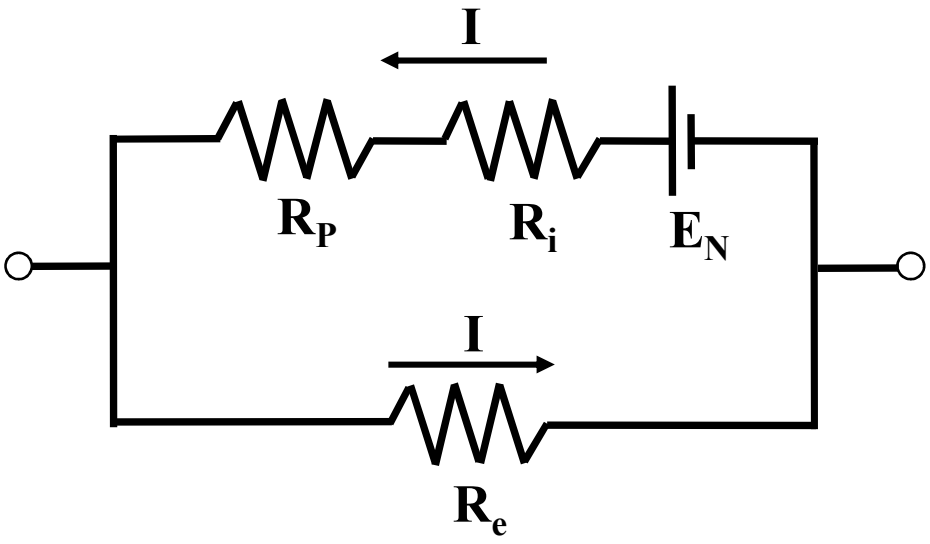

R_i : resistance of oxide ion conduction
R_e : resistance of electronic conduction
R_P : resistance of electrode
E_N : voltage calculated by Nernst equation
I : internal short circuit current

Fig. 3.6 Parallel circuit assumed for the cell in the open circuit condition.

$$V_{OCV} = t_i E_N \left(1 - \frac{IR_P}{E_N} \right) \quad (3.5)$$

where E_N is the voltage calculated by Nernst equation, t_i the oxide ion transference number, R_P the resistance of electrode and I the internal short circuit current. This equation indicates that V_{OCV} decreases with increasing R_P and I values. That is, V_{OCV} is influenced by the characteristics of electrode and the thickness of electrolyte[12]. Figure 3.7 shows the relationship between $E_N V_{OCV}$ and E_N for the cells with ITO and $SrRuO_3$ cathode. The solid line represents the curve predicted by Eq. (3.5). The measured $E_N V_{OCV}$ value showed the tendency of Eq. (3.5).

3.3.3 Ohmic Resistance and Overpotential

The ohmic resistance and overpotential at the cathode were separated by analyzing the AC impedance spectroscopy during the measurement of power density. Figure 3.8 (a) shows the AC impedance spectrum between cathode and reference electrode on the GDC surface of the cathode side at 1073 K under open-circuit (10 mA AC current). The measured data were fitted with the equivalent circuit shown in Fig. 3.8 (b). The fitted equivalent circuits consisted of ohmic resistance, one or two resistance – capacitance parallel circuit and a resistance – inductance parallel circuit. The ohmic resistance corresponds to the intrinsic resistance of ITO cathode. The each resistance – capacitance parallel circuit may be related to the elementary process of the reactions at the cathode involving the diffusion of O_2 gas, the dissociative adsorption of O_2 on the cathode surface, the surface diffusion of O atom to the triple phase boundary of the electrolyte – cathode – O_2 gas and diffusion of oxide ion into the electrolyte. The overpotential at the cathode was estimated by eliminating the voltage drop due to the ohmic resistance from the whole voltage drop at the cathode. The voltage drop at the cathode was estimated from the terminal voltage between the cathode and the reference electrode on the GDC surface of cathode side. The study on the impedance spectroscopy is shown in the chapter 5. Figures 3.9 (a), (b), (c) and (d) show the voltage drop at the cathode at 1073 K with ITO (a), LSCF (b), $SrRuO_3$ (c) and Co_2RuO_4 (d) cathode, respectively. Similarly, Fig. 3.10 (a), (b), (c) and (d) show the voltage drop at 873 K for ITO (a), LSCF (b), $SrRuO_3$ (c) and Co_2RuO_4 (d) cathode, respectively. The relatively large voltage drop

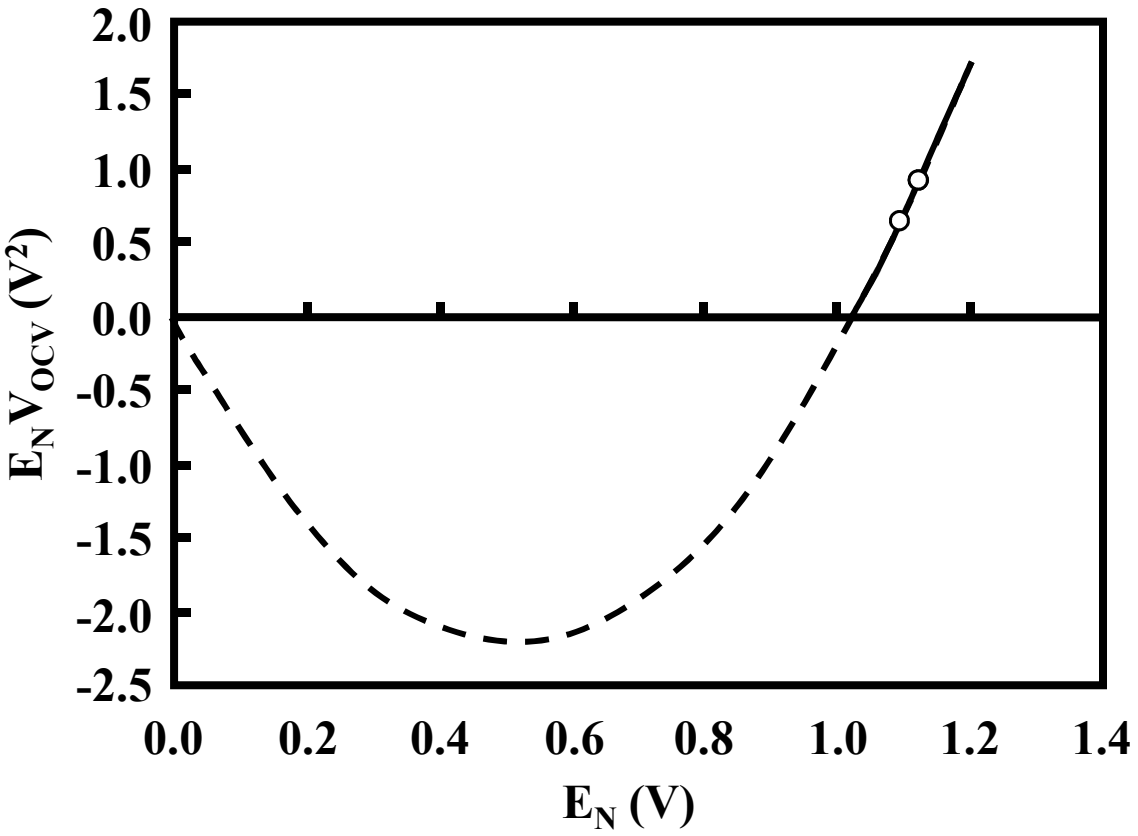

Fig. 3.7 Relationship between $E_N V_{OCV}$ and E_N for the cells with ITO and $SrRuO_3$ cathode at 1073 K. The solid line represents the curve predicted by Eq. (3.5) (t_i = 0.91).

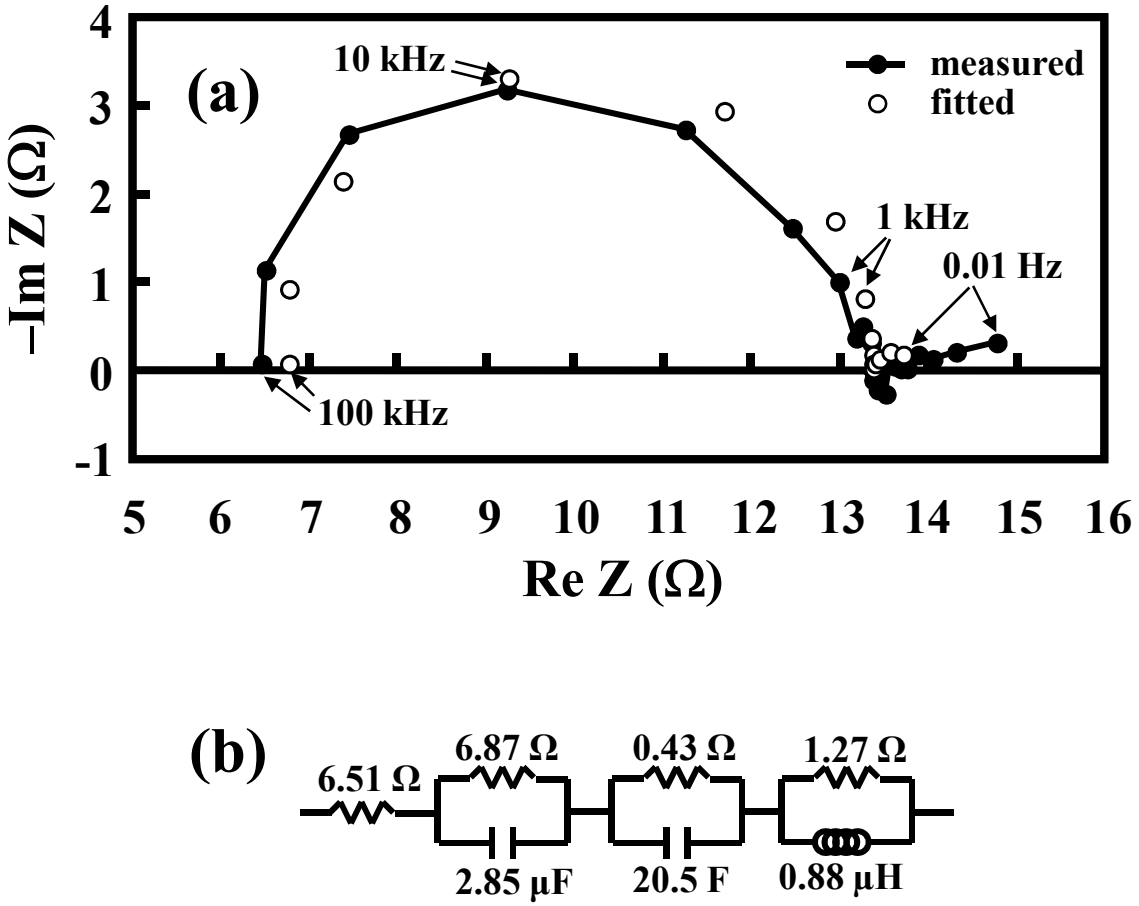

Fig. 3.8 Typical AC impedance spectrum (a) between cathode and reference electrode of the cell with ITO cathode measured at 1073 K under open-circuit (AC 10 mA) and corresponding equivalent circuit (b).

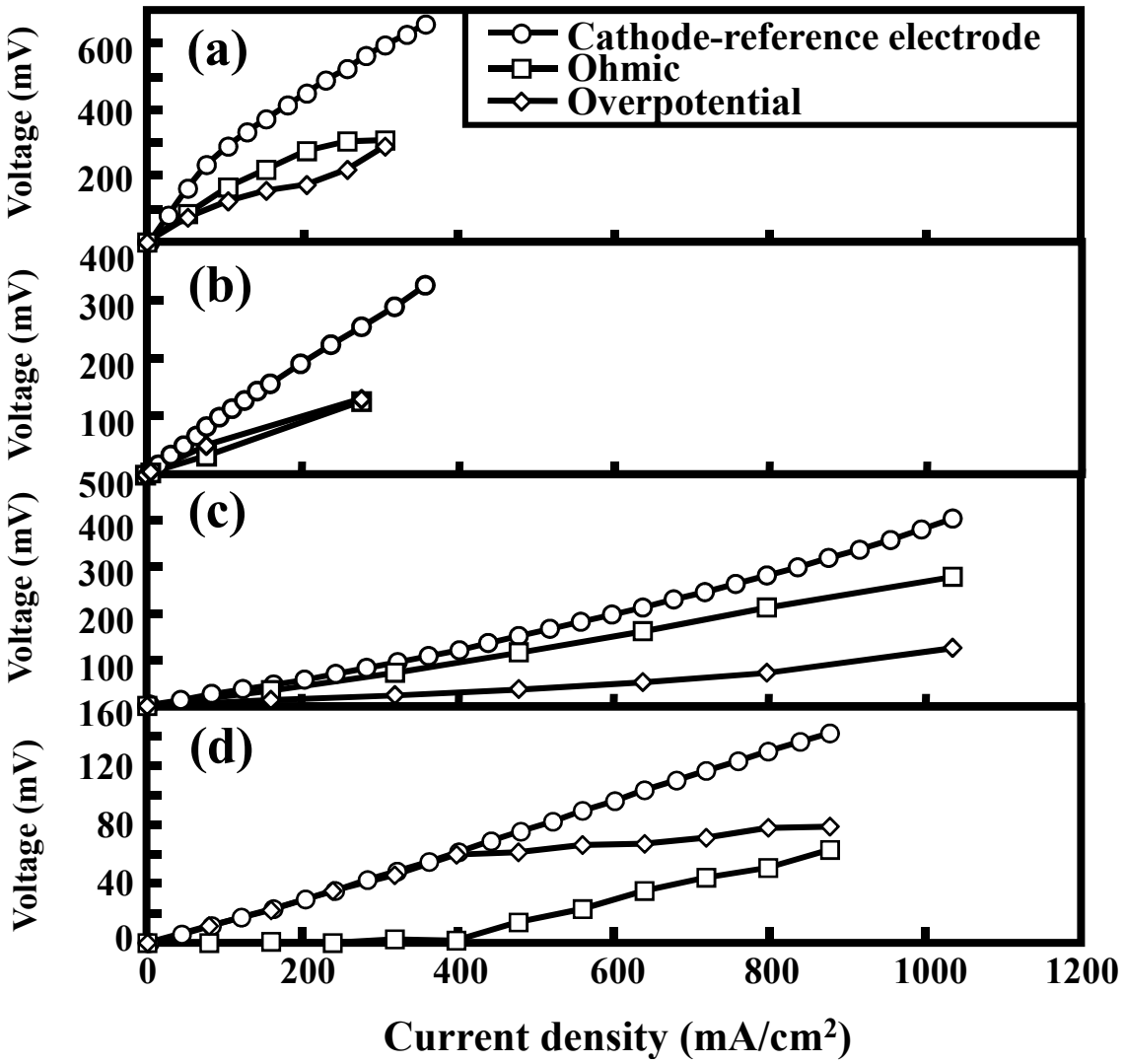

Fig. 3.9 Terminal voltage drop between cathode and reference electrode of (a) ITO / GDC / Ni-GDC cell, (b) LSCF / GDC / Ni-GDC cell, (c) $SrRuO_3$ / GDC / Ni-GDC cell and (d) Co_2RuO_4 / GDC / Ni-GDC cell at 1073 K.

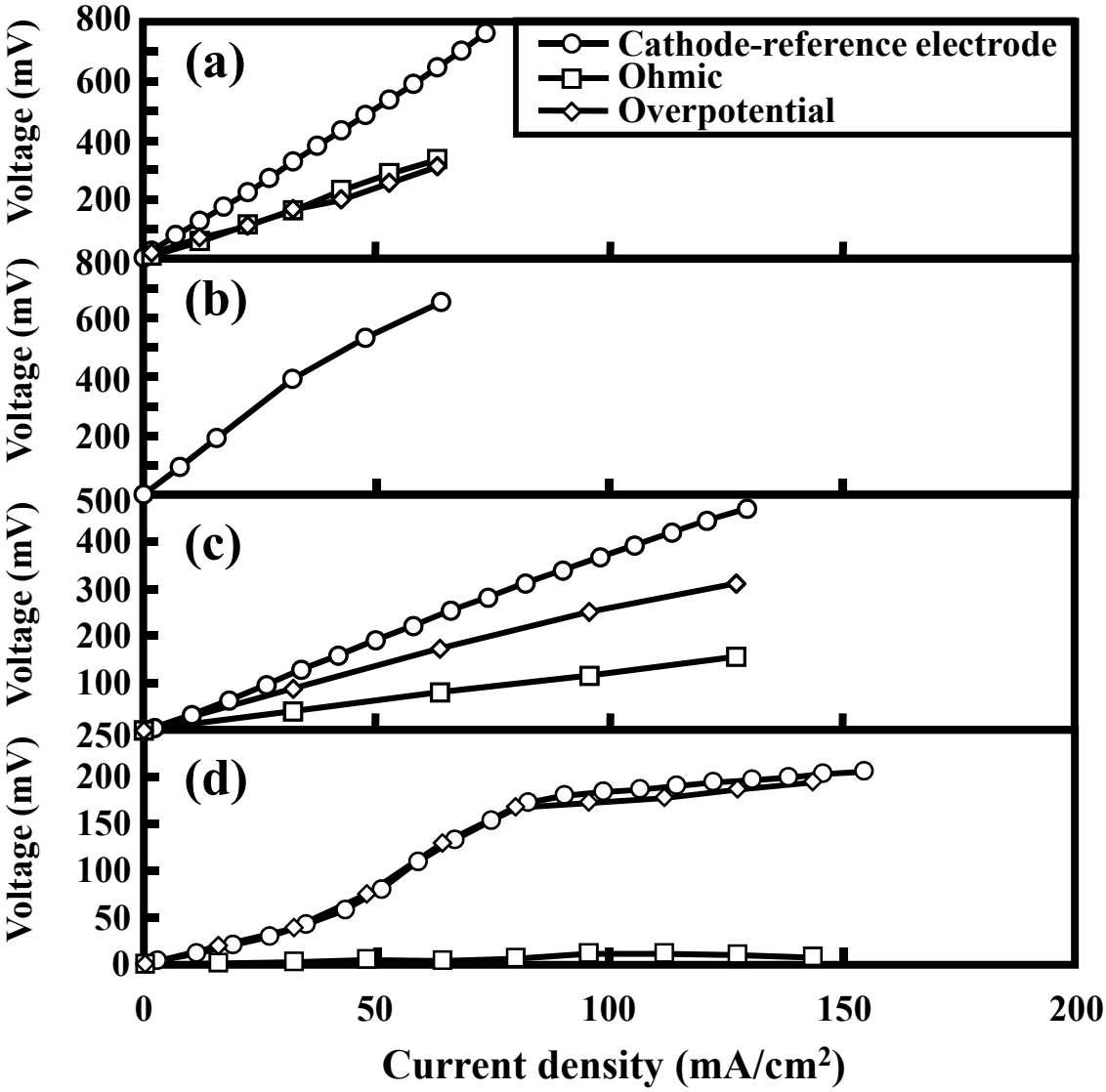

Fig. 3.10 Terminal voltage drop between cathode and reference electrode of (a) ITO / GDC / Ni-GDC cell, (b) LSCF / GDC / Ni-GDC cell, (c) $SrRuO_3$ / GDC / Ni-GDC cell and (d) Co_2RuO_4 / GDC / Ni-GDC cell at 873 K.

due to the ohmic resistance was observed for the ITO cathode at 1073 K. The ITO compacts were sintered at 1773 K in air and in O_2 atmosphere ($Po_2 = 1.01\times10^5$ Pa) to relative density 74.2 and 87.1 %, respectively. In the sintering in air, ITO decomposed to In_2O_3 and SnO_2, resulting in the increase of electrical resistivity. On the other hand, decomposition of ITO was prevented in O_2 atmosphere. Therefore, the relatively high ohmic resistance of ITO may be decreased by heating the cathode in O_2 atmosphere. Both the ohmic resistance and overpotential were lowest for the Co_2RuO_4 cathode among the investigated cathodes. The overpotential for the $SrRuO_3$ cathode was lower than that for ITO or LSCF cathode in spite of the decreased length of triple phase boundary for the $SrRuO_3$ cathode as shown in Fig. 3.4 (b). $SrRuO_3$ accelerates the reduction of adsorbed O_2 molecules to O^{2-} ions and the diffusion of oxide ion into the electrolyte. Figures 3.11 and 3.12 show the voltage drop at the Ni-GDC anode at 1073 and 873 K, respectively, for cell 1, 2, 3 and 4. The voltage drop at the anode was estimated from the terminal voltage between the anode and the reference electrode on the GDC surface of anode side. The voltage drop at the Ni-GDC anode was small in the order of cell 1 < cell 2 < cell 3 < cell 4 at 1073 K, and cell 1 ≈ cell 4 < cell 2 < cell 3 at 873 K. The results in Figs. 3.11 and 3.12 indicate that the voltage drop at the anode is not only affected by the thickness of the anode but also by the microstructure of the anode including the triple phase boundary and the porosity. The comparison of the data in Figs. 3.9, 3.10, 3.11 and 3.12 indicates that the voltage drop at the cathode is larger than that at the anode in these cells[13] except for the cell with Co_2RuO_4 cathode.

3.3.4 Reaction between GDC Powder and $SrRuO_3$ or Co_2RuO_4 Powder

It was reported that $La_{0.6}Sr_{0.4}CoO_3$ cathode with a high activity for the oxygen reduction reacted with YSZ electrolyte to form the poorly conducting interphases ($La_2Zr_2O_7$ and $SrZrO_3$), which resulted in the degradation of the performance of cathode[14]. The reaction between the GDC powder and $SrRuO_3$ or Co_2RuO_4 powder was investigated because the reaction between cathode and electrolyte changes the electrochemical properties of cathode and electrolyte. Figures 3.13 (a) and (b) show the X-ray diffraction patterns of the mixed powders of GDC and $SrRuO_3$ before and after heating at 1073 K for 10 h in air. The GDC powder did not react with the $SrRuO_3$

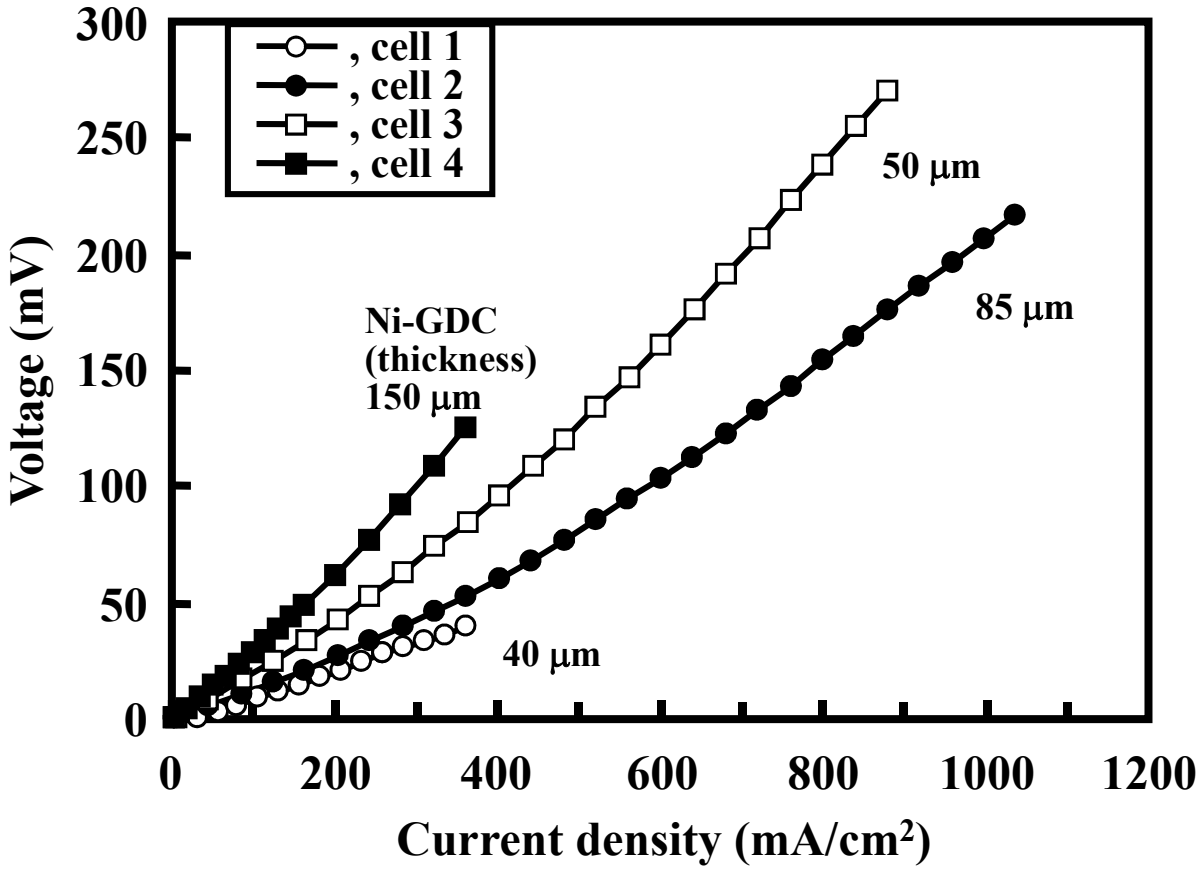

Fig. 3.11 Terminal voltage drop between anode (A) and reference electrode (RA) of ITO / GDC / Ni-GDC (cell 1), $SrRuO_3$ / GDC / Ni-GDC (cell 2), Co_2RuO_4 / GDC / Ni-GDC (cell 3) and LSCF / GDC / Ni-GDC (cell 4) at 1073 K.

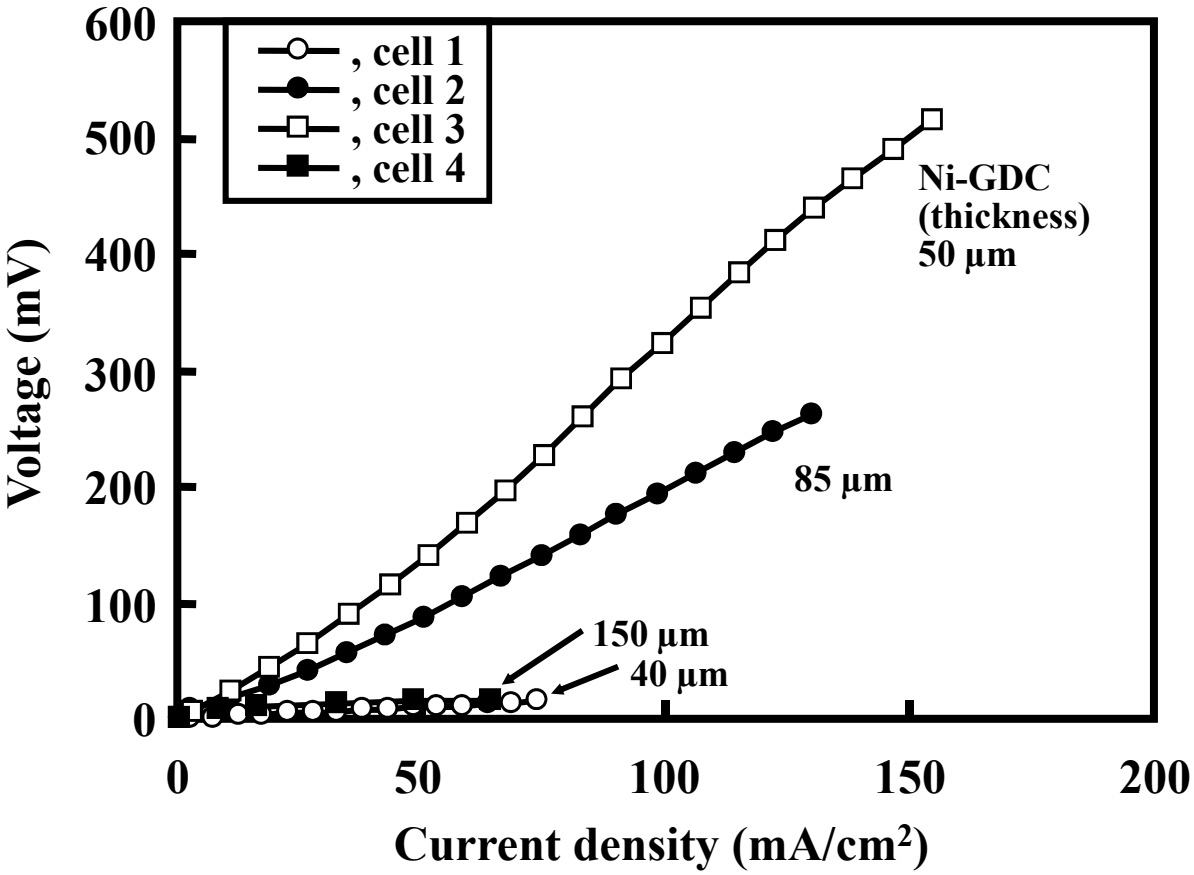

Fig. 3.12 Terminal voltage drop between anode (A) and reference electrode (RA) of ITO / GDC / Ni-GDC (cell 1), $SrRuO_3$ / GDC / Ni-GDC (cell 2), Co_2RuO_4 / GDC / Ni-GDC (cell 3) and LSCF / GDC / Ni-GDC (cell 4) at 873 K.

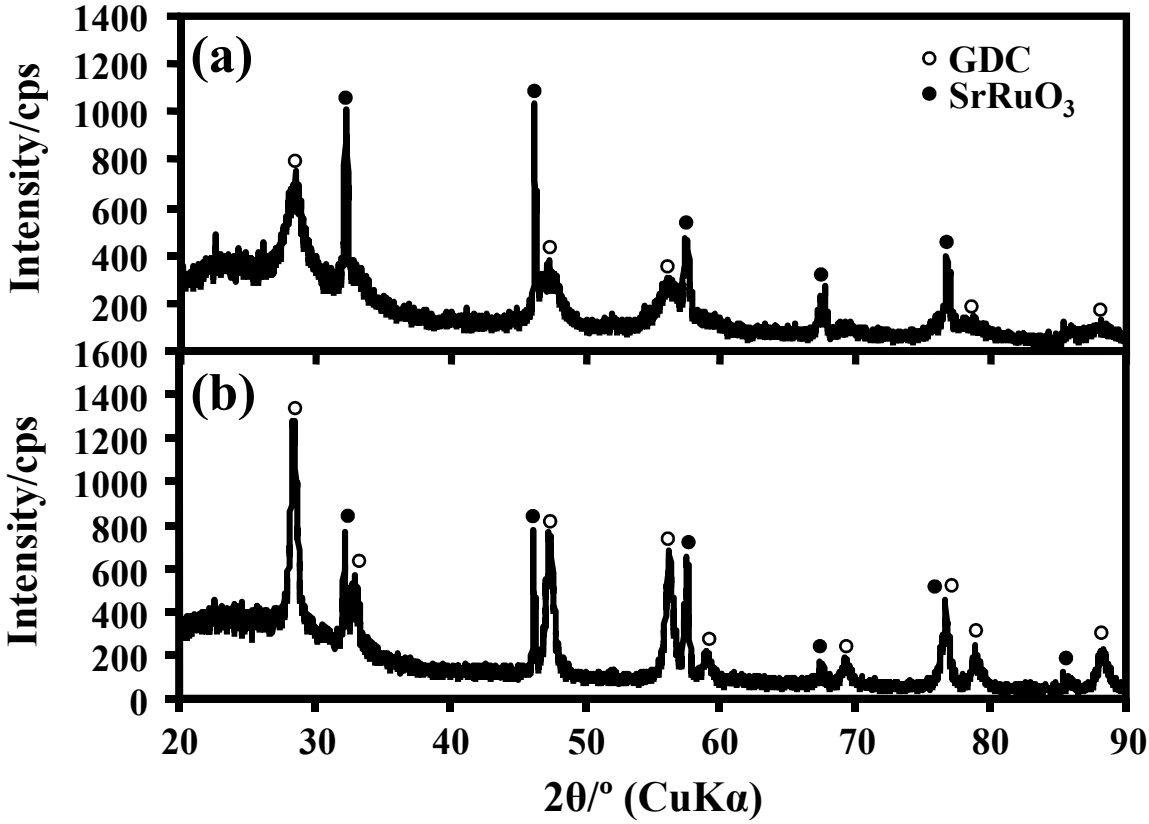

Fig. 3.13 X-ray diffraction patterns of the mixed powders of GDC and $SrRuO_3$ (a) before and (b) after heating at 1073 K for 10 h in air.

powder at 1073 K. The crystallinity of GDC powder calcined at 873 K was enhanced by heating at 1073 K. Similarly, Figure 3.14 (a) and (b) show the X-ray diffraction patterns of the mixed powders of GDC and Co_2RuO_4 before and after heating at 1073 K for 10 h in air. The X-ray diffraction pattern of the mixed powder after the heating showed new peaks ascribed to Co_3O_4 and $Gd_2Ru_2O_7$. The Co_3O_4 and $Gd_2Ru_2O_7$ were formed in the following processes.

$$Co_2RuO_4 + \frac{1}{3}O_2 \rightarrow RuO_2 + \frac{2}{3}Co_3O_4 \quad (3.6)$$

$$Ce_{0.8}Gd_{0.2}O_{1.9} + xRuO_2 \rightarrow Ce_{0.8}Gd_{0.2-x}O_{1.9-3x/2} + \frac{x}{2}Gd_2Ru_2O_7 \quad (3.7)$$

Co_2RuO_4 decomposed to RuO_2 and Co_3O_4 at 1073 K. The formed RuO_2 reacted with GDC to form $Gd_2Ru_2O_7$. The formation of $Gd_2Ru_2O_7$ on the GDC electrolyte surface may enhance the electronic conductivity of the electrolyte. The lower open circuit voltage at 1073 K for the Co_2RuO_4 / GDC / Ni-GDC cell may be attributed to the decrease of the oxide ion transference number for the GDC electrolyte. In addition, the overpotential for the formation of oxide ions was reduced by the formation of $Gd_2Ru_2O_7$. (Figs. 3.9 and 3.10).

3.4 Summary

The electrochemical properties were measured for ITO, $SrRuO_3$ or Co_2RuO_4 (cathode) / GDC (electrolyte) / Ni-GDC (anode) cells at 873 and 1073 K using 3 vol% H_2O-containing H_2 fuel and compared with the cell with LSCF cathode. The open circuit voltages of the cells with ITO, $SrRuO_3$, Co_2RuO_4 and LSCF cathode was 0.93, 0.85, 0.84 and 0.81 V at 873 K, respectively, and was 0.82, 0.82, 0.57 and 0.79 V at 1073 K, respectively. The maximum power densities of the cells with ITO, $SrRuO_3$, Co_2RuO_4 and LSCF cathode was 21, 36, 38 and 12 mW/cm^2 at 873 K, respectively, and was 71, 328, 183 and 113 mW/cm$_2$ at 1073 K, respectively. The voltage drop was larger for the cathode than for the anode except for the cell with Co_2RuO_4 cathode. The ohmic resistance and overpotential was large in the order of Co_2RuO_4 < $SrRuO_3$ < LSCF < ITO and in the order of $SrRuO_3$ < Co_2RuO_4 < LSCF < ITO, respectively. The $SrRuO_3$

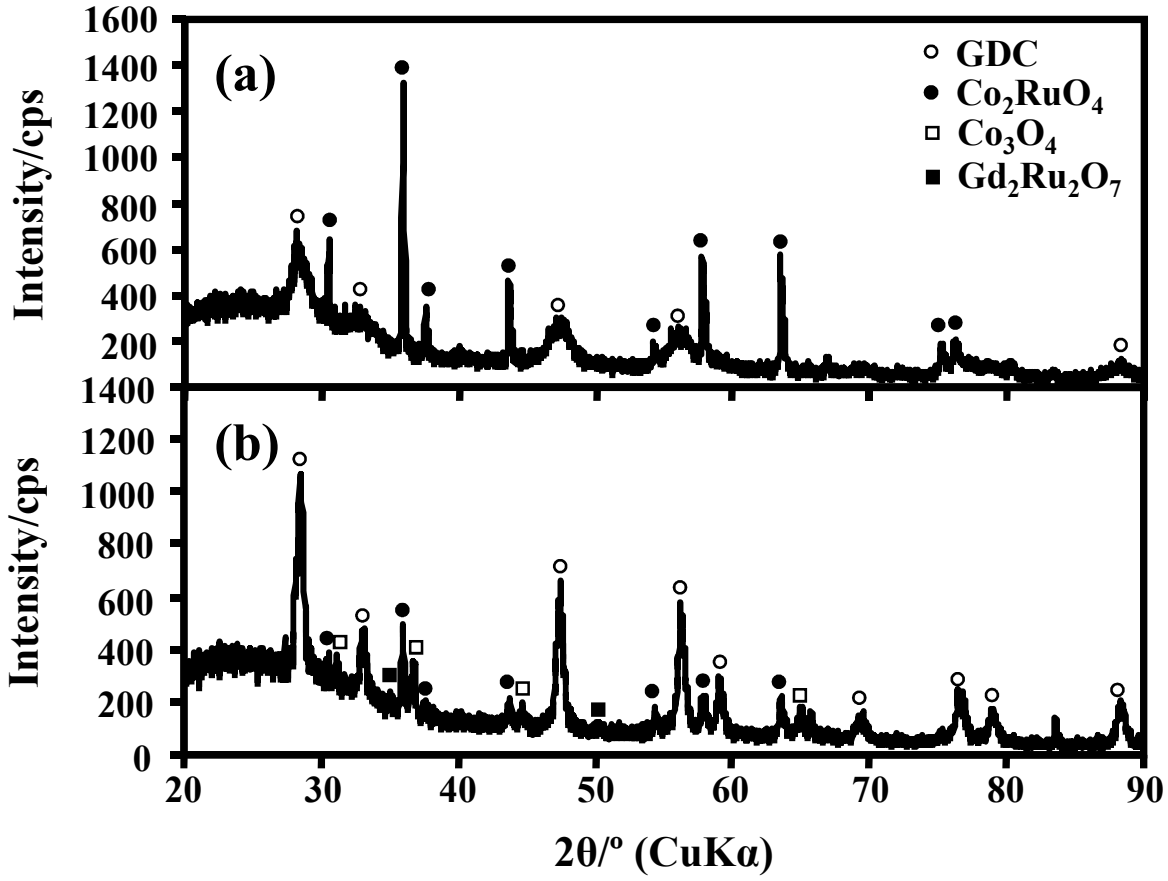

Fig. 3.14 X-ray diffraction patterns of the mixed powders of GDC and Co_2RuO_4 (a) before and (b) after heating at 1073 K for 10 h in air.

powder did not react with the GDC powder at 1073 K. On the other hand, the Co_2RuO_4 powder reacted with the GDC powder at 1073 K to form Co_3O_4 and $Gd_2Ru_2O_7$. The low open circuit voltage and the low voltage drop at the cathode for the cell with Co_2RuO_4 cathode may be due to the formation of $Gd_2Ru_2O_7$ at the interfaces between GDC electrolyte and Co_2RuO_4 cathode. Therefore, $SrRuO_3$ is the promising candidate of the cathode for low temperature SOFC in view points of the low overpotential and high phase compatibility with GDC electrolyte.

References

1) S.J. Skinner and J.A. Kilner, Solid State Ionics, 135, 709-712 (2000).

2) Z. Shao and S.M. Haile, Nature, 431, 170-173 (2004).

3) Y. Liu, C. Compson and M. Liu, Journal of Power Sources, 138, 194-198 (2004).

4) Y. Yoshimura, Y. Hirata, S. Sameshima, H. Sueyoshi, T. Doi and T. Horita, Adv. Tech. Mater. Mater. Proc. J., 9, 25-28 (2007).

5) M.L.B. Rao, A. Damjanovic and J. O'M. Bockris, J. Phys. Chem., 67, 2508-2509 (1963).

6) K.W. Kim, J.S. Lee, T.W. Noh, S.R. Lee and K.Char, Phys. Rev. B, 71, 125104 (2005).

7) B. Krutzsch and S. Kemmler-Sack, Mater. Res. Bull., 19, 1659 (1984).

8) S. Nishiyama, T. Mukozono and T. Hattori, Proceedings of the 11th Fall Meeting of The Ceramic Society of Japan (1998), p. 204.

9) G. Hiramatsu, Y. Hirata, S. Sameshima and N. Matsunaga, Mater. Sci. Forum, 544-545, 985-988 (2007).

10) S. Sameshima, H. Ono, K. Higashi, K. Sonoda, Y. Hirata and Y. Ikuma, J. Ceram. Soc. Jpn., 108, 1060-1066 (2000).

11) T. Shimonosono, Y. Hirata, Y. Ehira, S. Sameshima and T. Horita, J. Ceram. Soc. Jpn., Suppl., 112, S616-621 (2004).

12) T. Matsui, T. Kosaka, M. Inaba, A. Mineshige and Z. Ogumi, Solid State Ionics, 176, 663-668 (2005).

13) Y. Hirata, S. Sameshima and G. Hiramatsu, Proceedings of the 23rd International

Korea-Japan Seminar on Ceramics (2006), pp. 93-96.
14) T. Setoguchi, T. Inoue, H. Takebe, K. Eguchi, K. Morinaga and H. Arai, Solid State Ionics, 37, 217-221 (1990).

Chapter 4

Electrochemical Properties of Anode-Supported SOFC with GDC Thin Film

4.1 Introduction

The operation temperature of solid oxide fuel cell (SOFC) depends significantly on the ionic conductivity of the solid electrolyte used. The fabrication of dense thin film of solid electrolyte is a key factor to operate SOFC at a low temperature. The following processings have been reported in the preparation of thin solid electrolyte : slurry coating[1)], plasma sputtering[2)], chemical vapor deposition (CVD)[3)], sol-gel method[4)], and electrochemical vapor deposition[5)]. CVD process is applied to the formation of film with simple chemical composition because of a strict control of vapor pressures of precursors. In addition, the cost of the equipment for the vapor phase processes is high as compared with that of powder processing. Sol-gel processing with liquid precursors can produce the film with complicated chemical composition. However, a lot of time, labor and energy are used to make a crack-free film by the repeated sequence of coating-drying-firing. The doctor blade method is a low cost processing to produce a continuous film with constant thickness above 3 μm[6), 7)]. The specific area conductivity of GDC is shown in Fig. 1.3. The thickness of GDC electrolyte studied in chapter 3 was about 600 μm. The several 10 micro meter thickness is required to decrease the operation temperature from 1073 K to 873 K. This thickness is suitable for the fabrication of thin film by the doctor blade method.

On the other hand, the efficiency (ε) in terms of the loss of fuel due to the electronic conduction of electrolyte and the voltage drop due to the resistance of electrolyte should be considered for the practical use of SOFC with GDC electrolyte. The analytic solution for the charge transport in the mixed conductor is reported in the literatures[8), 9)]. The current densities ($I_{O^{2-}}$ and I_e) due to the flux of the oxide ions and the electrons are expressed by Eqs. (4.1) and (4.2), respectively,

$$I_{O^{2-}} = \frac{\sigma_{O^{2-}}}{2F}\frac{\partial \eta_{O^{2-}}}{\partial x}$$

$$= \frac{\sigma_{O^{2-}}}{2F}\frac{\partial \mu_O}{\partial x} + \frac{\sigma_{O^{2-}}}{F}\frac{\partial \eta_e}{\partial x} \tag{4.1}$$

$$I_e = \frac{\sigma_e}{F}\frac{\partial \eta_e}{\partial x} \tag{4.2}$$

where F is the Faraday constant, σ the conductivity, μ the chemical potential, η the electrochemical potential and x the coordinate. The subscripts stand for the chemical species. The chemical potential of the oxygen atom is expressed by Eq. (4.3) using the oxygen partial pressure (P_{O_2}),

$$\mu_O = \frac{1}{2}\mu_{O_2} = \frac{1}{2}\left(\mu^{\circ}_{O_2} + RT \ln P_{O_2}\right) \tag{4.3}$$

Equation (4.4) shows the relationship among the electrochemical potential (η_e) and chemical potential (μ_e) of electron, and the electric potential (ϕ).

$$\eta_e = \mu_e - F\phi \tag{4.4}$$

The efficiency (ε) is expressed by Eq. (4.5),

$$\varepsilon = \frac{I_{ext} V_{term.}}{I_{O^{2-}} E} \tag{4.5}$$

where I_{ext}, $I_{O^{2-}}$, and E are the external current density, current density due to the flux of the oxide ions and voltage calculated by Nernst equation, respectively. These values are expressed by Eqs. (5.6), (5.5) in chapter 5 and (1.5). $V_{term.}$ is the terminal voltage and is expressed by Eq. (4.6),

$$V_{term.} = \frac{RT}{4F}\ln\frac{P_{O_2}(0)}{P_{O_2}(L)} + \frac{nRT}{4F}\ln\left[\frac{\sigma_{O^{2-}} - rCP_{O_2}(0)^{-1/n}}{\sigma_{O^{2-}} - rCP_{O_2}(L)^{-1/n}}\right] \tag{4.6}$$

where r is the ratio of $I_{O^{2-}}$ / I_e (I_e : current density due to the flux of the electrons), L is the thickness of the electrolyte, and $P_{O_2}(0)$ and $P_{O_2}(L)$ is the oxygen partial pressures at x = 0 and x = L, respectively. Equation (4.6) is obtained by the integration of Eq. (4.1) and the substitution of Eqs. (4.3) and (4.4). The substitution of Eqs. (1.5), (4.6), (5.5) and (5.6) into Eq. (4.5) gives Eq. (4.7),

$$\varepsilon = \left(1 + \frac{1}{r}\right)\left\{1 + n\frac{\ln\left[\dfrac{\sigma_{O^{2-}} - rCP_{O_2}(0)^{-1/n}}{\sigma_{O^{2-}} - rCP_{O_2}(L)^{-1/n}}\right]}{\ln\dfrac{P_{O_2}(0)}{P_{O_2}(L)}}\right\} \quad (4.7)$$

The efficiency is expressed as a function of the r value. Under the operation condition of SOFC, the r value is smaller than −1. The minus sign is due to the opposite flows of the oxide ions and the electrons. Figure 4.1 shows the relationship between the log |r| (absolute value of r) and ε (efficiency) at 873 and 1073 K. The efficiencies are calculated under the conditions of $P_{O_2}(0) = 2.1 \times 10^4$ Pa, $P_{O_2}(L) = 1.0 \times 10^{-22}$ Pa, $\sigma_{O^{2-}} = 2.05 \times 10^{-2}$ S/cm, n = 6.30 and C = 2.18×10^{-7} S/cm at 873 K, and $P_{O_2}(0) = 2.1 \times 10^4$ Pa, $P_{O_2}(L) = 1.0 \times 10^{-17}$ Pa, $\sigma_{O^{2-}} = 1.25 \times 10^{-1}$ S/cm, n = 5.79 and C = 2.58×10^{-5} S/cm at 1073 K. The efficiency increases with increasing log |r| value and reaches the maximum approximately at log |r| = 1. The decreases of efficiency at log |r| < 1 and log |r| > 1 are due to the loss of fuel and the drop of terminal voltage, respectively. The terminal voltage is expressed as a function of the r value by Eq. (4.6). The terminal voltage at log |r| = 1 are 1.01 and 0.78 V at 873 and 1073 K, respectively. While, the external current density is expressed as a function of the r and L value by Eq. (5.6). Figure 4.2 shows the relationship between I_{ext} (external current density) and 1/L (thickness of electrolyte) at log |r| = 1. The I_{ext} value is proportional to the 1/L value. Then, the external current density for maximum efficiency varies with the thickness of electrolyte.

In this chapter, the $Ce_{0.8}Gd_{0.2}O_{1.9}$ (Gd-doped ceria, GDC) electrolyte thin film supported by the NiO-GDC anode was fabricated by the doctor blade method. Then, the electrochemical properties of the anode-supported SOFC with GDC were measured.

4.2 Experimental Procedure

4.2.1 Powder Preparation of SOFC Component

The GDC powder was prepared by heating the oxalate solid solution at 873 K and was milled with alumina ball for 24 h. The milled GDC powder was immersed into a 1.4 M $Ni(NO_3)_2$ solution to make a cermet anode with the volume ratio of Ni / GDC =

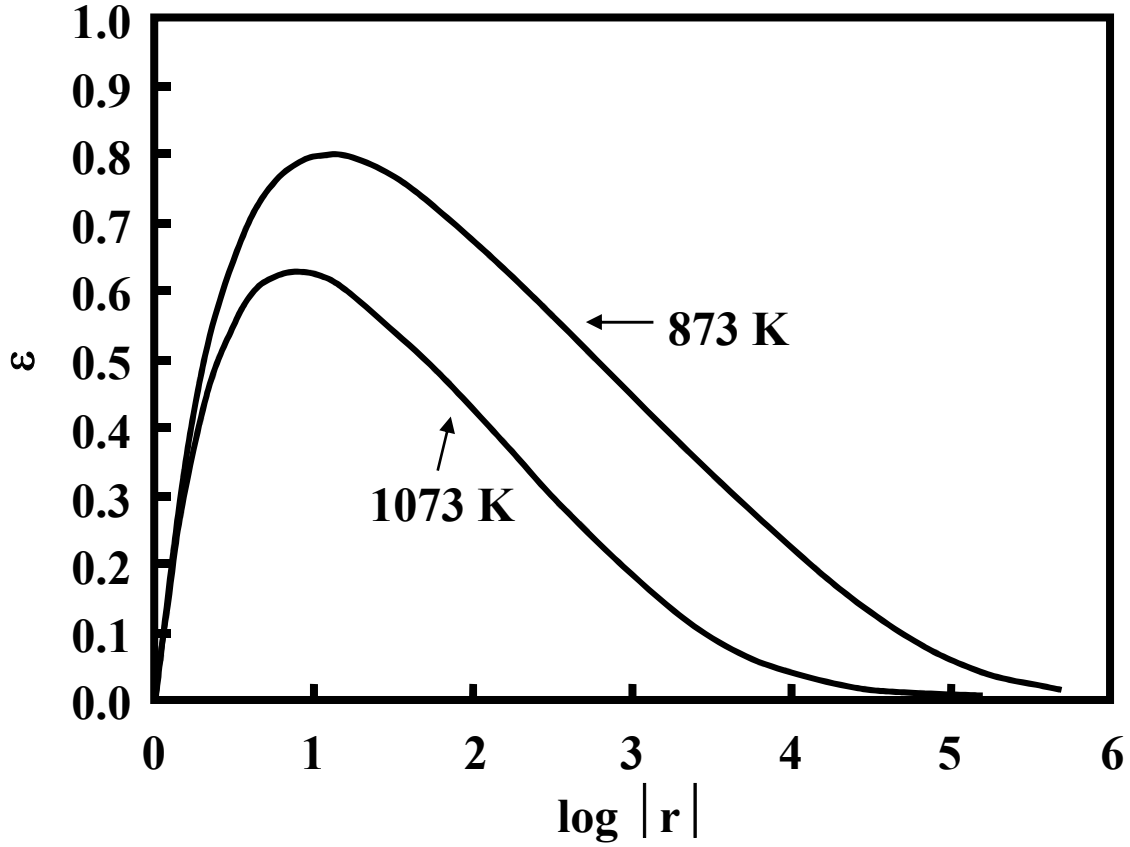

Fig. 4.1 Relationship between log |r| (absolute value of r) and ε (efficiency).

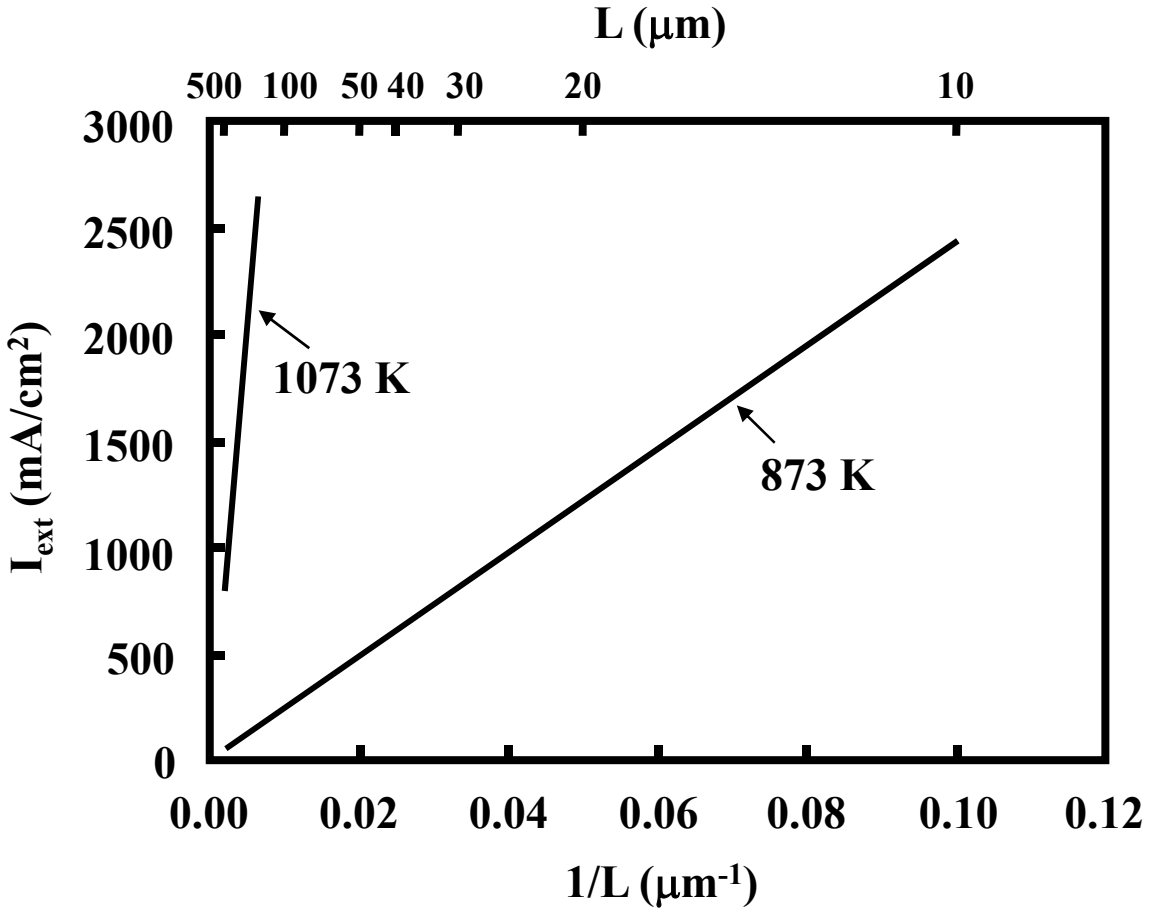

Fig. 4.2 Relationship between I_{ext} (external current density) and 1/L (thickness of electrolyte) at log $|r| = 1$.

40 / 60. The 0.2 M mixed solution of $RuCl_3$ and $Sr(NO_3)_2$ with the molar ratio of Ru / Sr = 1 / 1 was added into 1 M NH_4OH solution and then freeze-dried. The $SrRuO_3$ powder was formed by heating the freeze-dried powder at 1273 K for 2 h in air.

4.2.2 Fabrication of Anode-Supported SOFC by the Doctor Blade Method

The suspension of 15 vol% of the GDC powder was prepared in the mixed solution with the volume ratio of isopropanol / toluene = 2 / 1 by adding 9 mass% polyethylene glycol and 5 mass% polyvinyl butyral. The suspension were stirred for 24 h and then consolidated on polyester sheet by doctor blade (DP-100, Tsugawa Seiki Seisakusho, Tokyo) at a transfer rate of 15 cm/min. The front and back blade clearance was 170 and 250 μm, respectively. The formed film was left at room temperature for 24 h. The dried film was cut in a circle of 21.5 mm diameter. The NiO-GDC powder was pressed uniaxially at 25 MPa to a pellet with 22 mm diameter and 2 mm thickness. The NiO-GDC pellet and the GDC film were layered and then co-pressed uniaxially at 50 MPa. The co-pressed compacts were co-sintered at the different temperatures of 1673 and 1773 K for 4 h in air. The microstructure of the NiO-GDC / GDC composite was observed by the scanning electron microscope (SM-300, Topcon Co., Japan). The distribution of Ni, Ce and Gd elements in the cross section of the NiO-GDC / GDC composite was evaluated by electron probe microanalyser (EMX-SM7, Shimadzu Co., Kyoto, Japan).

4.2.3 Measurement of Cell Performance

The $SrRuO_3$ powder was dispersed at 15 vol% solid in the mixed solution of 90 vol% ethanol – 10 vol% ethyleneglycol. The prepared suspension was formed with screen (mesh: 250 μm) of thread diameter of 4 mm on the GDC surface of NiO-GDC / GDC composite. The printed $SrRuO_3$ powder was heated at 1273 K for 1 h in air. The Pt wire reference electrodes was fixed on the GDC surface of cathode side with Pt paste at 1273 K. A Pt mesh was attached to the each electrode with Pt paste. The GDC electrolyte with the cathode and anode was set to an alumina holder and sealed at 1173 K by using a glass O-ring. After cooling to 1073 – 773 K, the cell performance was measured by feeding air and 3 vol% H_2O-containing H_2 fuel into cathode and anode at 100 ml/min, respectively. The NiO at the anode is reduced to Ni by the reaction with H_2

fuel ($NiO + H_2 \rightarrow Ni + H_2O$). A direct current-voltage relation and AC impedance in the frequency range from 0.01 Hz to 100 kHz at the current of 10 mA were measured in the temperature range from 773 to 1073 K (As-510, NF Kairosekkei Block Co., Japan). The oxygen partial pressure of the fuel was monitored with yttria-stabilized zirconia oxygen gas sensor. The microstructure of the cell after the measurement of cell performance was observed using a scanning electron microscope (SM-300, Topcon, Co., Japan).

4.3 Results and Discussion

4.3.1 Microstructure of NiO-GDC / GDC Composite

The microstructures of the GDC surfaces ((a) and (c)) and the cross sections ((b) and (d)) for the NiO-GDC / GDC composites co-sintered at 1673 K ((a) and (b)) and 1773 K ((c) and (d)) are shown in Fig. 4.3. The grain growth and the decrease of the pore volume were observed in the GDC surface of the composite co-sintered at 1773 K. However, the separation of the NiO-GDC / GDC interface was partially observed in the composite co-sintered at 1773 K as shown in Fig. 4.3 (d), while the NiO-GDC / GDC interface adhered well in the composite co-sintered at 1673 K. The relative densities of the NiO-GDC pellets sintered at 1673 and 1773 K, measured by the Archimedes method, were 86.0 and 72.5 %, respectively. Therefore, the NiO-GDC / GDC composite co-sintered at 1673 K was used for the measurement of the cell performance. Figures 4.4 and 4.5 show the distributions of Ni (a), Gd (b) and Ce (c) elements in the cross sections of the NiO-GDC / GDC composites co-sintered at 1673 and 1773 K, respectively. Each figure show the similar distribution of the elements of Ni, Ce and Gd. The diffusion of Ni into the GDC film did not occur at 1673 and 1773 K, while the Ce and Gd distributed over the NiO-GDC / GDC composite.

4.3.2 Terminal Voltage and Power Density

Figure 4.6 shows the terminal voltage and electric power density for the cell supported by Ni-GDC anode with GDC electrolyte and $SrRuO_3$ cathode. The open circuit voltages (V_{OCV}) was 0.23, 0.46, 0.55 and 0.57 V at 773, 873, 973 and 1073 K, respectively. The maximum power density and the corresponding current density were 15 mW/cm^2 and 121 mA/cm^2 at 773 K, 100 mW/cm^2 and 439 mA/cm^2 at 873 K, 234

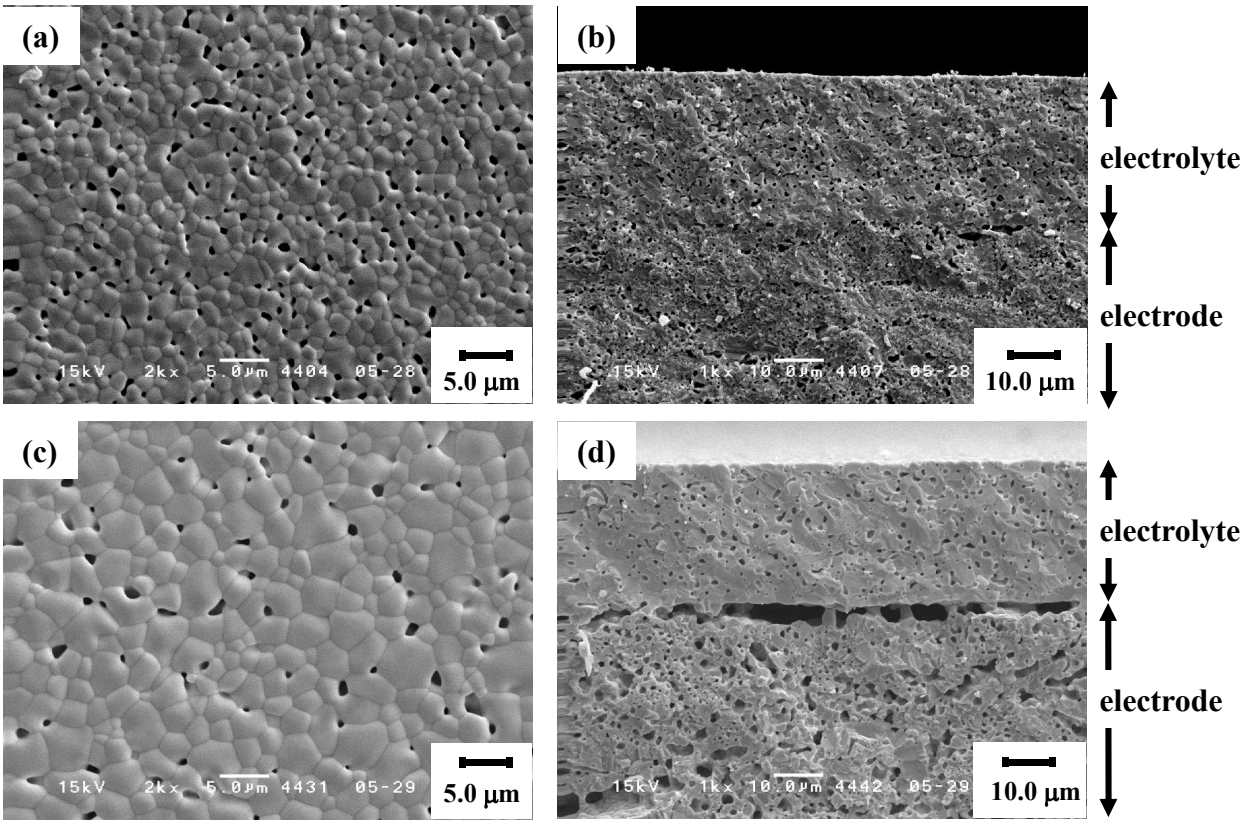

Fig. 4.3 Microstructures of the GDC surfaces ((a) and (c)) and the cross sections ((b) and (d)) for the NiO-GDC / GDC composites co-sintered at 1673 K ((a) and (b)) and 1773 K ((c) and (d)).

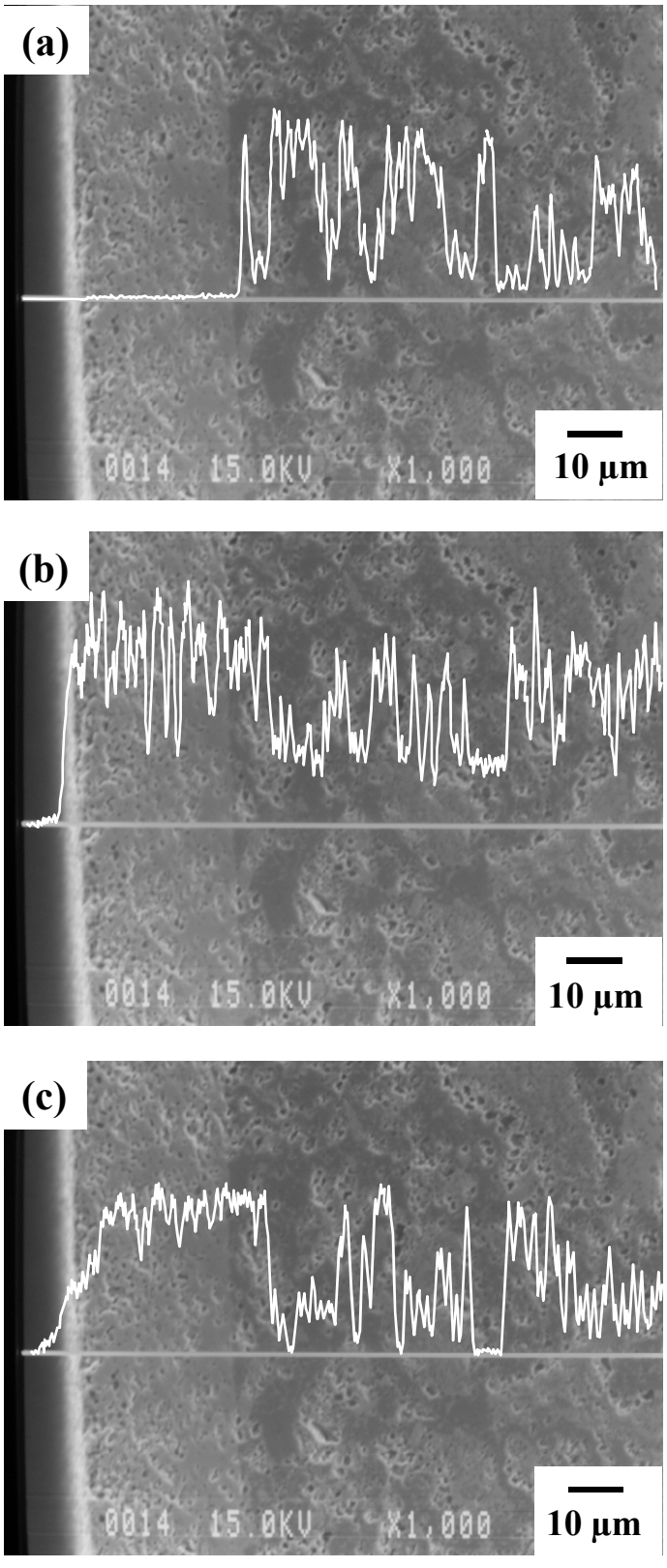

Fig. 4.4 Distributions of Ni (a), Gd (b) and Ce (c) elements in the cross section of the NiO-GDC / GDC composites co-sintered at 1673 K for 4 h in air.

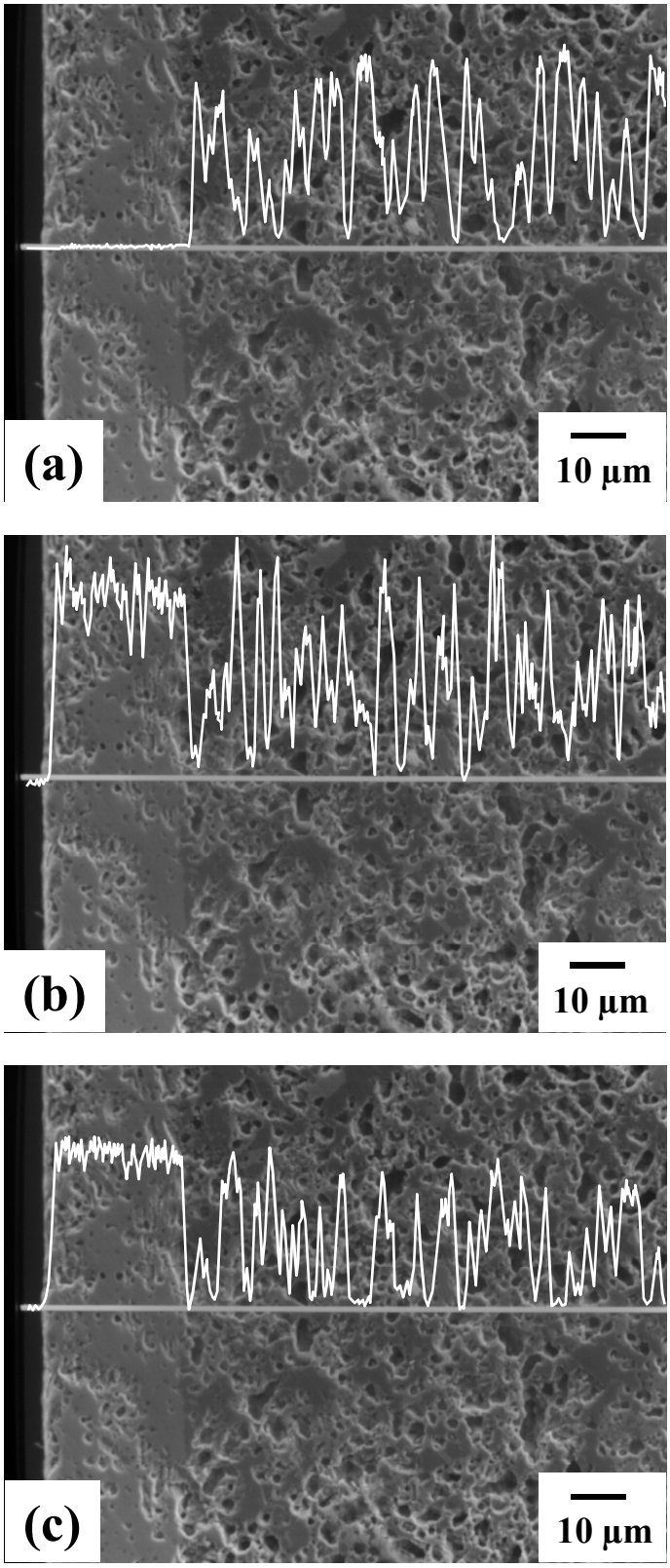

Fig. 4.5 Distributions of Ni (a), Gd (b) and Ce (c) elements in the cross section of the NiO-GDC / GDC composites co-sintered at 1773 K for 4 h in air.

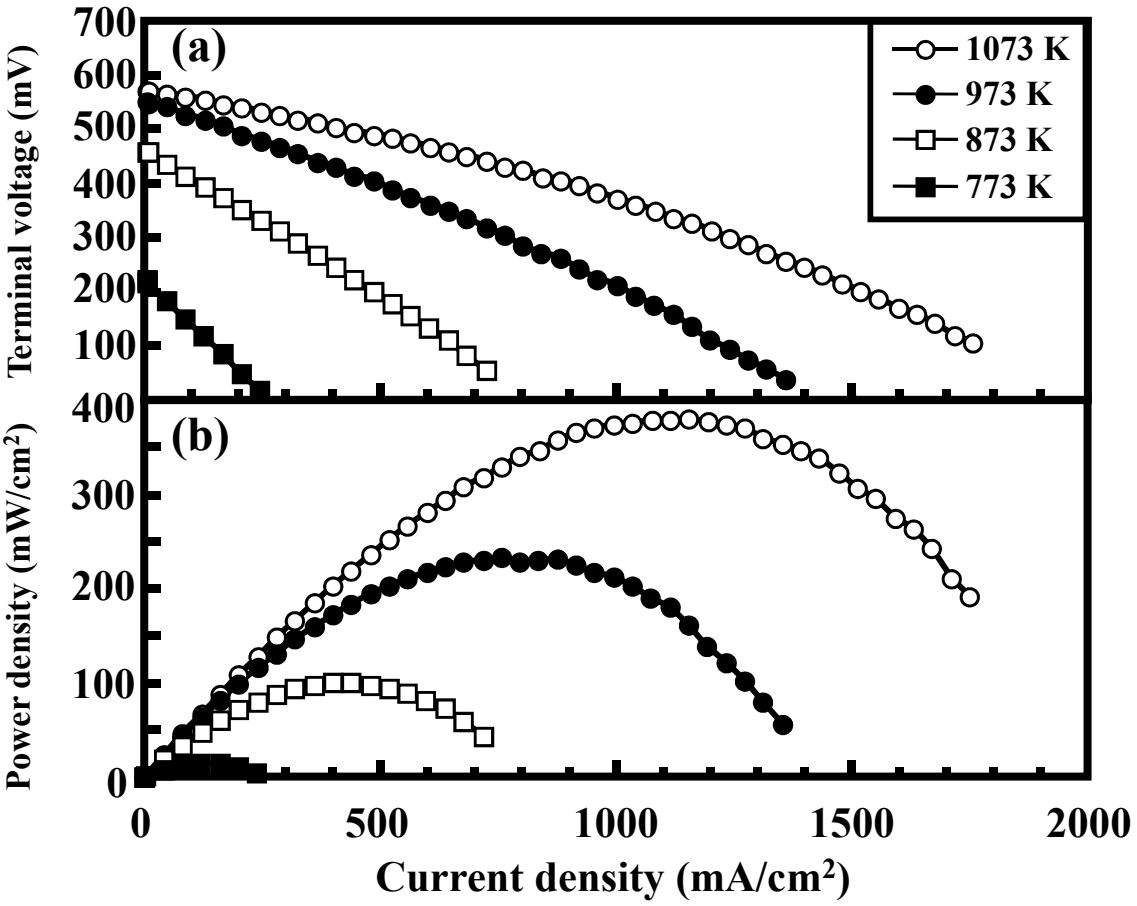

Fig. 4.6 Terminal voltage (a) and electric power density (b) as a function of current density for the Ni-GDC anode-supported SOFC with $SrRuO_3$ cathode and GDC electrolyte using a 3 vol% H_2O-containing H_2 fuel at the temperature range from 773 to 1073 K.

mW/cm^2 and 757 mA/cm^2 at 973 K, and 381 mW/cm^2 and 1154 mA/cm^2 at 1073 K. As compared with the cell 2 with $SrRuO_3$ cathode, 600 μm thick GDC electrolyte and Ni-GDC anode in chapter 3, the V_{OCV} values decreased by 0.25-0.39 V. On the other hand, the maximum power density increased for the anode-supported SOFC and was about 3 times as large as that of cell 2 ($SrRuO_3$ cathode) at 873 K. The oxygen partial pressures at the anode measured at 773, 873, 973 and 1073 K was 3.1×10^{-26}, 2.9×10^{-22}, 1.8×10^{-19} and 5.9×10^{-17} Pa, respectively. The V_{OCV} values were calculated using Eq. (3.4) to be 1.137, 1.101, 1.067 and 1.005 V at 773, 873, 973 and 1073 K, respectively. The measured V_{OCV} values were significantly lower than the calculated values. The open circuit voltage was also measured for the cell with Ni-YSZ anode-supported YSZ electrolyte thin film and Pt cathode, and was 0.56, 1.05, 1.09 and 1.08 V at 773, 873, 973 and 1073 K, respectively. The open circuit voltages for the cell with YSZ electrolyte thin film were close to the theoretical values calculated by Nernst equation, except for the open circuit voltage at 773 K. The significantly low V_{OCV} values for the cell with GDC electrolyte thin film are attributed to the following three factors, except for the V_{OCV} value at 773 K. At the first, the fuel gas leaked through the pores of GDC electrolyte shown in Figs. 4.3 (a) and (b) and the glass seal. In fact, the flux of the exhausted fuel was 96-98 % of that of the introduced fuel. Secondly, the GDC electrolyte was reduced by H_2 gas[10]. New pores may be formed by the reduction of GDC electrolyte[10]. The electrons formed by the reduction of the GDC electrolyte as expressed by Eq. (4.8) may increase the electronic conductivity of the GDC electrolyte,

$$O_O^{\times} + H_2 \rightarrow V_O^{\bullet\bullet} + H_2O + 2e' \qquad (4.8)$$

Thirdly, the internal short circuit current became larger because of the thinner electrolyte. As expressed by Eq. (3.5), the V_{OCV} value decreases with the increase of the internal short circuit current. In the open circuit condition, the current density due to the flux of the oxide ions is equal to that due to the flux of the electrons, which is expressed by Eq. (4.9),

$$I_{O^{2-}} + I_e = 0 \qquad (4.9)$$

The substitution of Eqs. (4.2) and (4.9) into Eq. (4.1) gives Eq. (4.10),

$$I_{O^{2-}} = \frac{1}{2F}\frac{\sigma_e \sigma_{O^{2-}}}{\sigma_e + \sigma_{O^{2-}}}\frac{\partial \mu_O}{\partial x} \tag{4.10}$$

The substitution of Eq. (4.3) into Eq. (4.10) gives Eq. (4.11),

$$I_{O^{2-}} = \frac{RT}{4F}\frac{\sigma_e \sigma_{O^{2-}}}{\sigma_e + \sigma_{O^{2-}}}\frac{\partial \ln P_{O_2}}{\partial x} \tag{4.11}$$

The oxide ion conductivity is expressed by Eq. (3.2) and is independent of the oxygen partial pressure. The electronic conductivity at a low oxygen partial pressure is expressed by Eq. (3.3) as a function of oxygen partial pressure. The integral of Eq. (4.11) gives Eq. (4.12),

$$I_{O^{2-}} = -I_e = \frac{nRT\sigma_{O^{2-}}}{4FL}\ln\left[\frac{\sigma_{O^{2-}} + CP_{O_2}(0)^{-1/n}}{\sigma_{O^{2-}} + CP_{O_2}(L)^{-1/n}}\right] \tag{4.12}$$

where L is the thickness of the electrolyte, and $P_{O_2}(0)$ and $P_{O_2}(L)$ is the oxygen partial pressures at x = 0 and x = L, respectively. In the open circuit condition, the internal short circuit current for the anode-supported SOFC with 30 μm thick electrolyte was calculated by Eq. (4.12) using the experimental data described above to be 13, 130, 858 and 3741 mA/cm^2 at 773, 873, 973 and 1073 K, respectively. The internal short circuit current calculated for the SOFC with 600 μm thick electrolyte described in chapter 3 is 7 and 218 mA/cm^2 at 873 and 1073 K, respectively, which is about 1/20 of that of the anode-supported SOFC. The V_{OCV} values in Table 1.2 were larger than those of the anode-supported SOFC measured in this study. The relatively small triple phase boundary in the $SrRuO_3$ cathode as shown in Fig. 3.1 (b) leads to the relatively high interfacial resistance, which may be reason that the V_{OCV} values for the anode-supported SOFC measured in this study were lower than those reported in the literatures.

4.3.3 Ohmic Resistance and Overpotential

The ohmic resistance and overpotential at the cathode were separated by analyzing the AC impedance spectroscopy during the measurement of power density. Figure 4.7 (a) shows the AC impedance spectrum between cathode and reference electrode at 1073 K under open-circuit (10 mA AC current). The measured data were fitted with the equivalent circuit shown in Fig. 4.7 (b). The fitted equivalent circuits consisted of ohmic resistance, one or two resistance – capacitance parallel circuits and one or two resistance

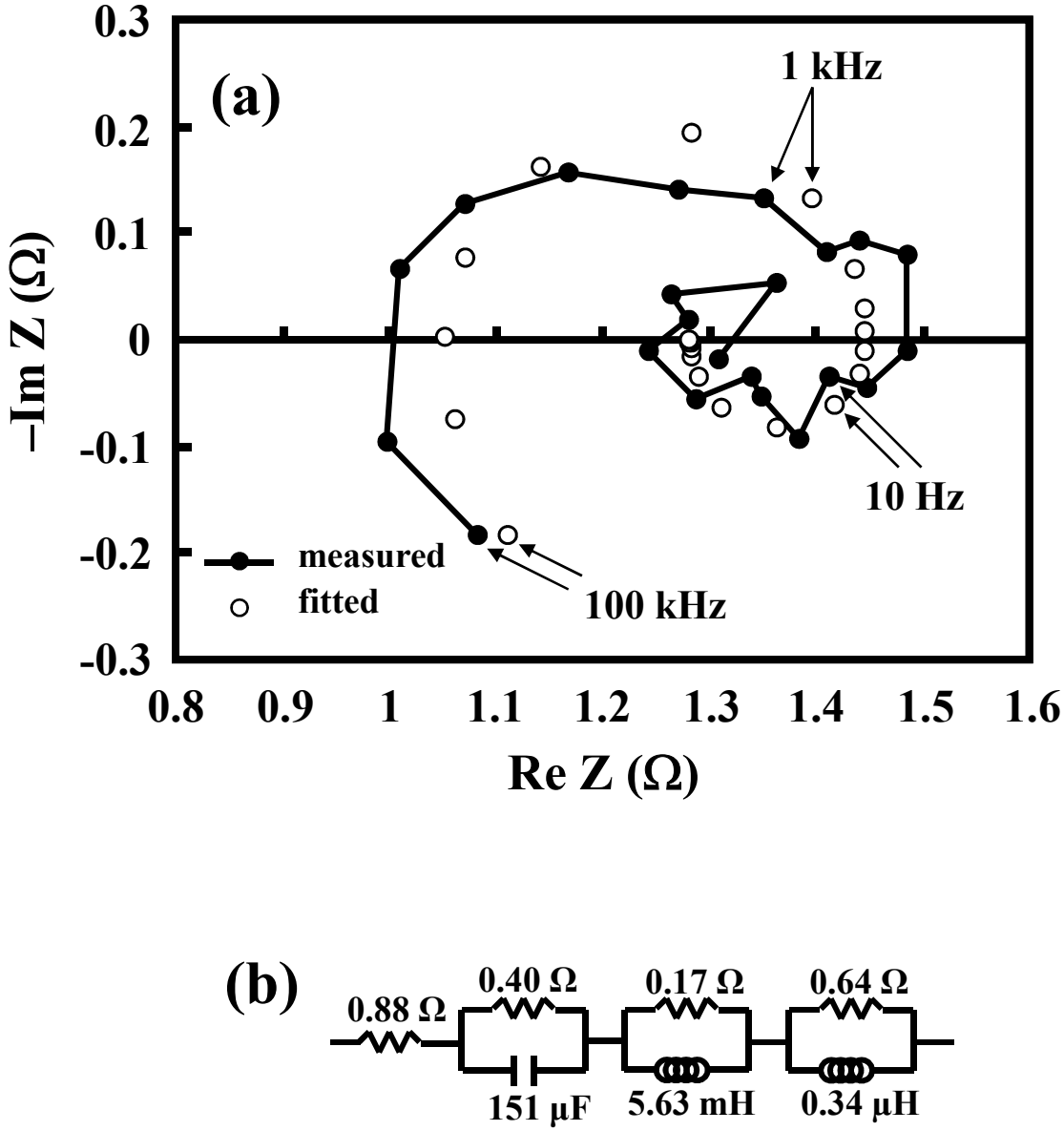

Fig. 4.7 AC impedance spectrum (a) between cathode and reference electrode of the anode-supported cell with $SrRuO_3$ cathode measured at 1073 K under open-circuit and corresponding equivalent circuit (b).

– inductance parallel circuit. The ohmic resistance corresponds to the intrinsic resistance of $SrRuO_3$ cathode. The overpotential at the cathode was estimated by eliminating the voltage drop due to the ohmic resistance from the whole voltage drop at the cathode. The voltage drop at the cathode was estimated from the terminal voltage between the cathode and the reference electrode on the GDC surface of cathode side. The study on the impedance spectroscopy is described in chapter 5. Figures 4.8 (a), (b), (c) and (d) show the comparison of the voltage drops between cathode and reference electrode, anode and reference electrode, and cathode and anode at 773, 873, 973 and 1073 K, respectively. The voltage drop at the cathode was almost equal to the voltage drop of the whole cell. The voltage drop at the anode was negligible[11), 12)]. Table 4.1 shows the voltage drops at the cathode, electrolyte and anode for the cells with $SrRuO_3$ cathode on the 600 μm thick GDC electrolyte and on the anode-supported GDC electrolyte under a direct current of 100 mA/cm^2 at 873 and 1073 K. The voltage drop at the electrolyte and anode was estimated from the terminal voltage between the anode and the reference electrode on the GDC surface of cathode side. The voltage drops at the cathode, electrolyte and anode decreased for the anode-supported SOFC, which may be related to the lower resistance of thinner electrolyte and the reaction on the electrode accelerated by the increase of the internal short circuit current. Figures 4.9 (a), (b), (c) and (d) show the voltage drops at the $SrRuO_3$ cathode at 773, 873, 973 and 1073 K, respectively. The contribution of the overpotential to the voltage drop at the cathode increased with increasing temperature.

4.4 Summary

The GDC thin film electrolyte supported by Ni-GDC anode was fabricated by the doctor blade method. The electrochemical properties of the anode-supported SOFC with GDC electrolyte and $SrRuO_3$ cathode were measured in the temperature range from 773 to 1073 K using the 3 vol% H_2O-containing H_2 fuel. The open circuit voltage was 0.23, 0.46, 0.55 and 0.57 V at 773, 873, 973 and 1073 K, respectively. The maximum power density and the corresponding current density were 15 mW/cm^2 and 121 mA/cm^2 at 773 K, 100 mW/cm^2 and 439 mA/cm^2 at 873 K, 234 mW/cm^2 and 757 mA/cm^2 at 973 K,

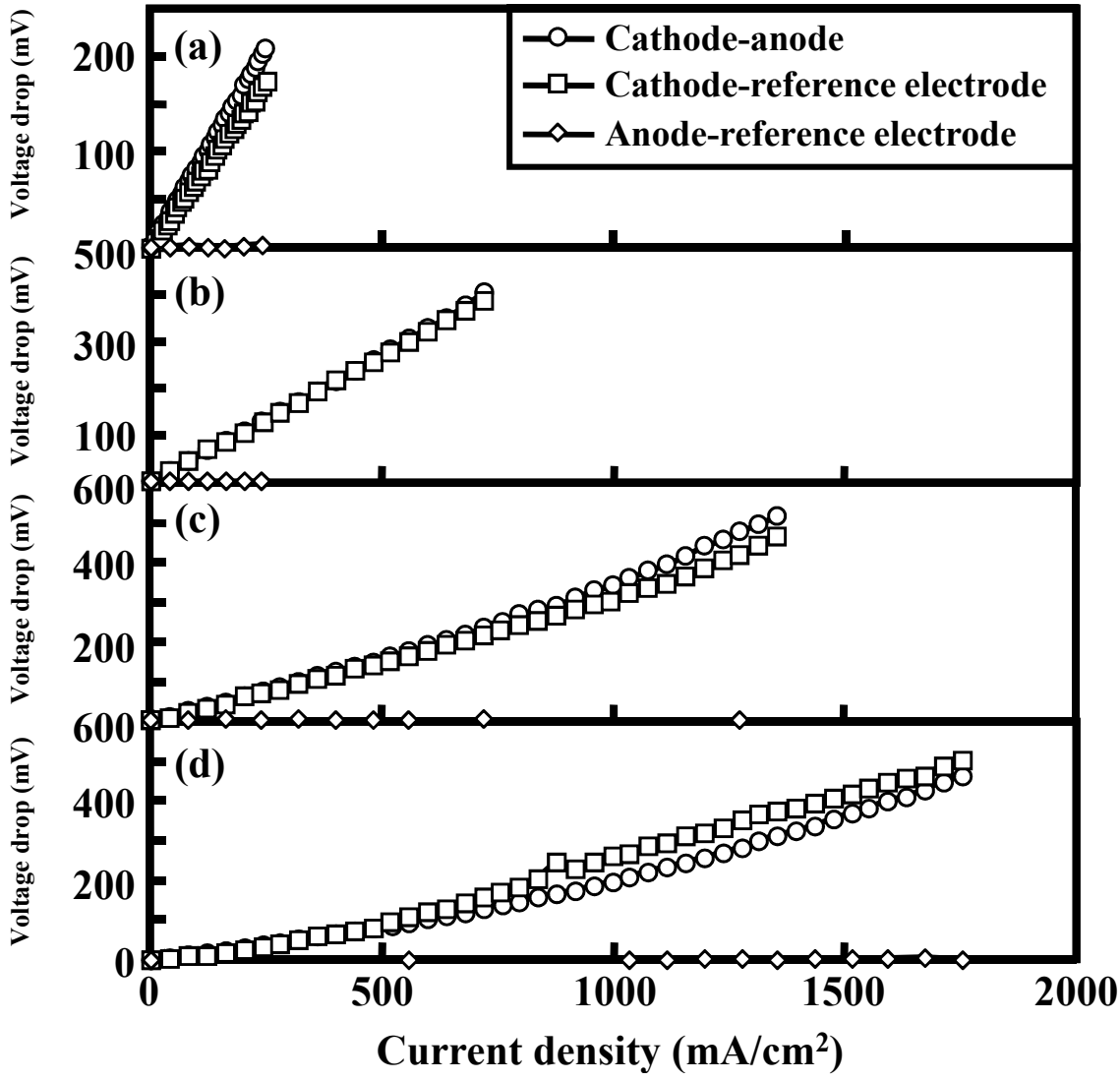

Fig. 4.8 Comparisons of voltage drops between cathode and anode, cathode and reference electrode, and anode and reference electrode at (a) 773, (b) 873, (c) 973 and (d) 1073 K.

Table 4.1 Voltage drops at cathode, electrolyte and anode for the cells with the $SrRuO_3$ cathode on the 600 μm thick GDC electrolyte (a) and on the anode-supported GDC electrolyte (b) under a direct current of 100 mA/cm^2 at 873 and 1073 K.

Temperature (K)	Cell	Voltage drop (mV)	
		cathode	electrolyte and anode
873	(a)	372.9	127.4
	(b)	54.7	0.2
1073	(a)	29.4	7.7
	(b)	10.0	0.2

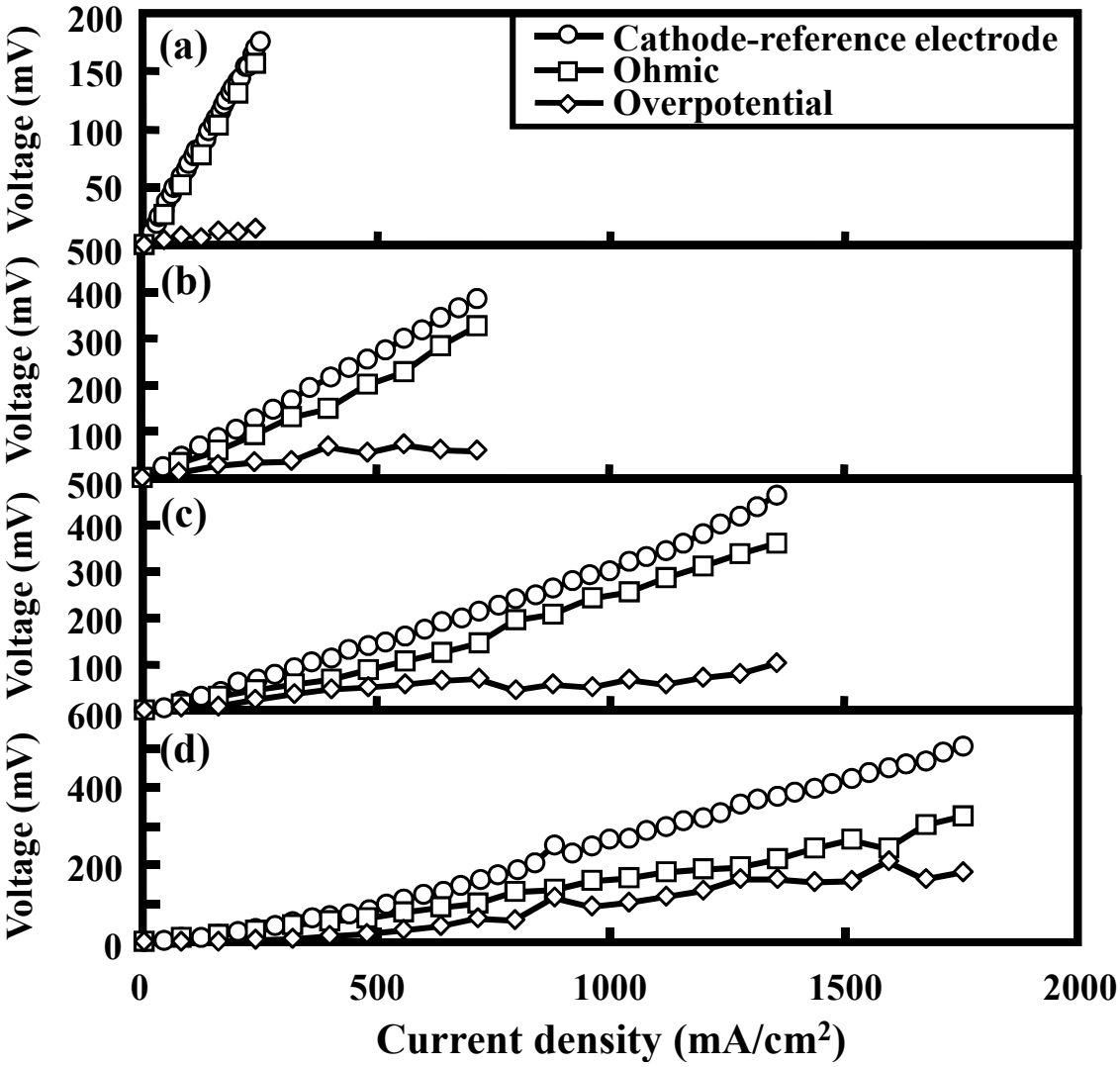

Fig. 4.9 Terminal voltage drop between cathode and reference electrode of the anode-supported SOFC with $SrRuO_3$ cathode and GDC electrolyte at (a) 773, (b) 873, (c) 973 and (d) 1073 K.

and 381 mW/cm^2 and 1154 mA/cm^2 at 1073 K. The voltage drop at the cathode was almost equal to the voltage drop of the whole cell. The voltage drop at the anode was negligible. The contribution of the overpotential to the voltage drop at the cathode increased with increasing temperature.

References

1) S. Sridhar and U. B. Pal, Powder Technology, 88, 173-178 (1996).

2) C. L. Curtis, D. T. Gawne and M. Priestnall, J. Mater. Sci., 29, 3102-3106 (1994).

3) J. Will, A. Mitterdorfer, C. Kleinlogel, D. Perednis and L. J. Gauckler, Solid State Ionics, 131, 79-96 (2000).

4) W. Huang, P. Shuk and M. Greenblatt, Solid State Ionics, 100, 23-27 (1997).

5) H. Sasaki, S. Otoshi, M. Suzuki, T. Sogi, A. Kajimura, N. Sugiura and M. Ippommatsu, Solid State Ionics, 72, 253-256 (1994).

6) S. Uchida, S. Sameshima and Y. Hirata, J. Ceram. Soc. Jpn., 109 [2], 100-105 (2001).

7) Mistler, R. E., Am. Ceram. Soc. Bull., 77, 82-86 (1998).

8) I. Riess, J. Electrochem. Soc., 128, 2077-2081 (1981).

9) S. Yuan and U. Pal, J. Electrochem. Soc., 143, 3214-3222 (1996).

10) S. Sameshima, Y. Hirata and Y. Ehira, J. Alloys Comp., 408-412, 628-631 (2006).

11) C. Xia and M. Liu, Solid State Ionics, 144, 249-255 (2001).

12) Y.J. Leng, S.H. Chan, S.P. Jiang and K.A. Khor, Solid State Ionics, 170, 9-15 (2004).

Chapter 5

AC Impedance Spectra of Cathodes Used in the Solid Oxide Fuel Cells

5.1 Introduction

The lower operation temperature of SOFC leads to a higher percentage of the voltage loss at the electrodes because of the higher activation energy of the reaction at the cathode[1]. In order to improve the electrochemical properties of the cathode for SOFC, the reaction mechanisms should be understood. The reduction of oxygen molecules at the cathode includes the diffusion of O_2 gas, the dissociative adsorption of O_2 on the cathode surface, the surface diffusion of O atom to the triple phase boundary of the electrolyte - cathode - O_2 gas and the diffusion of oxide ion into the electrolyte. The overall reaction at the cathode is expressed by Eq. (5.1),

$$O_2 + 2V_O^{\bullet\bullet} + 4e' \rightarrow 2O_O^{\times} \qquad (5.1)$$

The identifications of the reaction mechanisms on the metal electrodes were reported by the experimental investigations combined with modeling of the proposed reaction mechanisms[2)-4)]. The rate determining step and the reaction mechanism change with the morphology and the kind of the metal electrode. In this chapter, the reaction mechanism of O_2 molecules with electrons at the cathode for the SOFC measured in chapters 3 and 4 is discussed on the AC impedance spectra fitted with the equivalent circuits.

5.2 Experimental Procedure

Measurement of the Electrochemical Properties of the Cathode

The GDC electrolyte-supported cells with ITO, $SrRuO_3$ or Co_2RuO_4 cathode and Ni-GDC anode, and the Ni-GDC anode-supported cell with $SrRuO_3$ cathode and GDC electrolyte were fabricated and then Pt reference electrode was fixed on the GDC surface with Pt paste. The cell performances were measured by feeding air and 3 vol% H_2O-containing H_2 fuel into cathode and anode at 100 ml/min, respectively. A direct current-voltage relation and AC impedance in the frequency range from 0.01 Hz to 100 kHz at the current of 10 mA were measured in the temperature range from 773 to 1073 K (As-510, NF Kairosekkei Block Co., Japan).

5.3 Results and Discussion

5.3.1 AC Impedance Spectra Measured for ITO and $SrRuO_3$ Cathodes

Figures 5.1 (a) and 5.2 (a) show the AC impedance spectra measured between the ITO cathode and the Pt reference electrode at 873 K under open circuit and at direct current of 12 mA, respectively. The data of Figs. 5.1 and 5.2 were fitted with the equivalent circuits shown in Figs. 5.1 (b) and 5.2 (b), respectively. The AC impedance spectrum under open circuit consisted of one capacitive loop. On the other hand, the additional capacitive loop appeared at the low frequency region of the AC impedance spectrum at direct current of 12 mA. This second loop at a low frequency region became larger with increasing direct current. The similar trends were observed for the $SrRuO_3$ cathode as shown in Figs. 5.3 and 5.4. Figures 5.3 (a) and 5.4 (a) show the AC impedance spectra measured between the $SrRuO_3$ cathode and the Pt reference electrode at 1073 K under open circuit and at direct current of 130 mA, respectively. These data were fitted with the equivalent circuits shown in Figs. 5.3 (b) and 5.4 (b), respectively. These results indicate that the additional elementary process occurs for the cathode at a high direct current. The charge transfer reaction occurs at the triple phase boundary since the oxide ion conductivities of ITO and $SrRuO_3$ have not been reported. The oxide ions formed at the triple phase boundary diffuse into the electrolyte. In the low direct current, the oxide ions diffuse into the electrolyte near the triple phase boundary, which process is reflected in the high frequency capacitive loop (Fig. 5.5). It was reported that the diffusion process of oxide ion from the surface of GDC electrolyte appears in the frequency region below 100 kHz[5]. As the direct current increases, the oxide ions spread on the electrolyte surface and diffuse into the electrolyte since the flux of oxide ions concentrates on the triple phase boundary. This process is shown as the low frequency capacitive loop. Figure 5.5 illustrates the reaction mechanism of O_2 molecules with electrons at the ITO and $SrRuO_3$ cathode. As shown in Figs. 5.1 - 5.4, the AC impedance spectra were fitted with the equivalent circuits consisting of an ohmic resistance (R1) and one or two resistance-capacitance parallel circuits ([R2C2] or [R2C2][R3C3], C2 < C3). Figures 5.6 and 5.7 show the resistance (a) and the

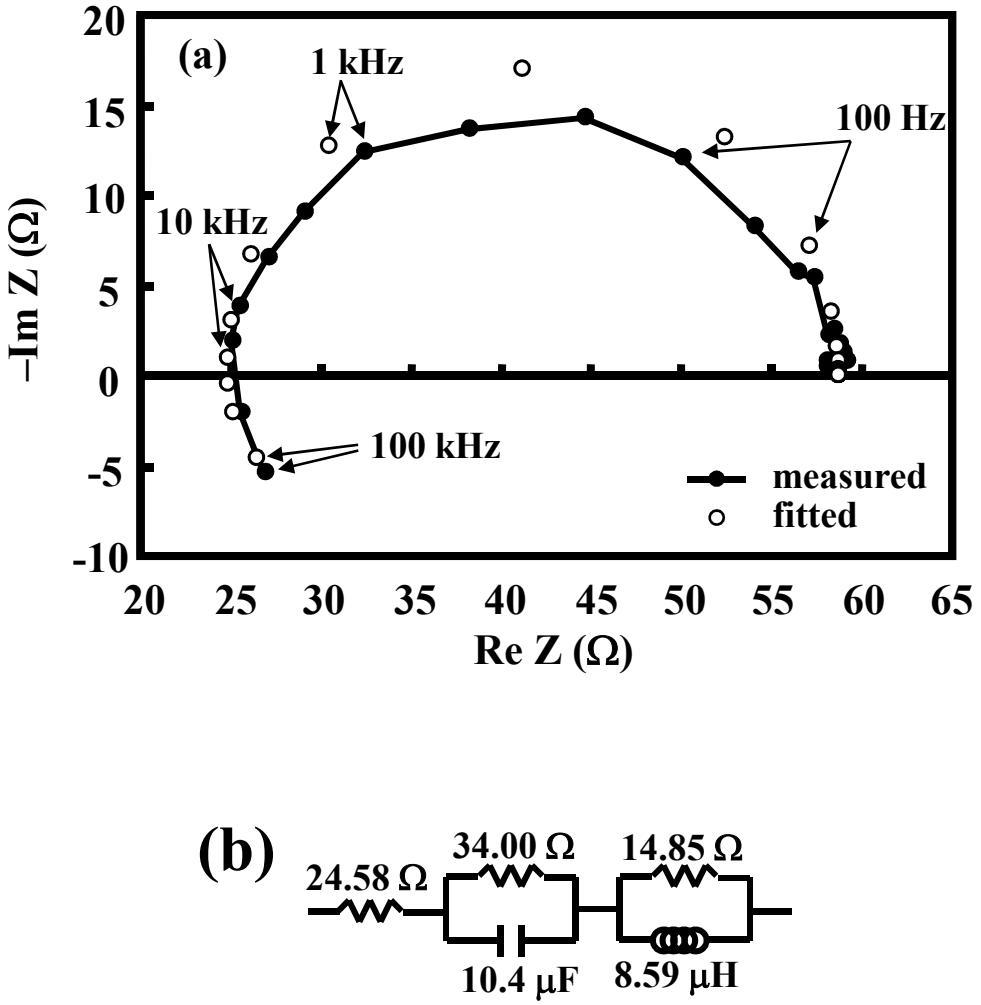

Fig. 5.1 AC impedance spectrum (a) between cathode and reference electrode of the cell with ITO cathode measured at 873 K under open-circuit and corresponding equivalent circuit (b).

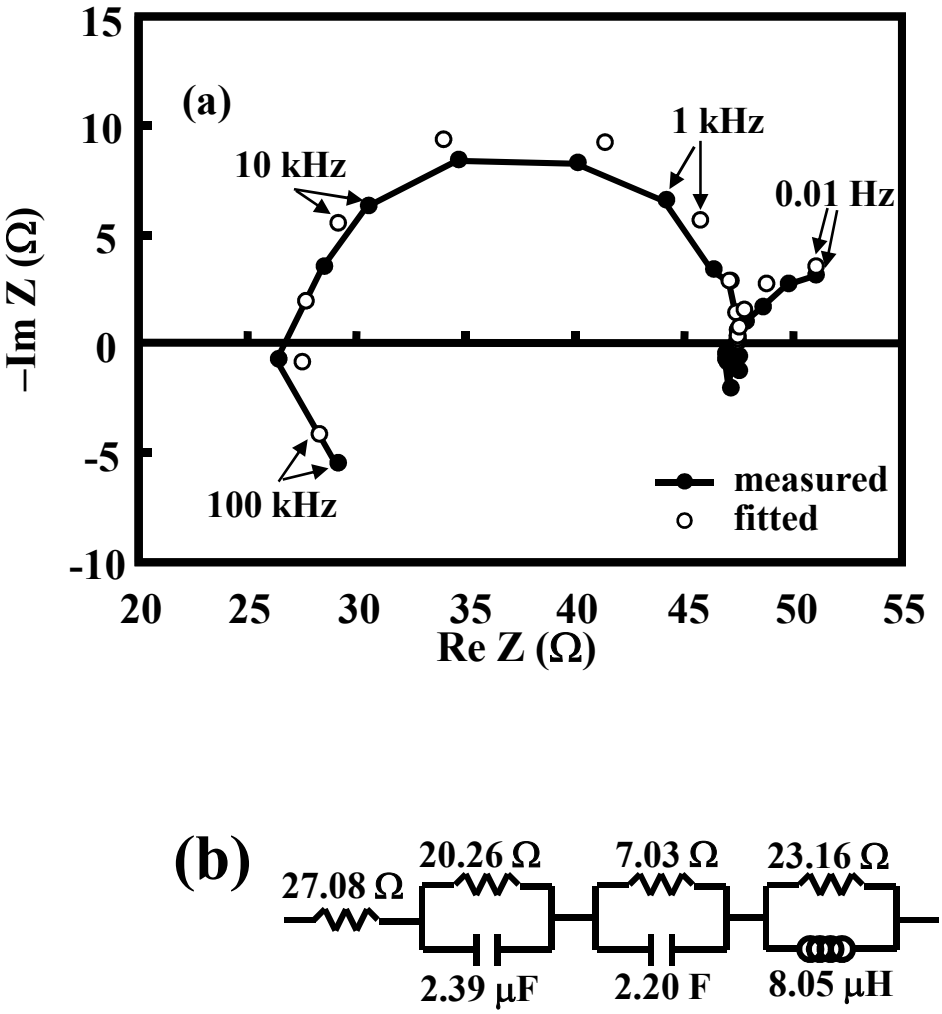

Fig. 5.2 AC impedance spectrum (a) between cathode and reference electrode of the cell with ITO cathode measured at 873 K at direct current of 12 mA and corresponding equivalent circuit (b).

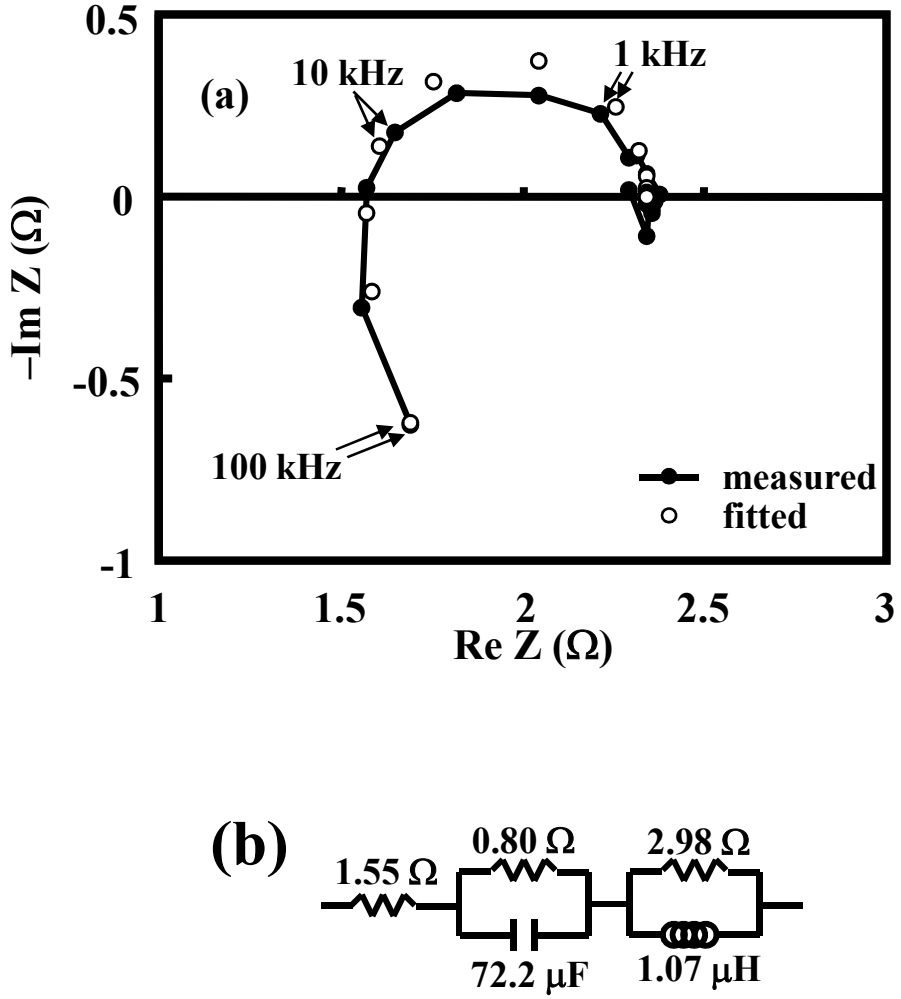

Fig. 5.3 AC impedance spectrum (a) between cathode and reference electrode of the cell with $SrRuO_3$ cathode measured at 1073 K under open-circuit and corresponding equivalent circuit (b).

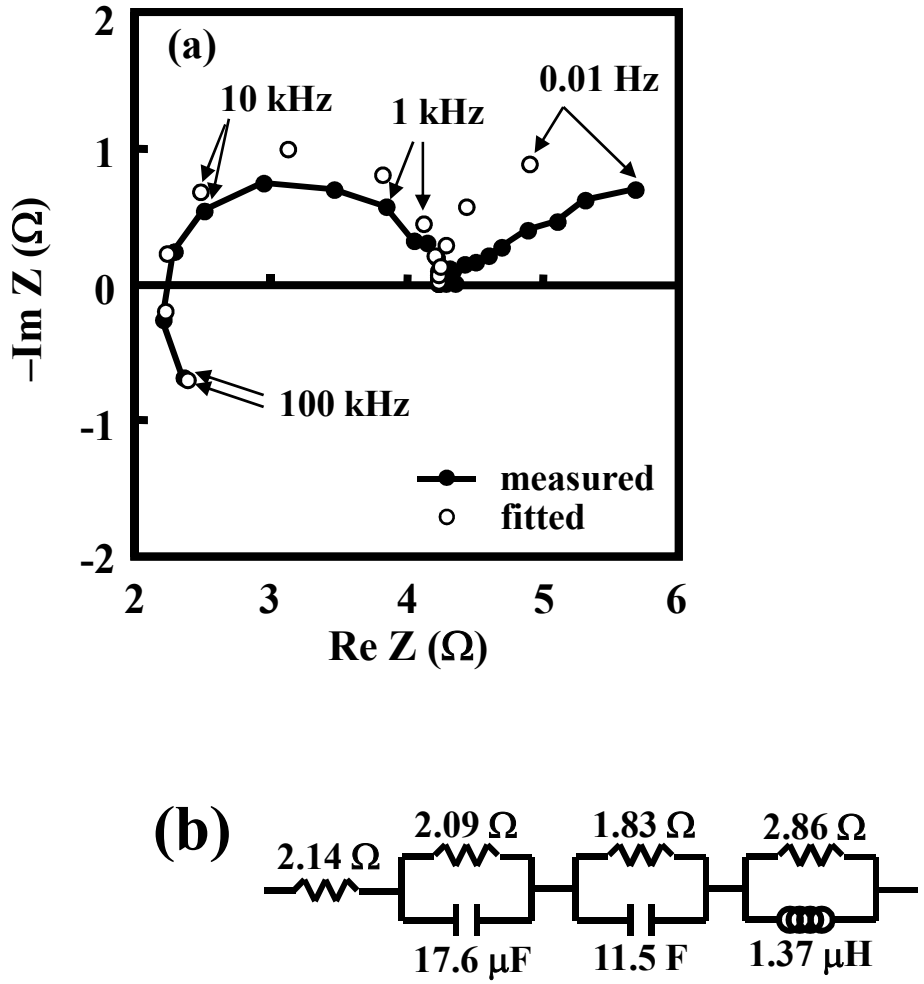

Fig. 5.4 AC impedance spectrum (a) between cathode and reference electrode of the cell with $SrRuO_3$ cathode measured at 1073 K at direct current of 130 mA and corresponding equivalent circuit (b).

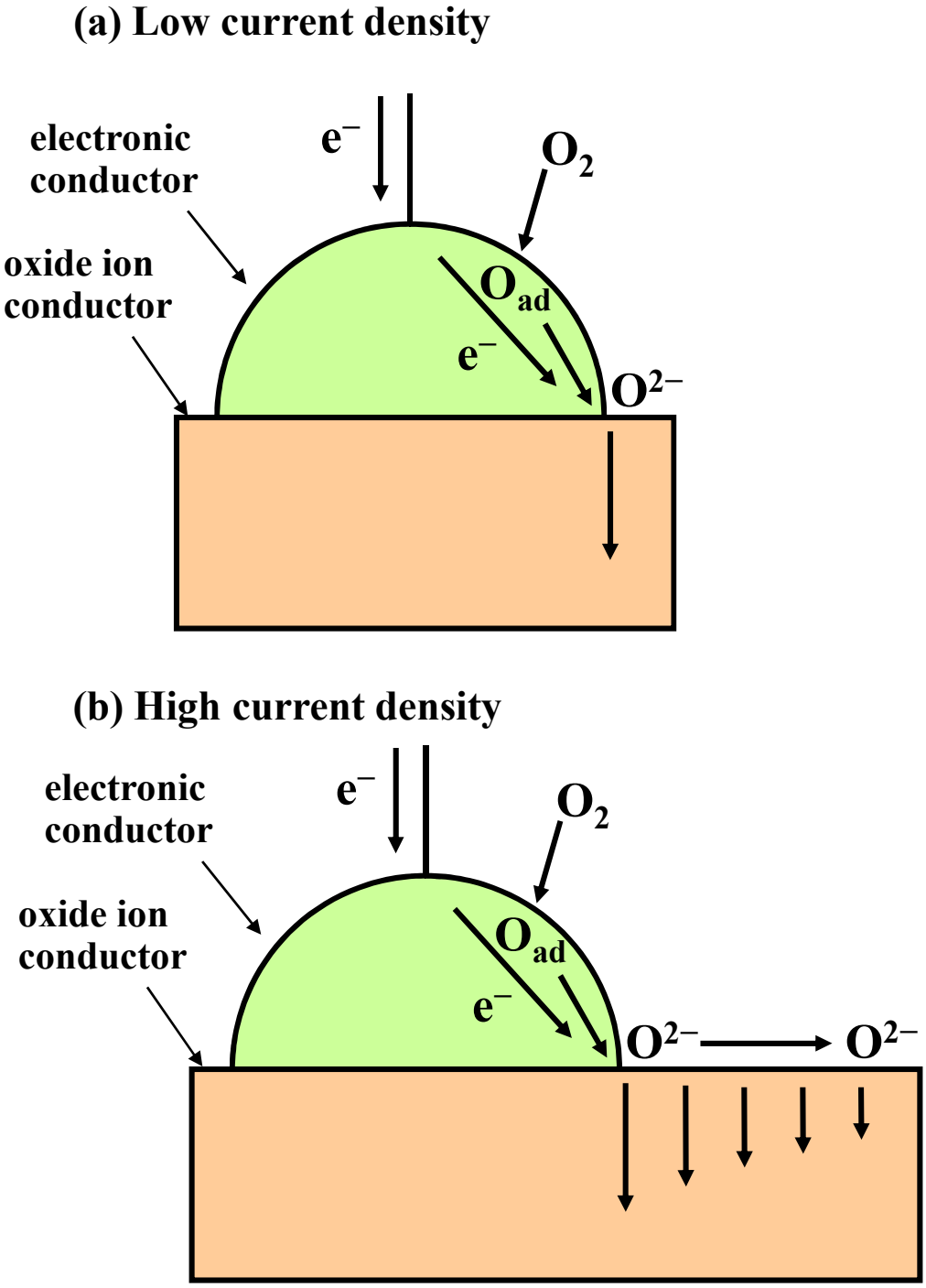

Fig. 5.5 Mechanisms of cathode reactions at (a) low and (b) high current density for ITO or $SrRuO_3$ cathode.

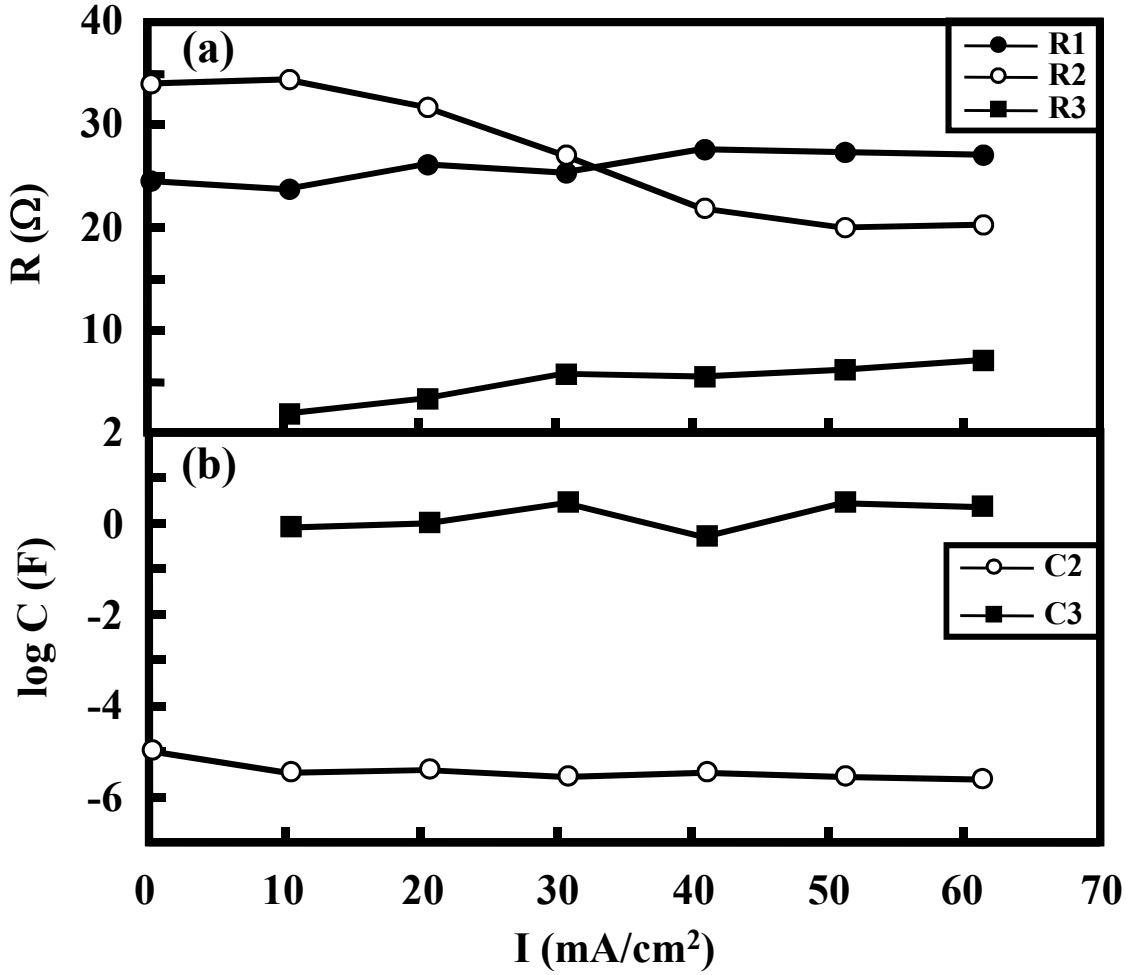

Fig. 5.6 Resistance (a) and capacitance (b) obtained from AC impedance spectra measured for the ITO cathode at 873 K.

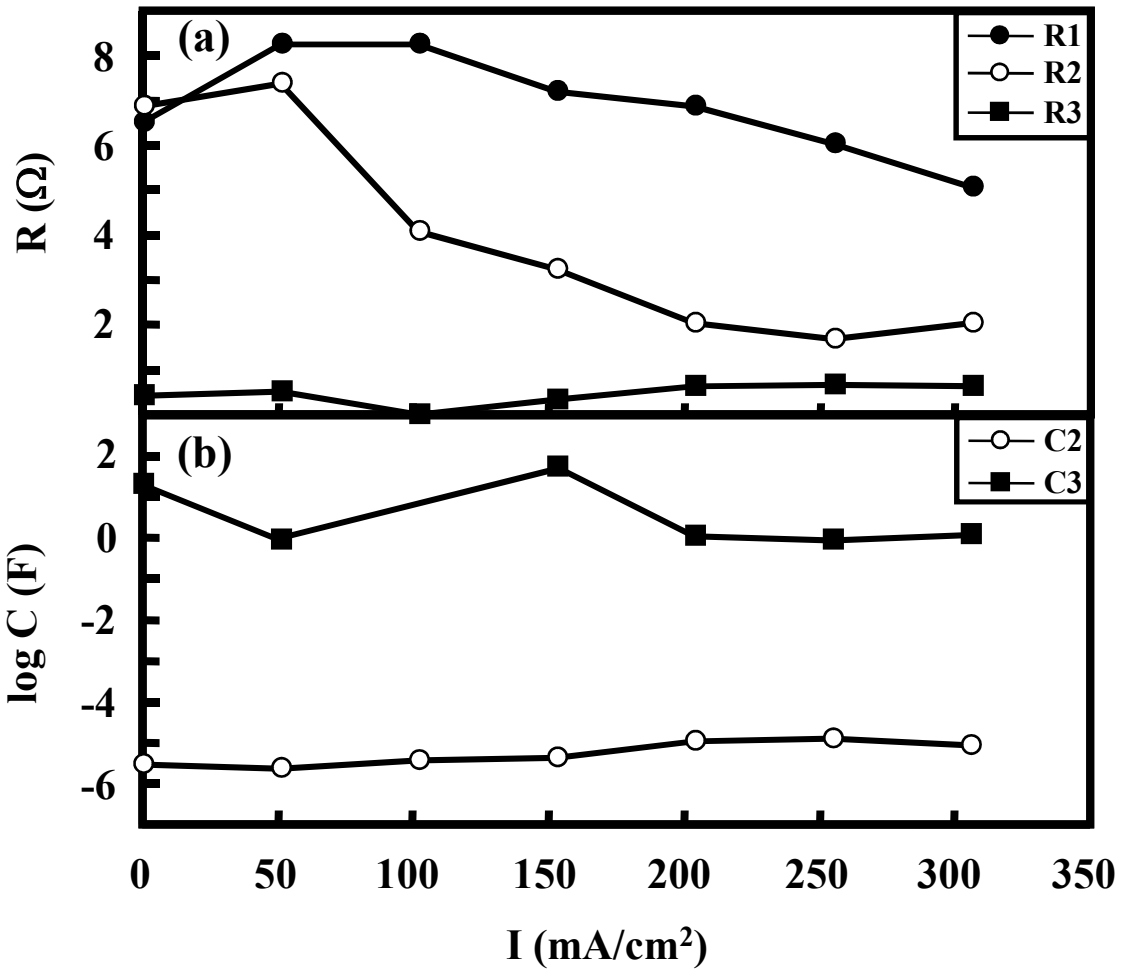

Fig. 5.7 Resistance (a) and capacitance (b) obtained from AC impedance spectra measured for the ITO cathode at 1073 K.

capacitance (b) obtained from the AC impedance spectra measured for the ITO cathode at 873 and 1073 K, respectively, as a function of current density. Figures 5.8 and 5.9 show the resistance (a) and the capacitance (b) obtained for the $SrRuO_3$ cathode at 873 and 1073 K, respectively. R1 value for ITO or $SrRuO_3$ cathode was almost constant and was independent of the current density. This result may indicate that the R1 value corresponds to the intrinsic resistance of the cathode. The reported electrical conductivities of ITO and $SrRuO_3$ are 5.0×10^2 and 1.0×10^4 S/cm at 300 K, respectively[6), 7)]. These values were higher than the conductivities of present ITO and $SrRuO_3$ cathode by a factor of 10^5 and 10^6, respectively. This result may be due to the porous structure of ITO and $SrRuO_3$ cathode. The poor connection between the adjacent particles in the cathode decreases the electrical conductivity. R2 value of the ITO cathode decreased with increasing current density, while the R3 value of the ITO cathode was almost constant with current density at both the temperatures. The current density dependences of the R2 and R3 values of the $SrRuO_3$ cathode at 873 K were similar to those of the ITO cathode. On the other hand, the R2 value of the $SrRuO_3$ cathode at 1073 K increased with increasing current density. The variation of R2 and R3 values is discussed on the reaction mechanism of O_2 molecules with electrons in Fig. 5.5 under the assumption that the R2 and R3 values reflect the transfer of the charge to adsorbed O atoms and that the rate of the surface diffusion of oxide ions on the GDC electrolyte is significantly faster than that of the diffusion of oxide ions into the GDC electrolyte. Then, the R2 and R3 values reflect the diffusions of oxide ions into the electrolyte from the triple phase boundary and from the electrolyte surface, respectively. The R2 and R3 values may be affected by the concentration of the oxide ions on the triple phase boundary and the electrolyte surface, respectively, and the concentration of the oxygen vacancy on the electrolyte surface near and far from the triple phase boundary, respectively. While the decrease of the concentration of carrier and the increase of diffusion length lead to the increase of resistance. The C2 and C3 values showed $10^{-6} - 10^{-4}$ and $10^{-1} - 10^2$ F, respectively, and were independent of the current density. According to the reaction mechanism of O_2 molecules with electrons shown in Fig. 5.5, the parallel circuits described by [R2C2] and [R3C3] reflect the reactions on

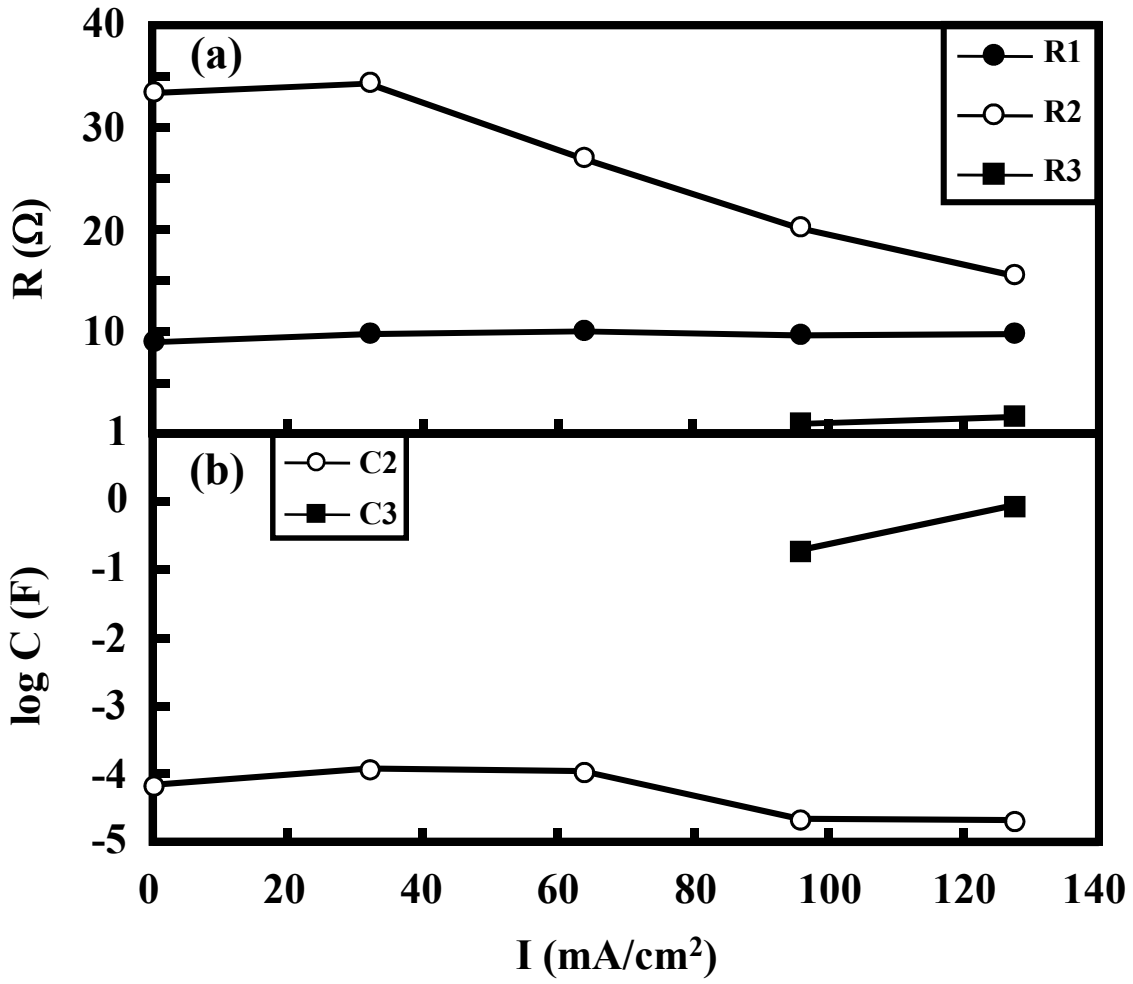

Fig. 5.8 Resistance (a) and capacitance (b) obtained from AC impedance spectra measured for the $SrRuO_3$ cathode at 873 K.

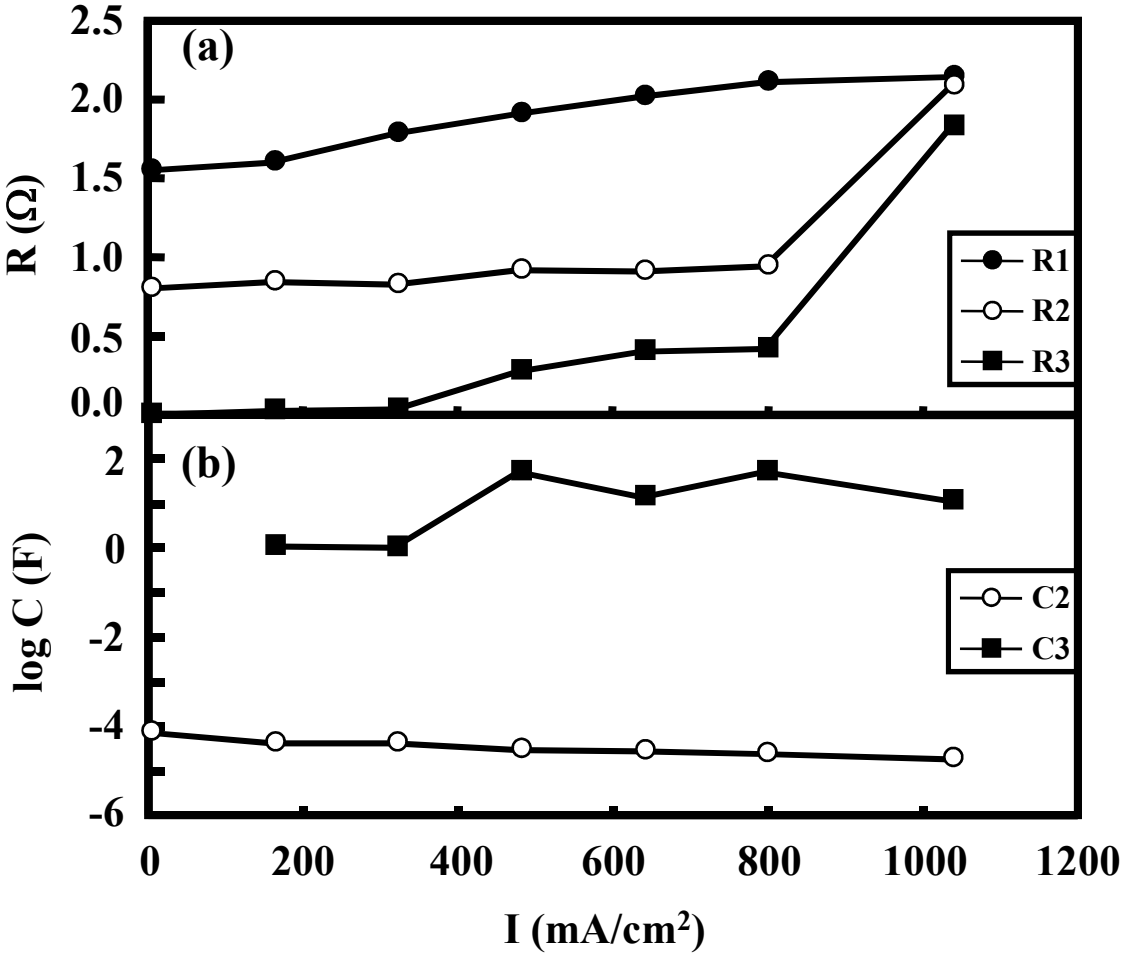

Fig. 5.9 Resistance (a) and capacitance (b) obtained from AC impedance spectra measured for the $SrRuO_3$ cathode at 1073 K.

the triple phase boundary and on the electrolyte surface, respectively. The C3 value larger than the C2 value may be attributed to the larger area of the electrolyte surface as compared with that of the triple phase boundary. The increase of the concentration of the oxygen vacancy on the electrolyte surface (i.e. decrease of diffusion length of carrier) far from the triple phase boundary lead to the decrease of R2 value.

5.3.2 AC Impedance Spectra Measured for Co_2RuO_4 and $SrRuO_3$ on 30 μm GDC Electrolyte

The AC impedance spectra for the Co_2RuO_4 cathode on the 550 μm thick GDC electrolyte and the $SrRuO_3$ cathode on the anode-supported GDC electrolyte were different from those described above. A inductive loop appeared in the low frequency region. Figures 5.10 (a) and 5.11 (a) show the AC impedance spectra measured between the Co_2RuO_4 cathode and the Pt reference electrode at 1073 K under open circuit and at direct current of 110 mA, respectively. These data were fitted with the equivalent circuits shown in Figs. 5.10 (b) and 5.11 (b), respectively. The inductive loop in the low frequency region became smaller with increasing direct current. This trend was also observed in the AC impedance spectra for the $SrRuO_3$ cathode on the anode-supported GDC electrolyte. Figures 5.12 (a) and 5.13 (a) show the AC impedance spectra measured between the $SrRuO_3$ cathode and the Pt reference electrode on the anode-supported GDC electrolyte at 973 K under open circuit and at direct current of 170 mA, respectively. These data were fitted with the equivalent circuits shown in Figs. 5.12 (b) and 5.13 (b), respectively. The appearance of the inductive loop in the low frequency region may be due to the electronic current in the GDC electrolyte. When the Co_2RuO_4 cathode was used in the SOFC, $Gd_2Ru_2O_7$ formed on the GDC electrolyte surface, enhancing the electronic conductivity of the electrolyte as described in chapter 3. Also, for the anode-supported SOFC, the internal short circuit current becomes larger owing to the thinner electrolyte as expressed by Eq. (4.12). Both the formation of $Gd_2Ru_2O_7$ and the decrease of the electrolyte thickness lead to the increased electronic current in the GDC electrolyte. On the other hand, the electronic current in the electrolyte decreases when the current flows through the external circuit. The external current density (I_{ext}) is expressed by Eq. (5.2),

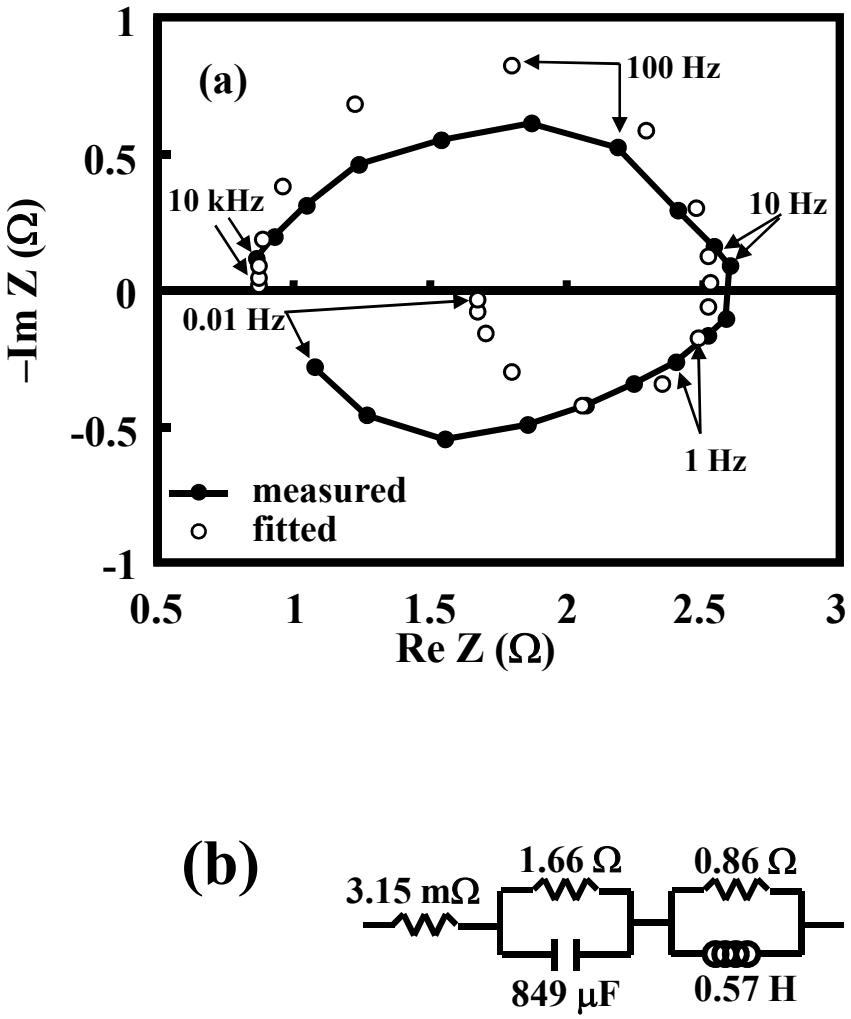

Fig. 5.10 AC impedance spectrum (a) between cathode and reference electrode of the cell with Co_2RuO_4 cathode measured at 1073 K under open-circuit and corresponding equivalent circuit (b).

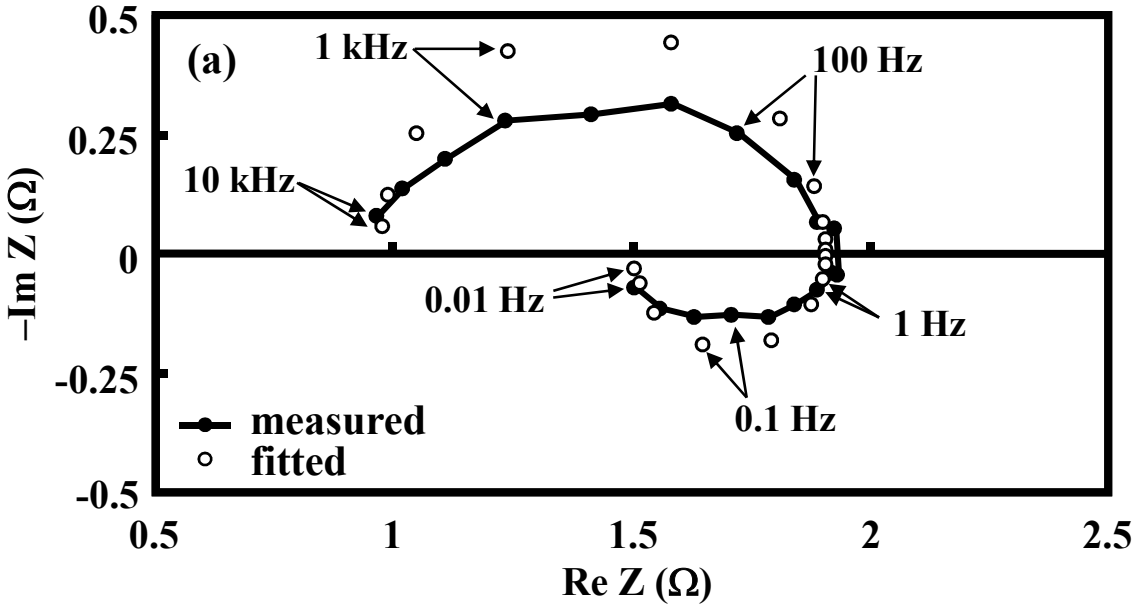

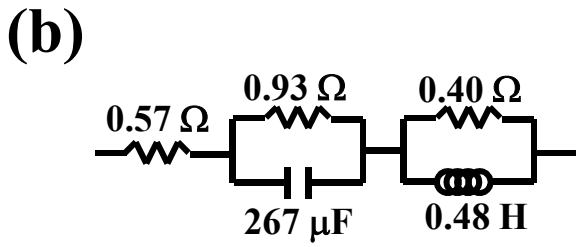

Fig. 5.11 AC impedance spectrum (a) between cathode and reference electrode of the cell with Co_2RuO_4 cathode measured at 1073 K at direct current of 110 mA and corresponding equivalent circuit (b).

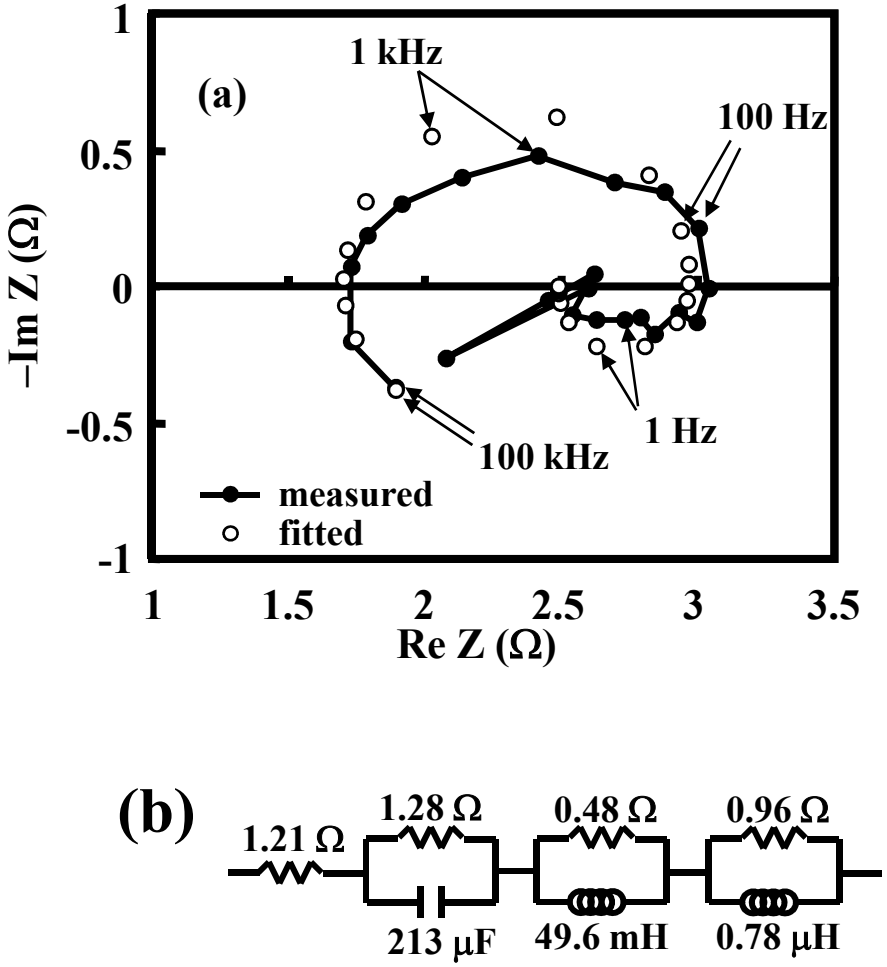

Fig. 5.12 AC impedance spectrum (a) between cathode and reference electrode of the anode-supported cell with $SrRuO_3$ cathode measured at 973 K under open-circuit and corresponding equivalent circuit (b).

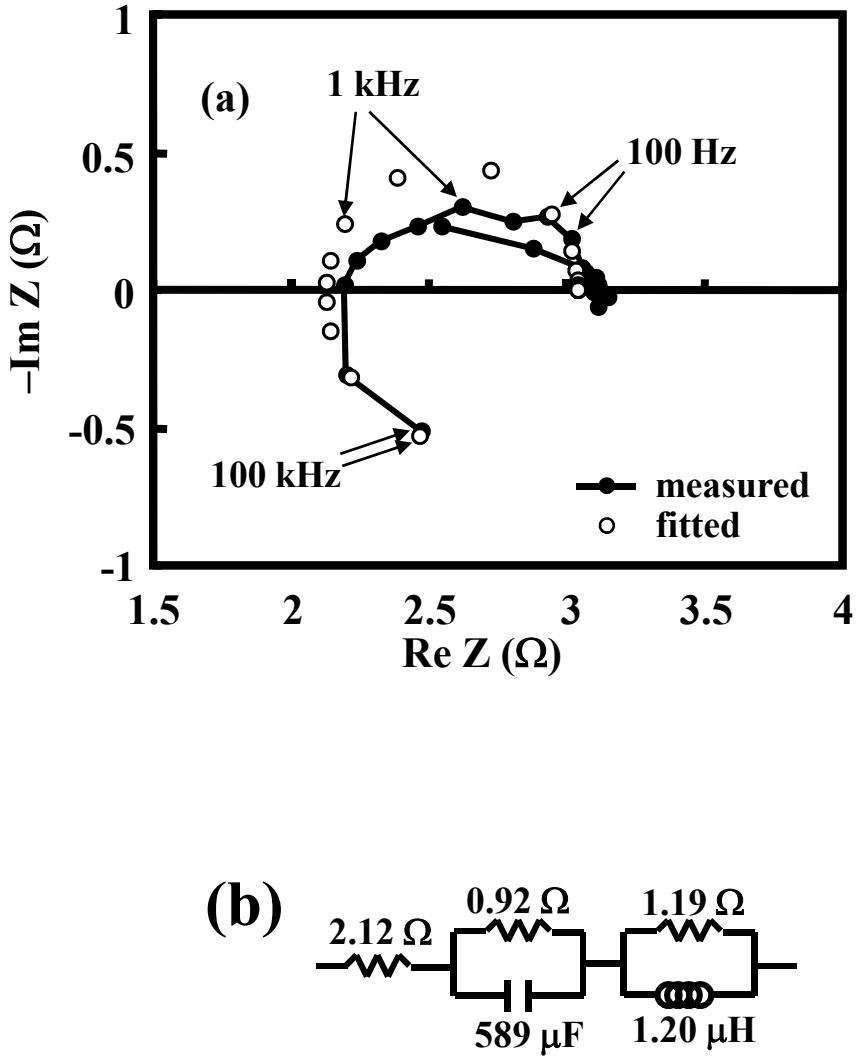

Fig. 5.13 AC impedance spectrum (a) between cathode and reference electrode of the anode-supported cell with $SrRuO_3$ cathode measured at 973 K at direct current of 170 mA and corresponding equivalent circuit (b).

$$I_{ext} = I_{O^{2-}} + I_e \tag{5.2}$$

Equation (5.3) is obtained by eliminating $\frac{\partial \eta_e}{\partial x}$ from Eqs. (4.1) and (4.2),

$$\frac{I_{O^{2-}}}{\sigma_{O^{2-}}} - \frac{I_e}{\sigma_e} = \frac{1}{2F}\frac{\partial \mu_O}{\partial x} \tag{5.3}$$

The substitution of Eq. (4.3) into Eq. (5.3) gives Eq. (5.4),

$$\frac{I_{O^{2-}}}{\sigma_{O^{2-}}} - \frac{I_e}{\sigma_e} = \frac{RT}{4F}\frac{\partial \ln P_{O_2}}{\partial x} \tag{5.4}$$

The Eq. (5.5) is obtained by integrating Eq. (5.4),

$$I_{O^{2-}} = \frac{nRT\sigma_{O^{2-}}}{4FL}\ln\left[\frac{\sigma_{O^{2-}} - rCP_{O_2}(0)^{-1/n}}{\sigma_{O^{2-}} - rCP_{O_2}(L)^{-1/n}}\right] \tag{5.5}$$

where r is the ratio of $I_{O^{2-}} / I_e$[8], L is the thickness of the electrolyte, and $P_{O_2}(0)$ and $P_{O_2}(L)$ is the oxygen partial pressures at x = 0 and x = L, respectively. In the open circuit condition (r = −1), Eq. (5.5) is equal to Eq. (4.12). The I_{ext} value is expressed as a function of the r value by Eq. (5.6),

$$\begin{aligned} I_{ext} &= \left(1 + \frac{1}{r}\right) I_{O^{2-}} \\ &= \left(1 + \frac{1}{r}\right)\frac{nRT\sigma_{O^{2-}}}{4FL}\ln\left[\frac{\sigma_{O^{2-}} - rCP_{O_2}(0)^{-1/n}}{\sigma_{O^{2-}} - rCP_{O_2}(L)^{-1/n}}\right] \end{aligned} \tag{5.6}$$

Under the operation condition of SOFC, the r value is smaller than −1. The minus sign is due to the opposite flows of the oxide ions and the electrons. The simulation of Eq. (5.6) as a function of r value indicates that the I_{ext} value increases with decreasing r value, while the absolute value of I_e decreases with decreasing r value. Figure 5.14 shows the $I_{O^{2-}}$ and I_e values as a function of I_{ext}, which were calculated for 500 μm thick GDC electrolyte under a condition of T = 1073 K, $P_{O_2}(0)$ = 2.1 × 10^4 Pa, $P_{O_2}(L)$ = 1.0 × 10^{-17} Pa, $\sigma_{O^{2-}}$ = 1.25 × 10^{-1} S/cm, n = 5.79 and C = 2.58 × 10^{-5} S/cm. The $I_{O^{2-}}$ value approaches the I_{ext} value with increasing I_{ext} value, while the absolute value of I_e decreases with increasing I_{ext} value. The trend that the inductive loop became smaller with increasing external current reflects the trend that the electronic current passing through the electrolyte decreases with increasing external current. The electrons

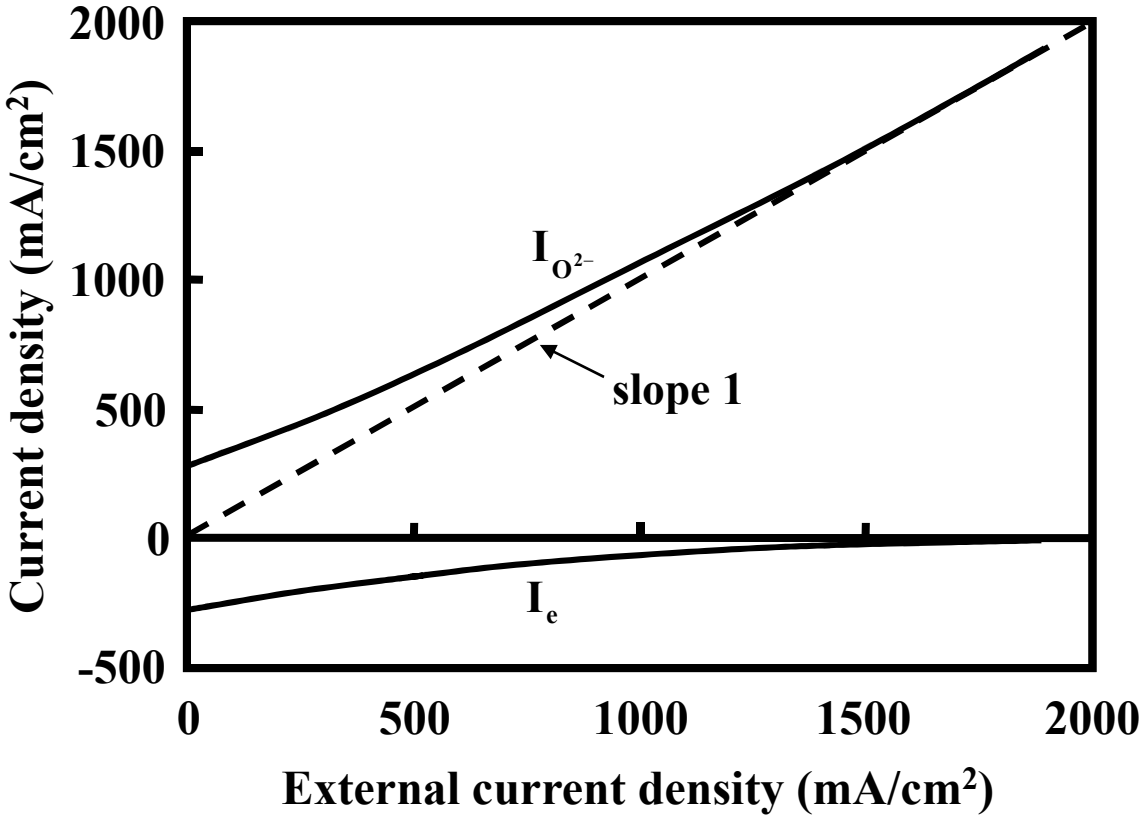

Fig. 5.14 Comparison of the absolute values of the oxide ion current and electronic current passing through GDC electrolyte as a function of external current density.

supplied from the anode to the cathode through the electrolyte may react with the oxygen adsorbed on the electrolyte surface. The inductive loop may reflect the reduction of oxygen atoms on the electrolyte surface and the diffusion of the formed oxide ions into the electrolyte (Fig. 5.15). Schouler et al.[9] observed the inductive loop similar to this study for the Pt electrode on the YSZ electrolyte under the anode polarization and reported that the appearance of the inductive loop can be attributed to the onset of a mixed conductivity in the electrolyte due to the direct injection of electron holes in the YSZ. On the other hand, Van Hassel et al.[3] suggested that the inductive loop observed in the O_2, Au/YSZ interface can be interpreted by a model involving a multi-step oxygen reduction and several adsorbed intermediates. The external current dependency of inductive loop observed in this study is different from their model. On the other hand, the AC impedance spectra measured between Pt cathode and Pt reference electrode on the anode-supported YSZ electrolyte (40 μm thickness) did not include the inductive loop in the low frequency region, and was composed of two capacitive loops, which were similar to the AC impedance spectra at ITO and $SrRuO_3$ cathode on the thicker GDC electrolyte (about 600 μm), as shown in Figs. 5.16 and 5.17. Figures 5.16 and 5.17 show the AC impedance spectra measured at Pt cathode on the anode-supported YSZ electrolyte at 1073 K under open circuit and at direct current of 12 mA, respectively. This result supports the influence of the electronic current in the GDC electrolyte on the inductive loop because the electronic current in the YSZ electrolyte thin film is significantly low.

The AC impedance spectra for the Co_2RuO_4 cathode on the 550 μm thick GDC electrolyte and the $SrRuO_3$ cathode on the anode-supported GDC electrolyte were fitted with the equivalent circuits consisting of an ohmic resistance (R1) and one or two resistance-capacitance parallel circuits ([R2C2] or [R2C2][R3C3], C2 < C3). Figures 5.18 and 5.19 show the resistance (a) and the capacitance (b) obtained for the Co_2RuO_4 at 873 and 1073 K, respectively, as a function of current density. The R1 value for the Co_2RuO_4 cathode at 873 K was almost independent of the current density, while the R1 value at 1073 K increased with increasing current density above a direct current of 400 mA/cm^2. The variation of R1 value has not been understood. The R2 values of the

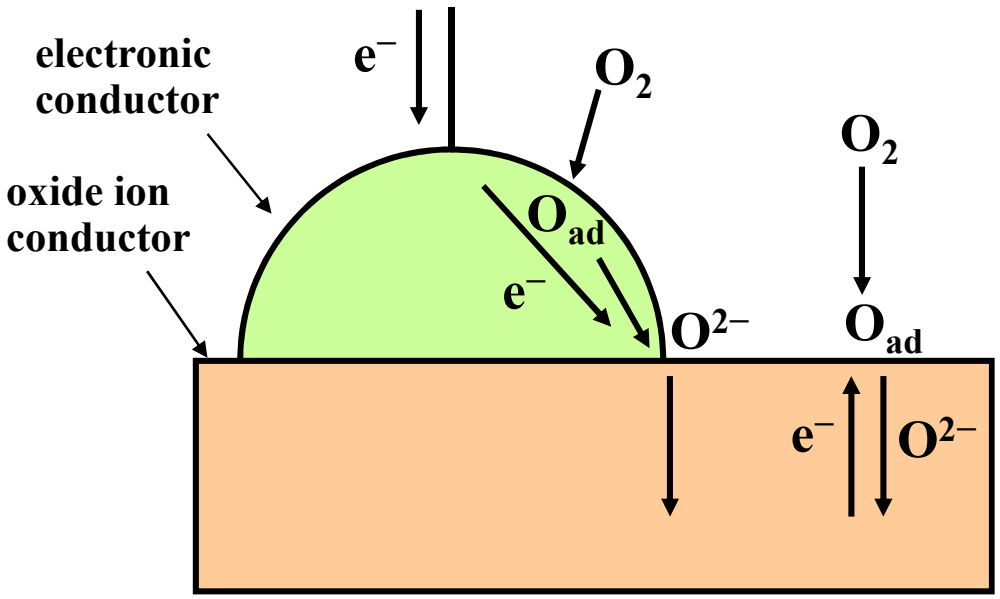

Fig. 5.15 Mechanisms of cathode reactions for Co_2RuO_4 cathode on the 550 μm thick GDC electrolyte or $SrRuO_3$ cathode on the anode-supported GDC electrolyte.

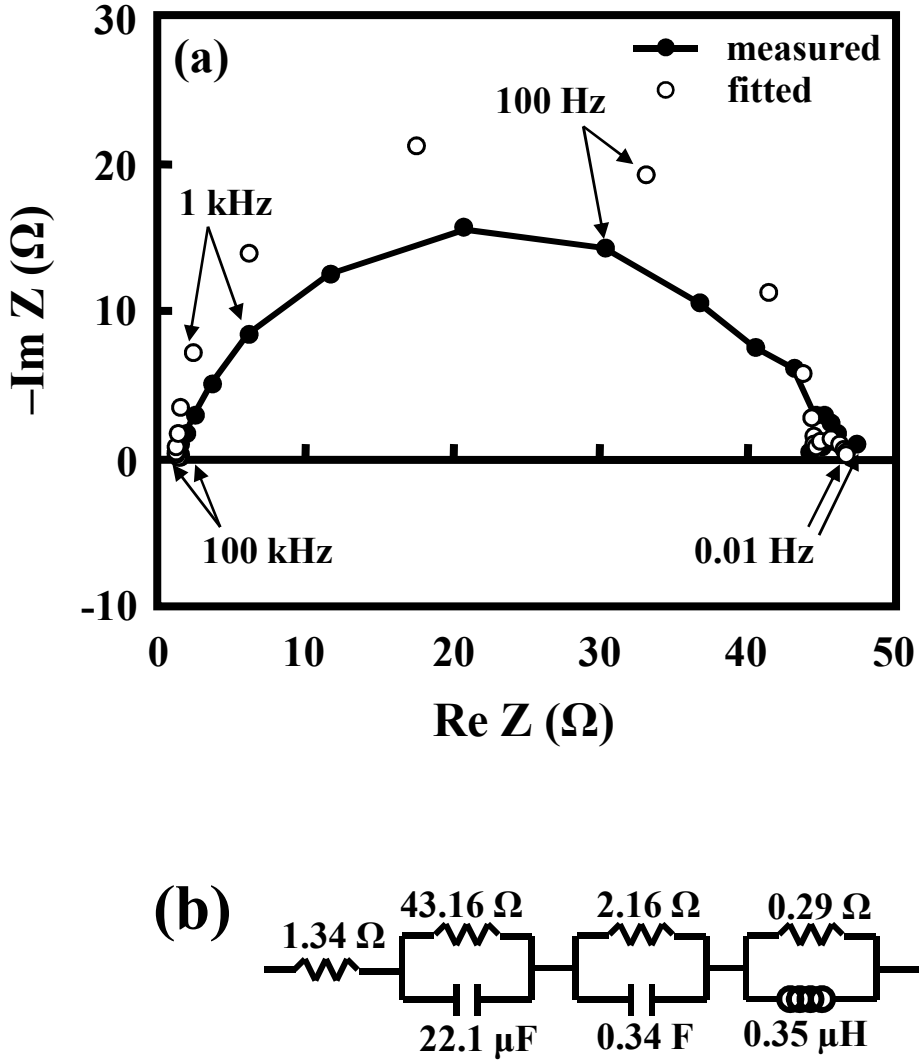

Fig. 5.16 AC impedance spectrum (a) measured at Pt cathode on the anode-supported YSZ electrolyte thin film at 1073 K under open-circuit and corresponding equivalent circuit (b).

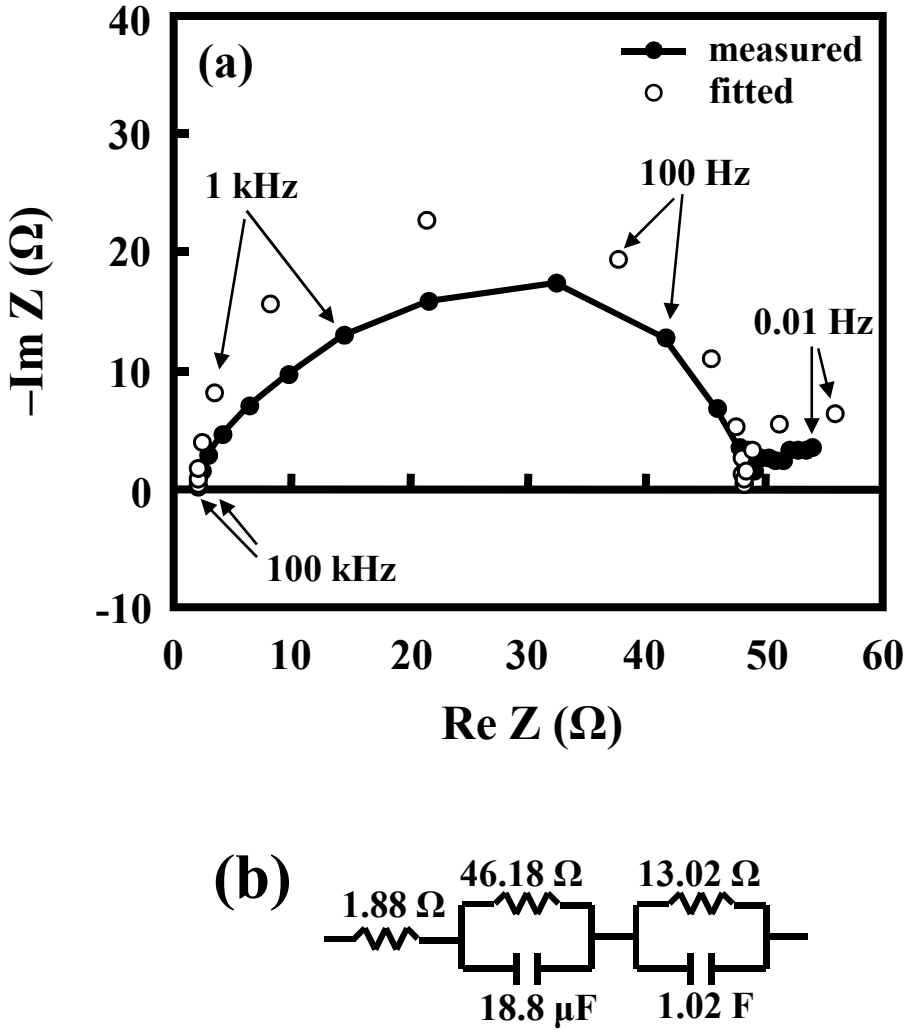

Fig. 5.17 AC impedance spectrum (a) measured at Pt cathode on the anode-supported YSZ electrolyte thin film at 1073 K at direct current of 12 mA and corresponding equivalent circuit (b).

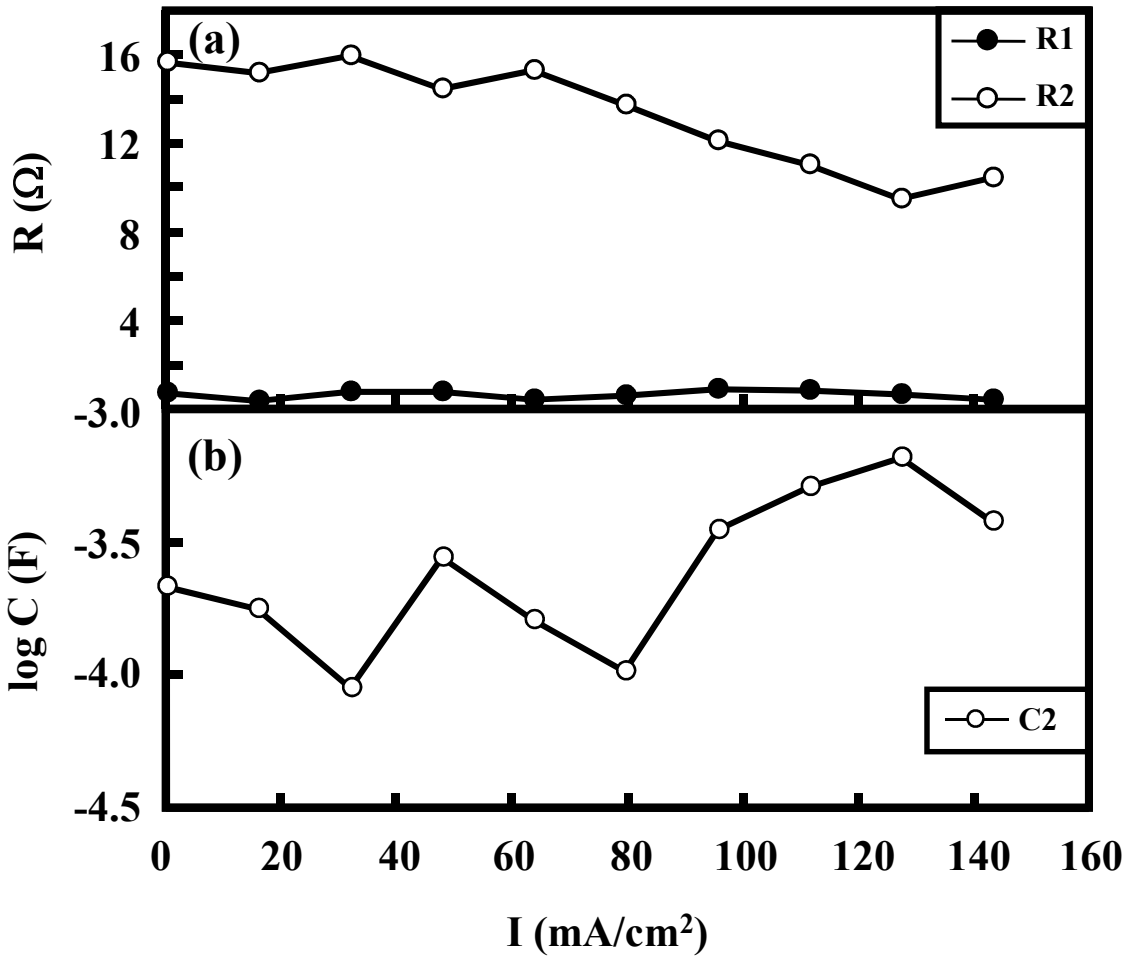

Fig. 5.18 Resistance (a) and capacitance (b) obtained from AC impedance spectra measured for the Co_2RuO_4 cathode at 873 K.

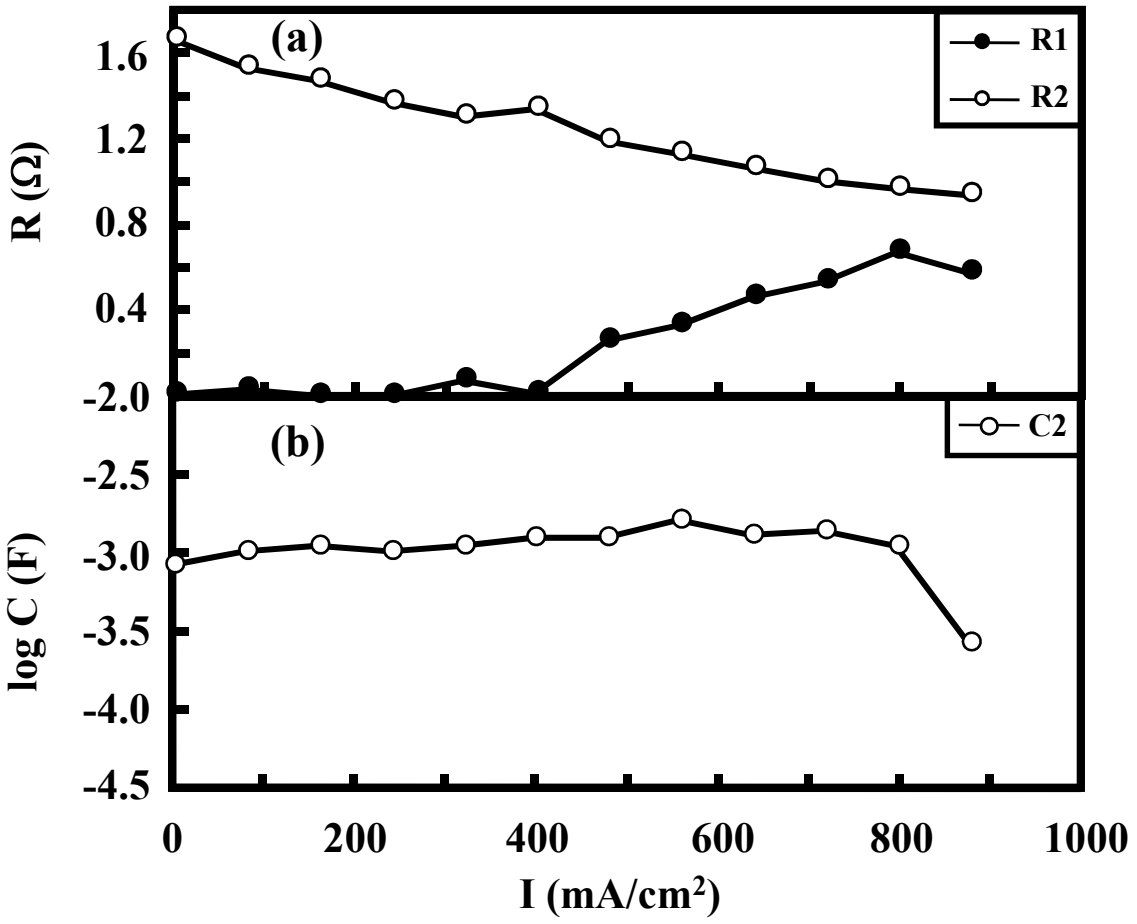

Fig. 5.19 Resistance (a) and capacitance (b) obtained from AC impedance spectra measured for the Co_2RuO_4 cathode at 1073 K.

Co_2RuO_4 cathode decreased with increasing current density at both the temperatures. The equivalent circuits for the Co_2RuO_4 cathode did not include [R3C3] parallel circuit. According to the reaction mechanism of O_2 molecules with electrons shown in Fig. 5.15, [R2C2] parallel circuit reflects the diffusion of oxide ions into the electrolyte near the triple phase boundary. The R2 value for the Co_2RuO_4 cathode may be affected by the concentration of the oxide ions on the triple phase boundary and the concentration of the oxygen vacancy on the electrolyte surface near the triple phase boundary. Figures 5.20, 5.21, 5.22 and 5.23 show the resistance (a) and the capacitance (b) obtained for the $SrRuO_3$ cathode on the anode-supported GDC electrolyte at 773, 873, 973 and 1073 K, respectively. The R1 values for the $SrRuO_3$ cathode on the anode-supported GDC electrolyte at 773 and 873 K were almost independent of the current density, while the R1 values at 973 and 1073 K increased with increasing current density. The variation of R1 value has not been understood. The R2 values of the $SrRuO_3$ cathode on the anode-supported GDC electrolyte at 773 – 973 K decreased with increasing current density. The equivalent circuits for the $SrRuO_3$ cathode on the anode-supported GDC electrolyte at 773 – 973 K did not include [R3C3] parallel circuit. On the other hand, the AC impedance spectra in the low frequency region for the $SrRuO_3$ cathode on the anode-supported GDC electrolyte at 1073 K showed the inductive loop at the low direct current and the capacitive loop ([R3C3]) at the high direct current. The reaction mechanism of O_2 molecules with electrons for the $SrRuO_3$ cathode on the anode-supported GDC electrolyte at 1073 K may change from the reaction mechanism shown in Fig. 5.15 to that shown in Fig. 5.5 (b) as the direct current increases. Both the R2 and R3 values of the $SrRuO_3$ cathode on the anode-supported GDC electrolyte at 1073 K increased with increasing current density. This trend was similar to that of $SrRuO_3$ cathode on the thicker GDC electrolyte at 1073 K. The R2 and R3 values may be affected by the concentration of the oxide ions on the triple phase boundary and the electrolyte surface, respectively, and the concentration of the oxygen vacancy on the electrolyte surface near and far from the triple phase boundary, respectively. The C2 and C3 values showed 10^{-4} – 10^{-3} and 10^{-1} – 10^{2} F, respectively, and were independent of the current density. These values were close to those of the ITO and $SrRuO_3$ cathode on

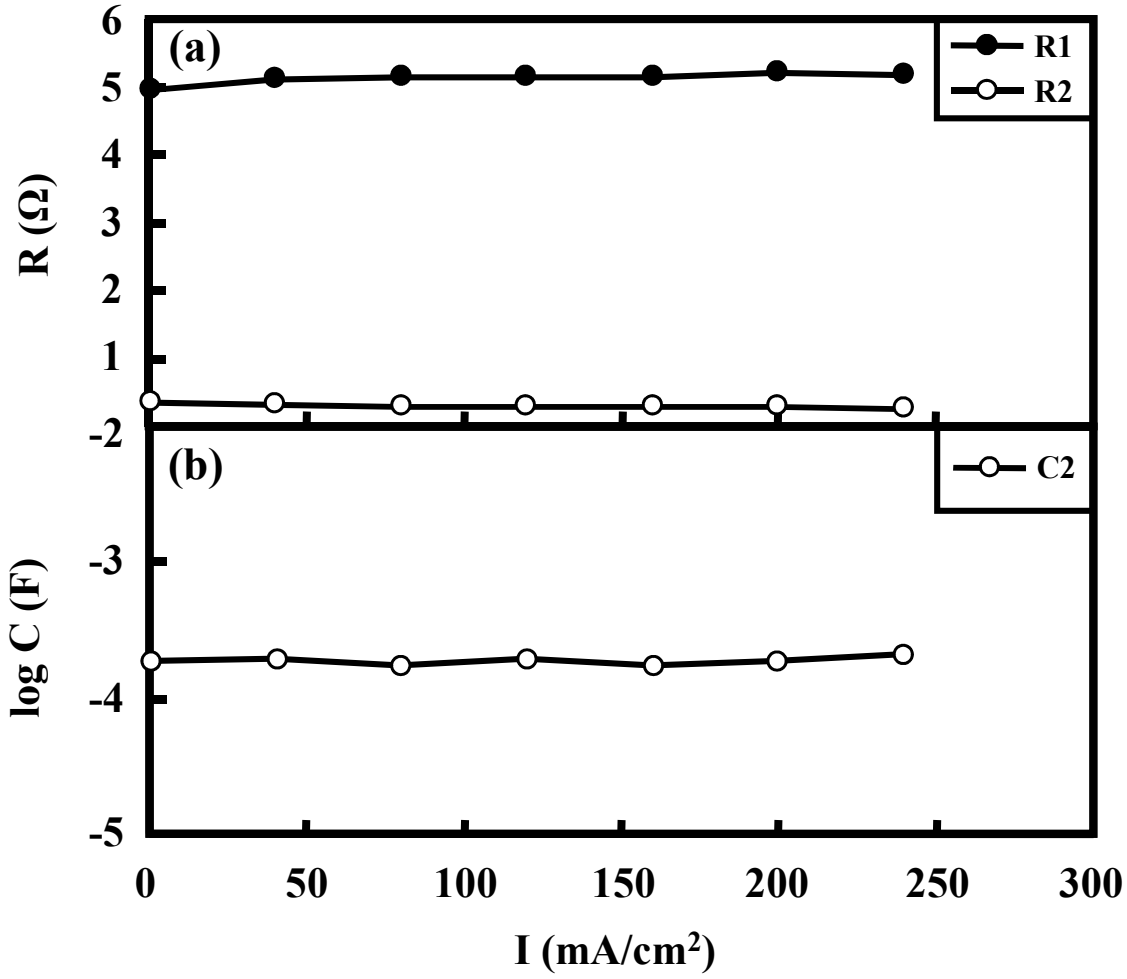

Fig. 5.20 Resistance (a) and capacitance (b) obtained from AC impedance spectra measured for the $SrRuO_3$ cathode on the anode-supported GDC electrolyte at 773 K.

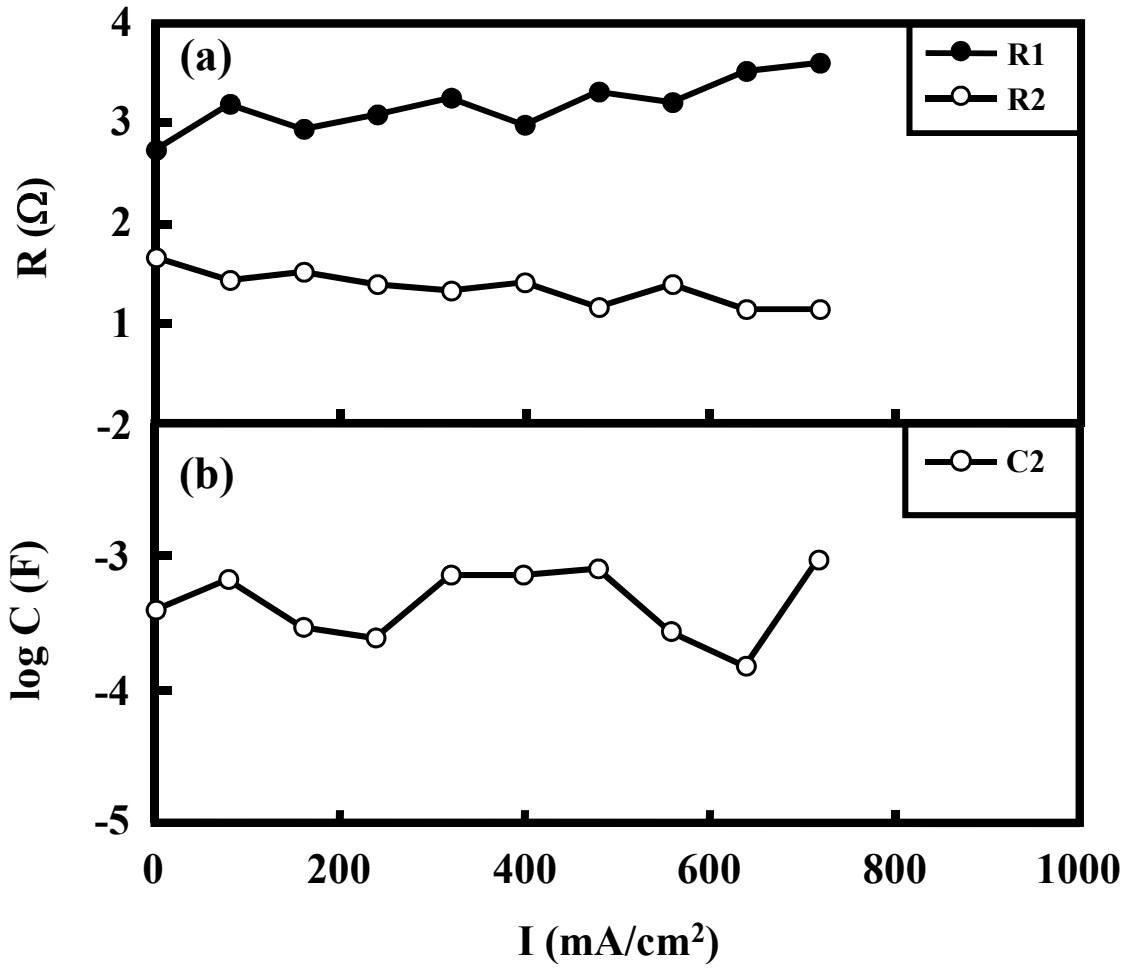

Fig. 5.21 Resistance (a) and capacitance (b) obtained from AC impedance spectra measured for the $SrRuO_3$ cathode on the anode-supported GDC electrolyte at 873 K.

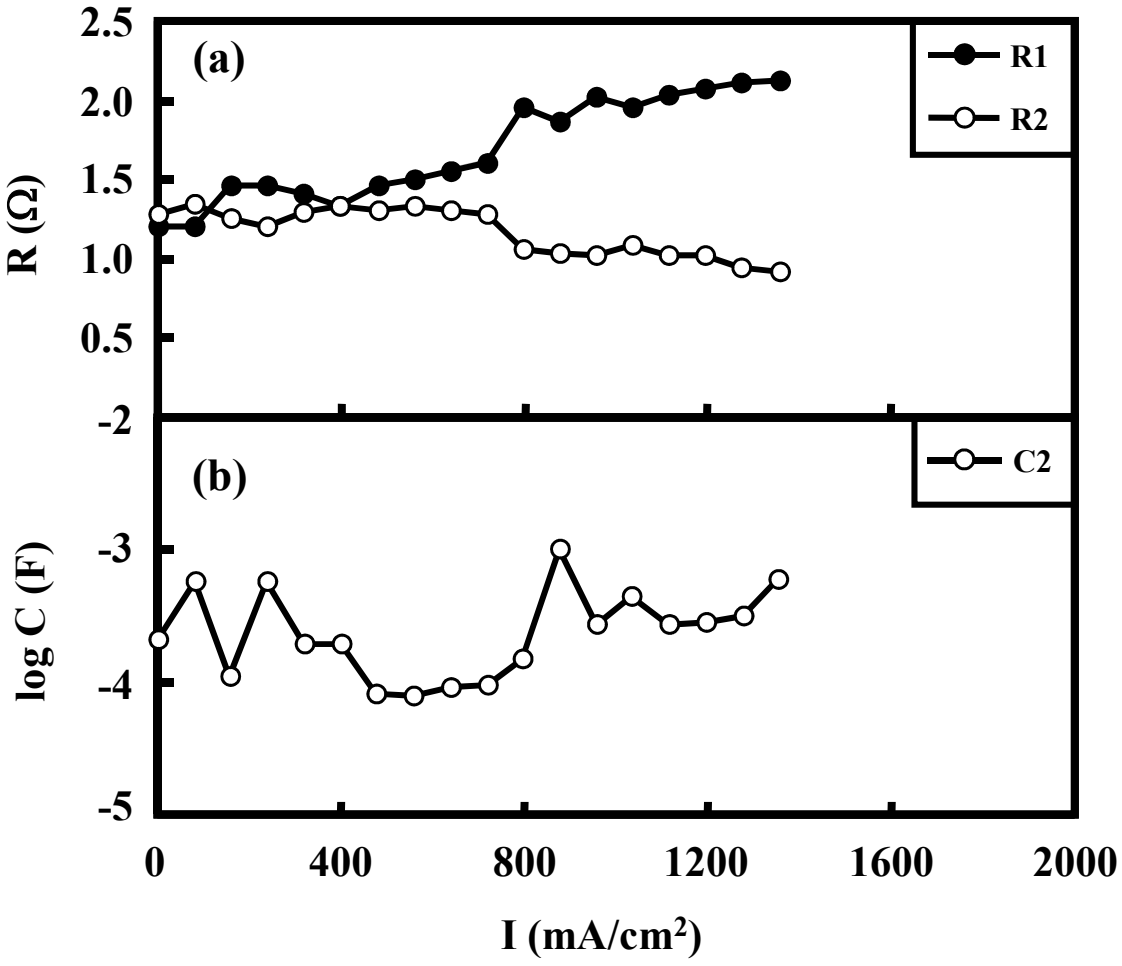

Fig. 5.22 Resistance (a) and capacitance (b) obtained from AC impedance spectra measured for the $SrRuO_3$ cathode on the anode-supported GDC electrolyte at 973 K.

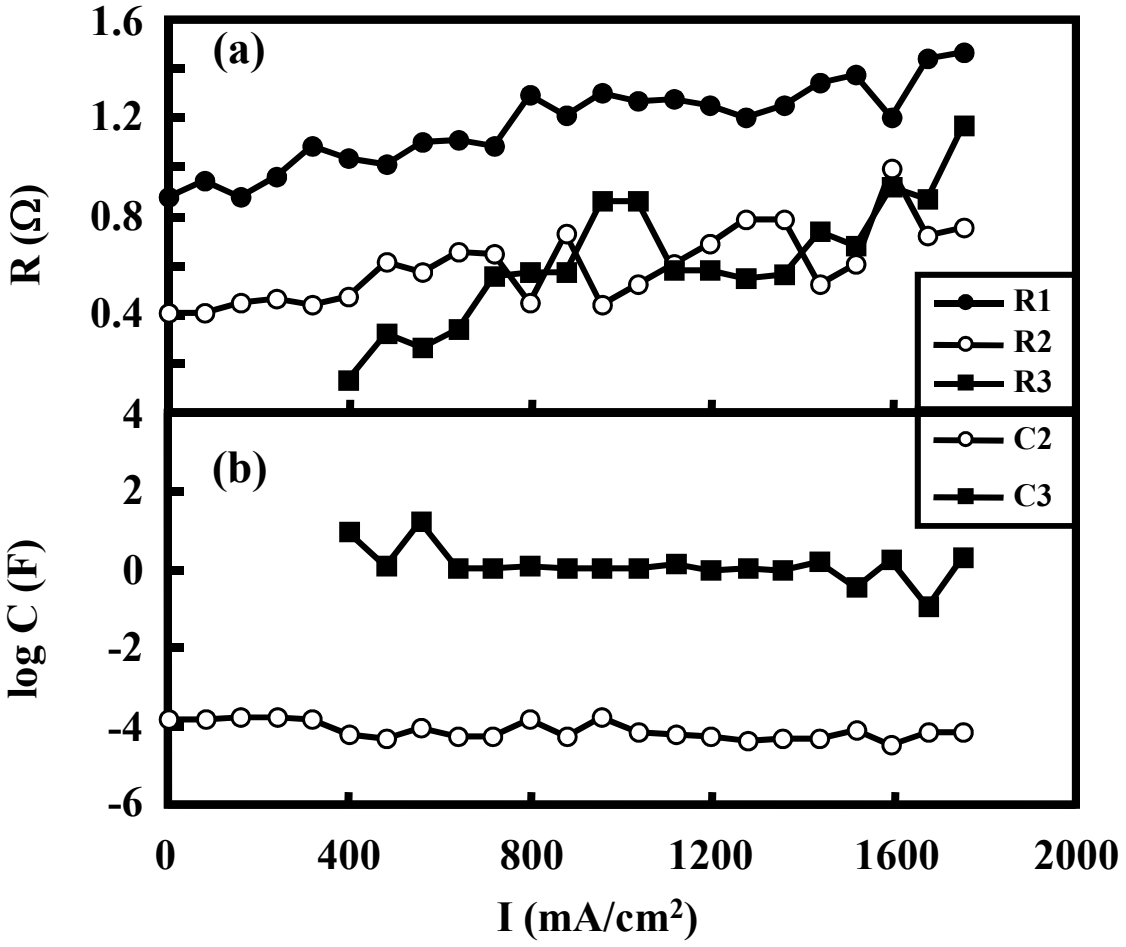

Fig. 5.23 Resistance (a) and capacitance (b) obtained from AC impedance spectra measured for the $SrRuO_3$ cathode on the anode-supported GDC electrolyte at 1073 K.

the thicker electrolyte. The degrees of capacitance of the capacitive loops in the high and low frequency regions may reflect the areas of the triple phase boundary and the electrolyte surface.

5.4 Summary

A direct current-voltage relation and AC impedance were measured for the ITO, $SrRuO_3$ and Co_2RuO_4 cathode using Pt reference electrode on the GDC electrolyte in the temperature range from 773 to 1073 K during the power generation by feeding air as oxidant and 3 vol% H_2O-containing H_2 as fuel. The measured AC impedance spectra were fitted with the equivalent circuit consisting of an ohmic resistance and one or two resistance-capacitance parallel circuits. The insight of the reaction mechanism for the ITO and $SrRuO_3$ cathode was obtained from the AC impedance spectra. In the low direct current, the oxide ions diffuse into the electrolyte near the triple phase boundary. As the direct current increases, the oxide ions spread on the electrolyte surface and diffuse into the electrolyte. The AC impedance spectra for the Co_2RuO_4 cathode on the thicker GDC electrolyte and the $SrRuO_3$ cathode on the anode-supported GDC electrolyte included an inductive loop in the low frequency region. The inductive loop may reflect the reaction of the oxygen adsorbed on the electrolyte surface with the electrons supplied from the anode to the cathode through the electrolyte, and the diffusion of the formed oxide ions into the electrolyte. The resistance obtained from the capacitive loop in the high frequency region decreased with increasing current density, except for the $SrRuO_3$ cathode at 1073 K. The resistance obtained from the capacitive loop in the low frequency region increased with increasing current density. The resistance obtained from the capacitive loops was discussed on the reaction mechanisms proposed in this chapter. The resistance obtained from the capacitive loop in the high frequency region may be affected by the concentration of the oxide ions on the triple phase boundary and the concentration of the oxygen vacancy on the electrolyte surface near the triple phase boundary. The resistance obtained from the capacitive loop in the low frequency region may be affected by the concentration of the oxide ions on the electrolyte surface and the concentration of the oxygen vacancy on the electrolyte

surface far from the triple phase boundary. The capacitance of the capacitive loops in the high and low frequency regions showed 10^{-6} – 10^{-3} and 10^{-1} – 10^{2} F, respectively. The degrees of capacitance of the capacitive loops in the high and low frequency regions may reflect the areas of the triple phase boundary and the electrolyte surface.

References

1) S. B. Adler, Chem. Rev. 104, 4791-4843 (2004).

2) D. Y. Wang and A. S. Nowick, J. Electrochem. Soc., 128, 55-63 (1981).

3) B.A. van Hassel, B.A. Boukamp and A.J. Burggraaf, Solid State Ionics 48, 139-154 (1991).

4) A. Mitterdorfer and L.J. Gauckler, Solid State Ionics 117, 187-202 (1999).

5) A. Hara, Y. Hirata, S. Sameshima, N. Matsunaga and T. Horita, J. Ceram. Soc. Japan, accepted, November 2007.

6) S. Nishiyama, T. Mukozono and T. Hattori, Proceedings of the 11th Fall Meeting of The Ceramic Society of Japan (1998), p. 204.

7) K.W. Kim, J.S. Lee, T.W. Noh, S.R. Lee and K.Char, Phys. Rev. B, 71, 125104 (2005).

8) J. H. Park and R. N. Blumenthal, J. Electrochem. Soc., 136, 2867-2876 (1989).

9) E. J. L. Schouler and M. Kleitz, J. Electrochem. Soc., 134, 1045-1050 (1987).

Chapter 6
Conclusions

Solid oxide fuel cell (SOFC) is a power generation system to convert chemical energy directly into electricity at a high efficiency. This system is operated at about 973 – 1273 K to enhance the diffusion of oxide ions. The increase of oxide ion conductivity and the decrease of the thickness of solid electrolyte, lead to the decrease of operation temperature of SOFC. The decrease of the operation temperature increases the lifetime of SOFC and expands the choice of constituent materials used for the electrodes and interconnector. It is reported that rare earth-doped ceria (RDC) has a higher oxide ion conductivity than the conventional electrolyte of yttria-stabilized zirconia (YSZ). The problem pointed out on RDC is the increased electronic conduction at a low oxygen partial pressure, which is accompanied by the reduction of Ce^{4+} to Ce^{3+}. On the other hand, the ohimc resistance of the electrolyte as well as the overpotentials at the electrodes increases with decreasing operation temperature of SOFC. This thesis mainly comprises the electronic conductivity of La-doped ceria, the electrochemical properties of the cells with the different cathodes, the fabrication of the thin electrolyte film by the doctor-blade method and the cell performance of the anode-supported SOFC. This thesis clarified the ranges of temperature and oxygen partial pressure for RDC as an ionic conductor, and proved that $SrRuO_3$ is a promising cathode material for RDC electrolyte.

In chapter 1, the problems on the practical use and the improvement of the cell performance of SOFC are mentioned, and the purpose of this study is described.

In chapter 2, the electronic conductivity of $Ce_{0.8}La_{0.2}O_{1.9}$ (La-doped ceria, LDC) was studied. The electronic conductivity of LDC was measured in a temperature range from 773 to 1113 K by direct current polarization method using the Hebb-Wagner ion blocking cell. A high linearity between ln σ_e (electronic conductivity)-E (applied voltage), which was theoretically predicted, was measured for LDC in the applied voltage of 0.2-1.0 V. The electronic conduction of LDC was proportional to $Po_2^{-1/4.3}$ ~ $Po_2^{-1/4.6}$ in the higher Po_2 range (10^{-2}-10^{-8} Pa) and $Po_2^{-1/6.7}$ ~ $Po_2^{-1/7.1}$ in the lower Po_2

range ($10^{-7.5}$-10^{-22} Pa). The activation energy for electronic conduction at Po_2 = 10^{-2}-10^{-14} Pa was 1.87-1.94 eV. In the Po_2 range from 10^2 to 10^5 Pa, hole conduction with the slopes of 0.21-0.27 in the log σ_e-log Po_2 plot was measured. The transference number (t_i) of oxide ion for the present LDC was significantly higher than the previously reported values. The t_i value for LDC at 773-1113 K was 0.96-1.00 under an oxygen partial pressure of 10^{-5} Pa. These results were compared with the previously reported data of Sm-doped ceria and Gd-doped ceria. The data measured for SDC at 1073 K have the trend similar to LDC studied in this chapter. The slope of log σ_e–log Po_2 plot for SDC at 1073 K was −1/4.1 in the Po_2 range from 10 to 10^{-7} Pa and decreased to −1/7.1 in the Po_2 range from 10^{-8} to 10^{-16} Pa. The slope of log σ_e–log Po_2 plot was also determined from the linear relationship between ln I (electronic current)–E (applied voltage). The slope for GDC was −1/6 in the temperature range from 873 to 1113 K, while the slope for SDC was in the range from −1/10.1 to −1/6.2 and increased with increasing temperature in the temperature range from 773 to 1073 K. The reported electronic conductivity of GDC was comparable to the conductivity of the present LDC. However, the reported SDC showed a higher electronic conductivity than the present LDC.

In chapter 3, indium tin oxide (ITO, 90 mass% In_2O_3-10 mass% SnO_2), perovskite-type oxide $SrRuO_3$, and Co_2RuO_4 with high electrical conductivity were studied as a cathode of SOFC with Gd-doped ceria ($Ce_{0.8}Gd_{0.2}O_{1.9}$, GDC) electrolyte and Ni-GDC anode. The electrochemical properties were measured for ITO, $SrRuO_3$ or Co_2RuO_4 (cathode) / GDC (electrolyte) / Ni-GDC (anode) cells at 873 and 1073 K using 3 vol% H_2O-containing H_2 fuel and compared with the cell with $La_{0.6}Sr_{0.4}Co_{0.2}Fe_{0.8}O_3$ (LSCF) cathode. The open circuit voltages of the cells with ITO, $SrRuO_3$, Co_2RuO_4 and LSCF cathode was 0.93, 0.85, 0.84 and 0.81 V at 873 K, respectively, and was 0.82, 0.82, 0.57 and 0.79 V at 1073 K, respectively. The maximum power densities of the cells with ITO, $SrRuO_3$, Co_2RuO_4 and LSCF cathode was 21, 36, 38 and 12 mW/cm^2 at 873 K, respectively, and was 71, 328, 183 and 113 mW/cm^2 at 1073 K, respectively. The voltage drop was larger for the cathode than for the anode except for the cell with Co_2RuO_4 cathode. The ohmic resistance and

overpotential was large in the order of Co_2RuO_4 < $SrRuO_3$ < LSCF < ITO and in the order of $SrRuO_3$ < Co_2RuO_4 < LSCF < ITO, respectively. The $SrRuO_3$ powder did not react with the GDC powder at 1073 K. On the other hand, the Co_2RuO_4 powder reacted with the GDC powder at 1073 K to form Co_3O_4 and $Gd_2Ru_2O_7$. The low open circuit voltage and the low voltage drop at the cathode for the cell with Co_2RuO_4 cathode may be due to the formation of Co_3O_4 and $Gd_2Ru_2O_7$ between GDC electrolyte and Co_2RuO_4 cathode. Therefore, the $SrRuO_3$ is the promising candidate of the cathode for the low temperature SOFC in view of the low overpotential and high phase compatibility with GDC electrolyte.

In chapter 4, the GDC electrolyte thin film supported by NiO-GDC anode was fabricated by the doctor blade method. Then, the electrochemical properties of the anode-supported SOFC with the $SrRuO_3$ cathode were measured in the temperature range from 773 to 1073 K using 3 vol% H_2O-containing H_2 fuel. The open circuit voltage was 0.23, 0.46, 0.55 and 0.57 V at 773, 873, 973 and 1073 K, respectively. The maximum power density and the corresponding current density were 15 mW/cm^2 and 121 mA/cm^2 at 773 K, 100 mW/cm^2 and 439 mA/cm^2 at 873 K, 234 mW/cm^2 and 757 mA/cm^2 at 973 K, and 381 mW/cm^2 and 1154 mA/cm^2 at 1073 K. The voltage drop at the cathode was nearly equal to the voltage drop of the whole cell. The voltage drop at the anode was negligible. The fraction of the overpotential to the voltage drop at the cathode increased with increasing temperature.

In chapter 5, the insights of the reaction mechanism of O_2 molecules with electrons at the cathode for the SOFC measured in chapters 3 and 4 were obtained from the AC impedance spectra. A direct current-voltage relation and AC impedance were measured for the ITO, $SrRuO_3$ and Co_2RuO_4 cathode using Pt reference electrode on the GDC electrolyte in the temperature range from 773 to 1073 K during the power generation by feeding air as oxidant and 3 vol% H_2O-containing H_2 as fuel. The measured AC impedance spectra were fitted with the equivalent circuit consisting of an ohmic resistance and one or two resistance-capacitance parallel circuits. The insight of the reaction mechanism for the ITO and $SrRuO_3$ cathode was obtained from the AC impedance spectra. In the low direct current, the oxide ions diffuse into the electrolyte

near the triple phase boundary. As the direct current increases, the oxide ions spread on the electrolyte surface and diffuse into the electrolyte. The AC impedance spectra for the Co_2RuO_4 cathode on the thicker GDC electrolyte and the $SrRuO_3$ cathode on the anode-supported GDC electrolyte included a inductive loop in the low frequency region. The inductive loop may reflect the reaction of the oxygen adsorbed on the electrolyte surface with the electrons supplied from the anode to the cathode through the electrolyte, and the diffusion of the formed oxide ions into the electrolyte. The resistance obtained from the capacitive loop in the high frequency region decreased with increasing current density, except for the $SrRuO_3$ cathode at 1073 K. The resistance obtained from the capacitive loop in the low frequency region increased with increasing current density. The resistance obtained from the capacitive loops was discussed on the reaction mechanisms proposed in this chapter. The resistance obtained from the capacitive loop in the high frequency region may be affected by the concentration of the oxide ions on the triple phase boundary and the concentration of the oxygen vacancy on the electrolyte surface near the triple phase boundary. The resistance obtained from the capacitive loop in the low frequency region may be affected by the concentration of the oxide ions on the electrolyte surface and the concentration of the oxygen vacancy on the electrolyte surface far from the triple phase boundary. The capacitance of the capacitive loops in the high and low frequency regions showed 10^{-6} – 10^{-3} and 10^{-1} – 10^{2} F, respectively. The degrees of capacitance of the capacitive loops in the high and low frequency regions may reflect the areas of the triple phase boundary and the electrolyte surface.

The remaining problems on the practical use and the improvement of the cell performance for SOFC are as follows : (1) open circuit voltage was lower than the theoretical value, (2) reaction mechanism of O_2 molecules with electrons at the cathode and (3) stability of SOFC for the long term operation.

List of Publications

1) **T. Shimonosono**, Y. Hirata, S. Sameshima and T. Horita, “Electronic Conductivity of La-doped Ceria Ceramics”, Journal of the American Ceramic Society, Vol. 88, No. 8, pp. 2114-2120 (2005). (Chapter 2)

2) Y. Hirata, S. Yokomine, S. Sameshima, **T. Shimonosono**, S. Kishi and H. Fukudome, ”Electrochemical Properties of Solid Oxide Fuel Cell with Sm-Doped Ceria Electrolyte and Cermet Electrodes”, Journal of the Ceramic Society of Japan, Vol. 113, No. 9, pp. 597-604 (2005). (Chapter 3)

3) **T. Shimonosono**, X. H. Wang, G. Hiramatsu, Y. Hirata, S. Sameshima, N. Matsunaga, T. Doi and T. Horita, “Oxygen Partial Pressure Dependence of Electrical Conductivity of $La_{0.6}Sr_{0.4}Co_{0.2}Fe_{0.8}O_{3-\delta}$”, Proceedings of the 23rd International Korea-Japan Seminar on Ceramics, pp. 467-470 (2006). (Chapter 3)

4) **T. Shimonosono**, G. Hiramatsu, Y. Hirata, S. Sameshima, N. Matsunaga, T. Doi and T. Horita, “Electrochemical Properties of Cathode for Solid Oxide Fuel Cell”, Key Engineering Materials, Vol. 352, pp. 255-258 (2007). (Chapter 3)

5) **T. Shimonosono**, G. Hiramatsu, Y. Hirata, S. Sameshima, N. Matsunaga, T. Doi and T. Horita, “Electrochemical Properties of Cathode for Solid Oxide Fuel Cell with Gd-Doped Ceria Electrolyte”, Advanced Materials Research, Vol. 26-28, pp. 275-278 (2007). (Chapter 3)

Acknowledgements

The work of this thesis was carried out in Professor Hirata laboratory at Kagoshima University. I would like to express much appreciation and thank to Professor Hirata for his continuous guidance, valuable suggestions and warm-hearted encouragement.

I would like to express my deep gratitude to Professors Toshiya Doi and Teruhisa Horita, for their valuable suggestion and advice for this work.

I also would like to give my acknowledgment to Professor Soichiro Sameshima for his advice. I am grateful to Mr. Masamichi Hoashi for his assistant in EPMA observation, and also to Dr. Naoki Matsunaga and all the members of Hirata laboratory, Kagoshima University for their cooperation and encouragement.

Finally I am grateful to my parents Kyoko and Matsuo Shimonosono for their cooperation and encouragement.

March, 2008
Kagoshima, Japan

Shimonosono Taro